University of Perugia
Department of Civil and Environmental Engineering

unipg
DIPARTIMENTO
DI INGEGNERIA
CIVILE E AMBIENTALE
DIPARTIMENTO DI ECCELLENZA

The
University
Of
Sheffield.

INTERNATIONAL DOCTORAL PROGRAM
IN CIVIL AND ENVIRONMENTAL ENGINEERING

PhD thesis
XXXV cycle

Limit analysis of non-periodic masonry by means of Discontinuity Layout Optimisation

PhD Candidate
Mattia Schiantella

Tutor
Prof. Federico Cluni

International Tutor
Prof. Matthew Gilbert

Abstract

Several historic masonry buildings comprise elements formed using stone masonry units arranged in an irregular bonding pattern called non-periodic texture. While in the case of periodic textures several methods are available to estimate the strength of the masonry, the influence non-periodicity on structural performance is difficult to establish. In this work the discontinuity layout optimization (DLO) numerical limit analysis procedure is used to investigate the influence of non-periodicity on structural performance by means of a parametrical analysis involving several geometrical parameters. Moreover the influence of mechanical parameters is analysed in the case of periodic texture. Both a rigid block discrete analysis and smeared continuum analysis are considered and they are applied to a range of representative example problems. The rigid block method is very useful to compare different textures although it requires to know the whole geometry of the wall, while the continuum representation is suited to modelling large areas of wall without needing the characterization of the whole panel and moreover it provides a conservative solution with respect to the rigid block analysis.

October 2022

International Faculty Board

PhD Coordinator

Prof. Filippo Ubertini

Italian members

Belardi Paolo
Bianconi Fabio
Brunone Brunone
Breccolotti Marco
Cavalagli Nicola
Cerni Gianluca
Cluni Federico
Falcinelli Stefano
Ferrante Marco
Flammini Alessia
Formisano Antonio
Fornaciari Da Passano
Gigliotti Giovanni
Gioffrè Massimiliano
Giorgi Giacomo
Gusella Vittorio
Kenny Jose Maria
Manciola Piergiorgio
Materazzi A. Luigi
Meniconi Silvia
Menchetelli Valeria
Mochi Giovanni
Morbidelli Renato
Orlandi Fabio
Pezzolla Daniela
Puglia Debora
Salciarini Diana
Saltalippi Carla
Terenzi Benedetta
Torre Luigi
Valentini Luca
Venanzi Ilaria
Ventura Flaminia

International members

Arwade Sanjay
Caracoglia Luca
Covas Didia
Denoël Vincent
Glisic Branko
Grigoriu Mircea
Halevi Yoram
Laflamme Simon
Rodríguez-Tembleque Luis
Saez Andres
Sritharan Sri

Data Availability Statement: The script for the analysis of plane plasticity problems with DLO can be found at `https://colab.research.google.com/drive/1qgXhlD2JSC_pKU_PF0p3kECFiM9gXTYd`.

Scientific production:

Peer-reviewed publications – Indexed journals:
• Mattia Schiantella, Federico Cluni and Vittorio Gusella. "Parametric Analysis of Failure Loads of Masonry Textures by Means of Discontinuity Layout Optimization (DLO)", Materials 15.10 (2022)

Peer-reviewed publications:
• Federico Cluni, Vittorio Gusella, and Mattia Schiantella. "Upper Bound Limit Analysis of Quasi-Periodic Masonry by Means of Discontinuity Layout Optimization (DLO)", Proceedings of XXIV AIMETA Conference 2019, Springer International Publishing, 2020, pp. 2124–2133.

• M.Schiantella ,M. Gilbert, C. C. Smith, L.He, F. Cluni, V.Gusella, (2022, November). Limit analysis of non-periodic masonry by means of Discontinuity Layout Optimization. In ECCOMAS Congress 2022-8th European Congress on Computational Methods in Applied Sciences and Engineering.

Expected peer-review publications - Indexed Journals:
• L.He, M.Schiantella, M.Gilbert, C.C. Smith, "A Python script for discontinuity layout optimization", Structural and Multidisciplinary Optimization, (In review)
• M.Schiantella, M.Gilbert, C.C. Smith, L.He, F.Cluni, "Limit analysis of quasi-periodic masonry walls", Heritage (Ready for submission)

Contents

Contents

List of Figures

List of Tables

List of abbreviations

RVE . . . .   Representative Volume Element

DLO . . . .   Discontinuity Layout Optimisation

FE - FEM . . . . . .   Finite Element - Finite Element Method

LP . . . .   Linear Programming

AR . . . .   local Aspect Ratio

SSB . . . .   Similar height Stretcher Bond

DSB . . . .   Different height Stretcher Bond

IB . . . .   Irregular Bond

1. Introduction

1.1.Background

Historical buildings were commonly designed to carry gravity loads, without concern for seismic actions and so generally masonry was adopted since its weaknesses such as low tensile and shear strength, low ductility and an anisotropic behaviour (see Corradi et al. (2008), Angelillo et al. (2014)) were not a problem for vertical loads.

In particular ancient masonry has an even weaker structural behaviour (see Fig. 1.1) due to irregularities in materials and in geometries and to inefficient construction techniques. Moreover, over the centuries historical buildings have often been subject to modifications that may have altered the distribution of loads and, potentially, also the effectiveness of the structure in time. Therefore the analysis models applied to such structures must reflect this aspect. For this reason, an accurate analysis in situ is required to better understand the structural characteristics and the state of conservation of the structure and calibrate the model accurately.

The first thing to consider in the evaluation of the strength of masonry buildings is the quality of masonry, as outlined in Borri et al. (2015). If the quality of masonry is not sufficient the wall does not have a global response but tends to disaggregate under seismic actions. This failure mode is the most dangerous because most of the building collapse immediately and the energy required for the activation is low and it may cause deaths and economical expenses. This usually happens when the walls are structured with more leaves (up to three) and the interior of such walls may comprise rubble or even earth elements that tend to disaggregate when subject to loading. If masonry has a good quality but there are not effective connections between walls and between

(a) **(b)**

Figure 1.1: Failure of ancient masonry structures: (a) Basilica of Saint Francis in Assisi, Italy, 1997 (b) Basilica of Saint Benedict in Norcia, Italy, 2016.

walls and slabs, the building can undergo out-of-plane local mechanisms as in de Felice and Giannini (2001). This kind of failure is still dangerous and requires an intermediate value of activation energy. Finally, if also the connections are adequate, the mechanism will be global and the failure will occur in plane. This is the safest failure mode and the hardest to achieve.

With regards to the quality of the masonry, certainly the resistance of stone or brick elements and the quality of mortar have a great impact on the outcome but there are certain factors that depend solely on the texture; for example the dimension and the shape of elements, the horizontality of mortar joints and the staggering of vertical mortar joints. In our work we are focusing on these geometrical aspects since we assume the failure it's not due to disaggregation or crushing of the masonry blocks. This is because for the historical masonry generally the blocks have a great resistance compared to the mortar and so the failure doesn't occur within the blocks in the case of the seismic action but it's characterized by rocking. So the case of multi-leaf walls with rubble masonry is not considered in this work.

A suitable model for the constituent masonry material must be chosen when analysing a historic masonry construction. This is often not straightforward, especially if the masonry comprises blocks or stones that are not arranged in a periodic pattern. The influence of the texture for different periodic schemes is analysed in Rios et al. (2022) for example. Sometimes the bonding pattern will be quasi-periodic, that is to say, courses of a given height are present, though the units within a course may have different widths, and the heights of different courses may also vary. Alternatively, the bonding pattern may be completely irregular, with no discernible bedding courses evident and this may be called chaotic texture.

Masonry structures are commonly modelled using either discrete or smeared continuum representations. In the first case, masonry units are modelled ex-

plicitly, representing non-periodic bonding patterns directly. In this case mortar joints are modelled explicitly though, for sake of simplicity, may be assumed to have zero thickness (used in conjunction with geometrically expanded units). Examples include the methods proposed by Livesley (1978), Ferris and Tin-Loi (2001) and Gilbert et al. (2006), where in the latter two contributions non-associative friction was considered. However, since a typical masonry structure consists of many thousands of masonry blocks, discrete modelling approaches can be computationally expensive since all units must be modelled individually. Thus, alternative smeared continuum formulations have also been developed. Considering periodic masonry, early contributions include those of Pande et al. (1989) and Anthoine (1995). A key development was to use a unit cell or representative volume element (RVE) to ensure the specific properties of masonry can be properly represented. For non-periodic masonry, Cluni and Gusella (2004) used RVEs in conjunction with 'test-windows' of increasing dimensions to capture the elastic properties of the masonry, then extended to enable the strength of the masonry element to be determined by Cavalagli et al. (2011).

Considering quasi-periodic masonry, the concept of a Statistically Equivalent Periodic Unit Cell (SEPUC) was proposed by Šejnoha et al. (2008), whereas for the analysis of non-periodic masonry walls subjected to in-plane loading, Tiberti and Milani (2019) have proposed a workflow that involves starting with a digital image of a wall and then performing a pixel-based limit analysis procedure employing automatically generated homogenized yield surfaces; this approach has also now been extended to treat out-of-plane loading scenarios (Tiberti and Milani 2020).

1.2.Aims of the research

In this work the Discontinuity Layout Optimization (DLO) numerical limit analysis is employed to carry on a parametric analysis considering several different parameters such as the height of the panel, the texture and other geometrical properties and also to study the influence of mechanical properties. As far as the author knows, currently there is not an accurate classification of the masonry textures and their impact on the structural behaviour has not been studied in detail. So the aim of this work is to provide an enhanced classification and to quantify the effect of such classes in the structural strength. For this reason DLO is used to compare the in-plane load carrying capacities of periodic and non-periodic masonry elements. Unlike finite element limit analysis, with DLO (Smith and Gilbert 2007) singularities in the stress or displacement fields can be handled in a direct and natural manner, obviating the need for the use of tailored meshes or adaptive mesh refinement. With DLO it is also possible to readily compare and contrast the results obtained using discrete and smeared continuum representations of masonry constructions, in the latter case adopting for example the homogenized masonry material model developed by de Buhan and de Felice (1997). Moreover, in this work more complex structural examples

have been tested, such as a whole facade subject to a rigid settlement or a seismic action, to show that DLO can deal with real application and complex geometries and load cases. For a proper validation, comparison with FE analysis have been addressed, showing that for the evaluation of the failure multiplier of the panel under seismic loads DLO is a fast and reliable tool.

1.3.Outline of the thesis

This work is organised as follows. In chapter 2 a literature review is provided, with notions in plasticity, Linear programming and FE and DLO methods, chapter 3 explains how DLO can be applied to masonry structural analysis. In chapter 4 the current classification for non-periodic texture is explained and a new classification for quasi-periodic textures is provided along with the explanation of a script for the generation of quasi-periodic samples. In chapter 5 a parametric analysis involving several geometrical and mechanical is carried on by means of DLO. In chapter 6 a comparison with a finite element (FE) method is established to compare and contrast the two methods pointing out advantages and drawbacks. Finally in chapter 7 conclusions are drawn. Appendix A shows a Python DLO script developed in a recent work that allows to conduct plane strain analysis in a fast and intuitive way.

2. Literature review

2.1. Plasticity

Elastic materials are characterized by the existence of a natural state for which both stress and strains are zero. If these materials are subjected to external actions they are deformed until the actions cease and the go back to the natural state. The strains are then reversible and the body accumulates the work done by the external forces as elastic potential energy that is then released when the actions vanish.

However, this model has several limitations with respect to the experimental analysis, since real transformations are not completely reversible but they are characterized by energy dissipation. It is anyway correct to neglect this component until the body is subjected to loads that are far from the failure load.

The main equations for the elastic problem can be found in Section 2.3.2 where the Finite element procedure for an elastic problem is explained. When the intensity of the actions is significant instead, most of the materials behave as an inelastic material.

To deal with such material the theory of plasticity was developed at the end of the 19$^\text{th}$ century and it it's still in evolution nowadays (see Chaboche (2008) for a review).

The key aspect of plasticity are:

- There is a presence of residual plastic strain deformations when the body is unloaded.

- There is not a biunivocal relation between strain and stress.

- The state of the body depends on the load history and so it is an incremental problem.

Moreover depending on how stress and the strain are related several stress-strain relationship. The more common are the following:

- Elastic-perfectly plastic: the stress-strain relation has two branches, the first one is the linear elastic characterized by the Young module E and the second one is characterized by increasing strain at constant stress namely the yield stress.

- Strain hardening: the stress-strain relation has two branches, the first one is the linear elastic characterized by the young module E and the second one that is rec is still linear but with a different slope K<E. Again the threshold between the two regions is the yield stress.

- Rigid-perfectly plastic: this is similar to the elastic-perfectly plastic but in this case the first branch is neglected since it's assumed that the elastic strain are way lower then the plastic strain.

In the Strain hardening model, at every step of the loading and unloading process the yield stress may variate unlike what happens for the elastic- perfectly plastic model; this phenomena is called Baushinger effect.

2.1.1.Yield surface

The stress strain relations can be determined by means of laboratory tests. To describe the switch between the elastic domain and the plastic domain for a triaxial stress state the concept of yield surface is introduced. The hypothesis is that the transition is dependent only on the stress state and the load history. Under this conditions the yield surface is defined as follows:

$$F(\sigma_{ij}, k_m) = 0 \tag{2.1}$$

where σ_{ij} takes into account the stress state and k_m are parameters related to the load history. The original yield surfaces is defined as follows:

$$F_0(\sigma_{ij}) = 0 \tag{2.2}$$

Under the hypothesis of an isotropic transition, the yield condition can be expressed in terms of the principal stress or the stress invariants.

$$\begin{aligned} F(\sigma_1, \sigma_2, \sigma_3) = 0 \\ F(I_1, I_2, I_3) = 0 \end{aligned} \tag{2.3}$$

where

$$\begin{aligned} I_1 &= \sigma_1 + \sigma_2 + \sigma_3 \\ I_2 &= -(\sigma_1\sigma_2 + \sigma_2\sigma_3 + \sigma_3\sigma_1) \\ I_3 &= \sigma_1\sigma_2\sigma_3 \end{aligned} \tag{2.4}$$

Considering the stress space, the vector **OM** represents the stress state:

$$\mathbf{OM} = (\sigma_1, \sigma_2, \sigma_3) \tag{2.5}$$

The stress state can be expressed as a sum of two vectors: the first is the projection on the line where $\sigma_1 = \sigma_2 = \sigma_3$ which versor is v and it's indicated as **ON** and the other one is the difference vector $\mathbf{NM} = \mathbf{OM} - \mathbf{ON}$ All this vector are shown in Fig. 2.1. It follows:
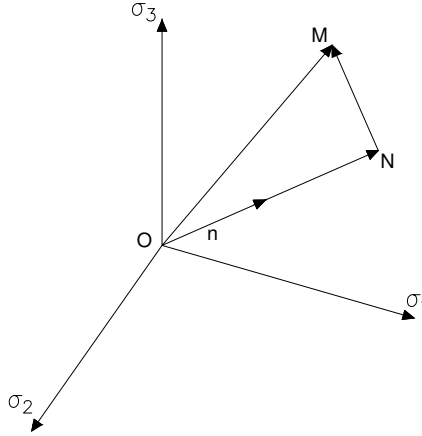
Figure 2.1: Principal stress space representation

$$|\mathbf{ON}| = \mathbf{OM} \times n = \frac{1}{\sqrt{3}}(\sigma_1 + \sigma_2 + \sigma_3) = \sqrt{3}\sigma_m$$

$$\mathbf{ON} = \sqrt{3}\sigma_m n = \sqrt{3}\sigma_m \left(\frac{1}{\sqrt{3}}, \frac{1}{\sqrt{3}}, \frac{1}{\sqrt{3}} \right) = (\sigma_m, \sigma_m, \sigma_m) \tag{2.6}$$

And so:

$$|\mathbf{NM}| = \sqrt{(\sigma_1 - \sigma_m)^2 + (\sigma_2 - \sigma_m)^2 + (\sigma_3 - \sigma_m)^2} \tag{2.7}$$

In the principal frame of reference the stress evaluated in the plane that has n as normal versor is:

$$\sigma(n) = [\sigma] \times n = \frac{1}{\sqrt{3}}(\sigma_1, \sigma_2, \sigma_3) \tag{2.8}$$

The absolute value of the normal component is:

$$|\sigma_n(n)| = \sigma(n) \cdot n = \frac{1}{\sqrt{3}}(\sigma_1, \sigma_2, \sigma_3) \cdot \left(\frac{1}{\sqrt{3}}, \frac{1}{\sqrt{3}}, \frac{1}{\sqrt{3}} \right) = \frac{\sigma_1 + \sigma_2 + \sigma_3}{3} = \sigma_m \tag{2.9}$$

so the normal stress becomes:

$$\sigma_n(n) = |\sigma_n(n)|n = \sigma_m \left(\frac{1}{\sqrt{3}}, \frac{1}{\sqrt{3}}, \frac{1}{\sqrt{3}} \right) \qquad (2.10)$$

and the absolute value of the octahedral tangential stress is:

$$|\tau(n)| = \sqrt{\left(\frac{\sigma_1}{\sqrt{3}} - \frac{\sigma_m}{\sqrt{3}} \right)^2 + \left(\frac{\sigma_2}{\sqrt{3}} - \frac{\sigma_m}{\sqrt{3}} \right)^2 + \left(\frac{\sigma_3}{\sqrt{3}} - \frac{\sigma_m}{\sqrt{3}} \right)^2} = \tau_{oct} \quad (2.11)$$

The term octahedral tangential stress is referred to the fact that this is the absolute value of the tangential stress related to the faces of an regular octahedron which axes are the principal direction of the stress tensor. This frame of reference is useful since points that belong to planes orthogonal to the line of versor $\mathbf{v}$ have the same average stress so the same isotropic part of stress but different deviatoric part of stress. The deviatoric part of stress may be expressed in the following form:

$$s_{ij} = \sigma_{ij} - \delta_{ij}\sigma_m \qquad (2.12)$$

If a material respects the Huber conditions (Huber (1904)) the yield condition is not affected by the isotropic part of the stress. This is the case of Huber-Hencky-Von mises and Tresca criteria commonly used to describe the behaviour of metals or soils such as clays under the hipothesis of undrained conditions.

In this case the failure surface depends just on the deviatoric part of the stress tensor and can be expressed as:

$$F(s_{ij}) = 0 \qquad (2.13)$$

And if the hypothesis of isotropy previously stated it can be expressed also in form of the principal stress or the second and third invariants of the deviatoric part of the stress tensor:

$$F(J_2, J_3) = 0 \qquad (2.14)$$

Since the dependence from the average stress is excluded, the failure surface must be dependent just on two parameters and it can be defined in every plane orthogonal to the line of versor v If the main axis $(\sigma_1, \sigma_2, \sigma_3)$ are projected on this plane the new frame of reference (ξ_1, ξ_2, ξ_3) is defined. The generic state of stress in defined in this new frame of reference by 2 values and considering the orthogonal reference frame (η_3, ξ_3) they are expressed as:

$$\eta_3 = \sqrt{2}\left(\frac{\sigma_2 - \sigma_1}{2} \right)$$

$$\xi_3 = \sqrt{\frac{2}{3}}\left(\sigma_3 - \frac{\sigma_2 - \sigma_1}{2} \right) = \sqrt{\frac{2}{3}}(\sigma_3 - \sigma_m) = \sqrt{\frac{2}{3}}\, s_3 \qquad (2.15)$$

2.1.2.Yield criteria

In this section the most used yield criteria are presented, divided into criteria that depends just on the deviatoric part of the stress tensor and criteria that are dependent from the isotropic component of the stress tensor. For the first kind the Tresca and the Huber-Hencky-Von Mises criteria are shown and for the second kind the Mohr-Coulomb criterion is shown.
Tresca and Mohr Coulomb criteria are used in standard DLO to solve metal plasticity problems and geotechnical problems (see A for some benchmark example).

Tresca criterion

For the Tresca criterion the yielding in a point of the continua occurs when a certain value of the tangential stress is reached:

$$\tau_{max} = k = constant \tag{2.16}$$

From a uniaxial tension stress it follows that:

$$\tau_{max} = \frac{\sigma_s}{2} \tag{2.17}$$

where σ_s is the yield stress. In terms of principal stress:

$$|\sigma_i - \sigma_j| = \sigma_s \tag{2.18}$$

Exchanging indices it is possible to individuate 6 planes parallel to the line of versor v. the yield surface is then a cylinder whose axis is the line of versor v and its expression is:

$$\left((\sigma_1 - \sigma_2)^2 - \sigma_s^2\right)\left((\sigma_2 - \sigma_3)^2 - \sigma_s^2\right)\left((\sigma_3 - \sigma_1)^2 - \sigma_s^2\right) = 0 \tag{2.19}$$

The face of the cylinder is a regular hexagon whose vertices are on the ξ_i axis. the yield curve is described by the relation:

$$\eta_i = \pm\frac{\sqrt{2}}{2}\sigma_s, \ i = 1, 2, 3 \tag{2.20}$$

in the case of plane stress problem ($\sigma_3 = 0$) it follows:

$$\left((\sigma_1 - \sigma_2)^2 - \sigma_s^2\right)\left(\sigma_2^2 - \sigma_s^2\right)\left(\sigma_1^2 - \sigma_s^2\right) \tag{2.21}$$

that is an hexagon in the plane of nonzero stress.

Huber-Hencky-Von Mises criterion

Unlike Tresca's criterion, in this case the yield is reached in a point of the continua when the second invariant of the deviatoric part of the stress tensor reaches a certain value. Recalling that:

$$
\begin{bmatrix} \sigma_1 & 0 & 0 \\ 0 & \sigma_2 & 0 \\ 0 & 0 & \sigma_3 \end{bmatrix} = \begin{bmatrix} \sigma_m & 0 & 0 \\ 0 & \sigma_m & 0 \\ 0 & 0 & \sigma_m \end{bmatrix} + \begin{bmatrix} \sigma_1 - \sigma_m & 0 & 0 \\ 0 & \sigma_2 - \sigma_m & 0 \\ 0 & 0 & \sigma_3 - \sigma_m \end{bmatrix} \tag{2.22}
$$

the second invariant of the deviatoric part is:

$$
\begin{aligned}
J_2 &= -(s_1 s_3 + s_2 s_3 + s_1 s_3) \\
&= -\left((\sigma_1 - \sigma_m)(\sigma_3 - \sigma_m) + (\sigma_2 - \sigma_m)(\sigma_3 - \sigma_m) + (\sigma_2 - \sigma_m)(\sigma_1 - \sigma_m) \right)
\end{aligned} \tag{2.23}
$$

or in an alternative form:

$$
J_2 = \frac{1}{3}\left(\sigma_1^2 + \sigma_2^2 + \sigma_3^2 - \sigma_1 \sigma_2 - \sigma_2 \sigma_3 - \sigma_3 \sigma_1 \right) \tag{2.24}
$$

Recalling that (from Eqn: (2.11))

$$
\begin{aligned}
\tau_{oct} &= \frac{1}{\sqrt{3}} \sqrt{(\sigma_1 - \sigma_m)^2 + (\sigma_1 - \sigma_m)^2 + (\sigma_1 - \sigma_m)^2} \\
&= \frac{\sqrt{2}}{3} \sqrt{(\sigma_1^2 + \sigma_2^2 + \sigma_3^2 - \sigma_1 \sigma_2 - \sigma_2 \sigma_3 - \sigma_3 \sigma_1)}
\end{aligned} \tag{2.25}
$$

Hence:

$$
\tau_{oct}^2 = \frac{2}{3} J_2 \tag{2.26}
$$

And for the criterion the yield condition is reached when:

$$
J_2 = k^2 = constant \tag{2.27}
$$

So, as the Tresca criterion, it depends just on the deviatoric part and so again the yield surface is a cylinder whose axis is the line of versor v.

In case of uniaxial stress the second invariant of the deviatoric part of the stress tensor is:

$$
J_2 = \frac{\sigma_s^2}{3} \tag{2.28}
$$

$$
\Rightarrow k = \frac{\sigma_s}{\sqrt{3}}
$$

and since:

$$
\tau_{oct}^2 = \frac{2}{3} J_2 = \frac{2}{9} \sigma_s^2 \tag{2.29}
$$

$$
\Rightarrow \tau_{oct} = \frac{\sqrt{2}}{3} \sigma_s
$$

then:

$$\mathbf{NM} = \sqrt{3}\tau_{oct} = \sqrt{\frac{2}{3}}\sigma_s \tag{2.30}$$

so the yield curve is a circle whose center belongs to the line of versor v and it lives in the plane orthogonal to it. In Fig. 2.2 the criteria previously described are compared, note that Tresca's hexagon is inscribed into the Von-Mises's circle.

This criterion is related to the distorsion energy concept since the work associated is:

$$L_{dist} = \frac{1}{2G}J_2 \tag{2.31}$$

where G is the shear modulus and so it is clear that it's proportional to the second invariant of the deviatoric part of the stress tensor.
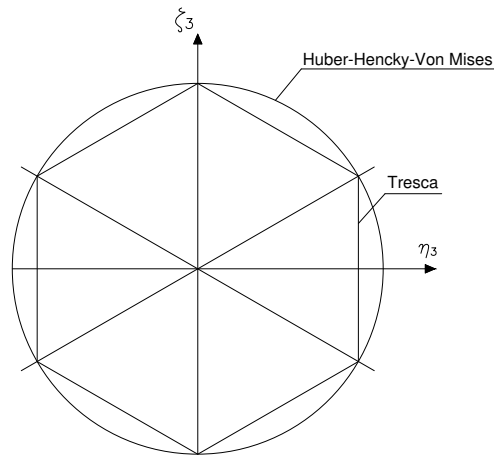
Figure 2.2: Comparison between the Tresca and Huber-Hencky-Von Mises in the $\xi\eta$ plane

Mohr-Coulomb criterion

Mohr-coulomb criterion is used to describe cohesive- frictional materials. Unlike the previous criteria it is dependent on the isotropic part of the stress tensor.

If c is the cohesion and ϕ is the angle of friction, then the shear displacement on a plane is described by the following formula:

$$|\tau| = (c - \sigma)\tan\phi \tag{2.32}$$

In the Mohr plane it is possible to individuate the highest and the lowest normal stress for an uniaxial load that causes failure. In the first case (tension) the

Mohr circle is expressed by:

$$\frac{\sigma'_f}{2} = \left(c - \frac{\sigma'_f}{2}\right)\sin\phi \tag{2.33}$$

thus:

$$\sigma'_f = 2c\,\frac{\sin\phi}{1+\sin\phi} \tag{2.34}$$

In the second case (compression) the Mohr circle is expressed by:

$$\frac{\sigma''_f}{2} = \left(c + \frac{\sigma'_f}{2}\right)\sin\phi \tag{2.35}$$

thus:

$$\sigma''_f = 2c\,\frac{\sin\phi}{1-\sin\phi} \tag{2.36}$$

The previous expression can be deduced by Fig. 2.3. The ratio between the
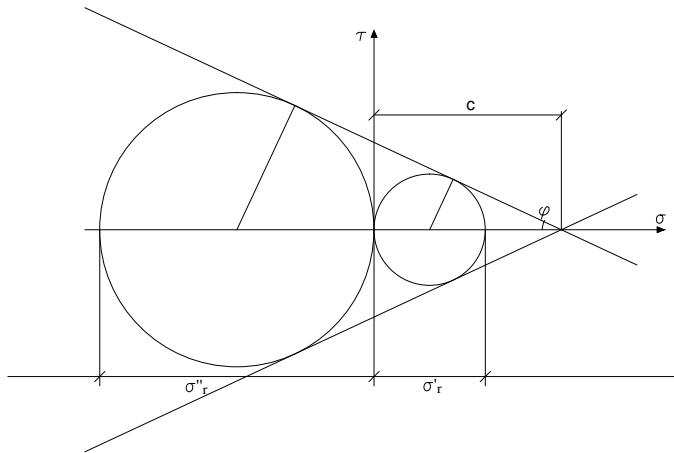
Figure 2.3: Mohr circles at failure for a uniaxial force in tension or compression

maximum stress is only dependent from the angle of friction:

$$\frac{\sigma'_f}{\sigma''_f} = \frac{1-\sin\phi}{1+\sin\phi} \tag{2.37}$$

In the generic stress state the condition that implies the shear displacement at failure is the following:

$$\sigma = \frac{1}{2}(\sigma_1 + \sigma_3) + \frac{1}{2}(\sigma_1 - \sigma_3)\sin\phi \tag{2.38}$$

$$\tau = \frac{1}{2}(\sigma_1 - \sigma_3)\cos\phi$$

if these values of σ and τ are replaced is in Eqn. (2.32) the following is obtained:

$$\sigma_1(1 + \sin\phi) - \sigma_3(1 - \sin\phi) = 2c\sin\phi \tag{2.39}$$

Thus:

$$\sigma_1 - \left(\frac{1 - \sin\phi}{1 + \sin\phi}\sigma_3 = \sigma'_f)\right)$$
$$-\sigma_3 + \left(\frac{1 + \sin\phi}{1 - \sin\phi}\sigma_1 = \sigma''_f)\right) \tag{2.40}$$
$$\Rightarrow \sigma_1\sigma''_f - \sigma_3\sigma'_r = \sigma'_f\sigma''_f$$

The generic form is the following:

$$\sigma_i\sigma''_f - \sigma_j\sigma'_f = \sigma'_f\sigma''_f \qquad i,j = 1,2,3 \tag{2.41}$$

that represent a cone in the principal stress space and an hexagon in the plane orthogonal to the line of versor v (see figure)
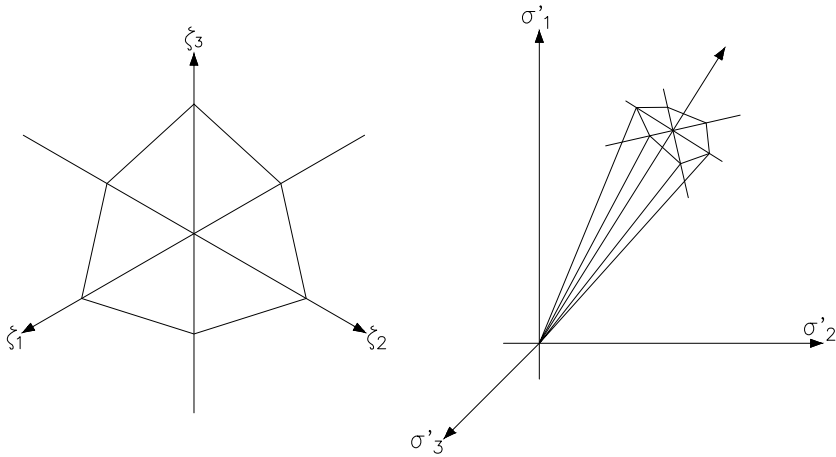
Figure 2.4: Mohr yield curve in the plane $\xi\eta$ and yield surface in the principal stress space for a null cohesion

2.1.3. Associative flow rule
In this work only the hypothesis of associative flow rule is considered.

In this case the yield surface coincides with the original yield surface and it does not vary in the stress space.

Two conditions rule the increment of plastic strain due to an increment of plastic stress: first of all the stress state must satisfy the yield condition and second, the increment of stress must be tangent to the yield surface. So:

$$F(\sigma_{ij}) = 0 \tag{2.42}$$

$$\frac{\partial F}{\partial \sigma_{pq}} d\sigma_{pq} = dF = 0 \tag{2.43}$$

If the bi-symmetric tensor E_{ij} and the infinitesimal parameter $d\lambda$ are introduced, the plastic strain increments may be expressed as:

$$d\epsilon_{ij}^p = d\lambda E_{ij} \tag{2.44}$$

where

$$
\begin{array}{lll}
F = 0 & dF = 0 & \Rightarrow \quad d\lambda \geq 0 \\
F = 0 & dF < 0 & \Rightarrow \quad d\lambda = 0 \\
F < 0 & & \Rightarrow \quad d\lambda = 0
\end{array} \tag{2.45}
$$

It has been shown from experimental tests that E_{ij} is dependent just on the stress state and not from the stress increments and if the plastic potential $P(\sigma ij)$ dependent from the stress state is introduced it follows:

$$E_{ij} = \frac{\partial P}{\partial \sigma_{ij}} \tag{2.46}$$

for ductile materials $P = F$ is assumed so:

$$d\epsilon_{ij}^p = d\lambda \frac{\partial F}{\partial \sigma_{ij}} \tag{2.47}$$

This is what is called associative flow rule. If time is introduced and the plastic strain rate $\dot{\epsilon}_{ij}^p$ is defined then:

$$\dot{\epsilon}_{ij}^p = \dot{\lambda} \frac{\partial F}{\partial \sigma_{ij}} \tag{2.48}$$

so in terms of total strain:

$$\dot{\epsilon}_{ij} = \dot{\epsilon}_{ij}^e + \dot{\epsilon}_{ij}^p \tag{2.49}$$

$$\dot{\epsilon}_{ij} = C_{ijpq} \dot{\sigma}_{pq} + \dot{\lambda} \frac{\partial F}{\partial \sigma_{ij}} \tag{2.50}$$

2.1.4.Limit Analysis

Limit analysis is a structural analysis that allows to directly estimate the collapse load of a structure avoiding iterative or incremental analysis.

A continuum with an elastic-perfectly plastic behaviour is considered and the external actions applied are supposed to increase proportionally.

When these external forces increase, parts of the continuum reach the plastic limit and they develop local plastic strains.

If actions still increase, new parts of the continuum reach the plastic limit until this phenomenon can't be contrasted by the remaining parts anymore and the failure mechanism occurs. The corresponding load is called load factor or failure multiplier.

To obtain this value it is possible to pursue an elasto-plastic analysis that also allows to know the stress-strain relation and the distribution of stresses throughout the continuum but this approach is usually complex and computationally expensive.

If the limit analysis conditions are fulfilled instead, it is possible to avoid to know the evolution of stress and strain. These hypothesis may be expressed as follows:

- Elastic-perfectly plastic material with Drucker stability. The failure surface must be convex and the plastic increments must satisfy the normality condition.

- The displacements and the strain in the elastic regime are small and they don't affect the failure mechanism so that a rigid-perfectly plastic model can be adopted.

- All the actions increase proportionally to a parameter μ called load multiplier.

The following definitions are now introduced:

Statically admissible field: a distribution of stress σ_{ij}^{s} that satisfies the equilibrium conditions (within the body and at the boundary) and does not violate the flow rule condition anywhere so that $F(\sigma_{ij}^{s}) \leq 0$.

A load multiplier that can be associated to a statically admissible field is called statically admissible multiplier (μ_s).

Kinematically admissible field: a distribution of velocities $\dot{u}_k$ and strain velocities $\dot{\epsilon}_{ij}^{k}$ associated to a certain mechanism that satisfies the internal compatibility and the boundary conditions and that provides a positive dissipated power.

A load multiplier that can be associated to a kinematic admissible field is called kinematic admissible multiplier (μ_k).

Since the equivalence between the power dissipated by external and internal forces must hold we have:

$$\int_V \sigma_{ij}^k \epsilon_{ij}^k \, \mathrm{d}v = \int_{S_f} \mu_k f_i \dot{u}_i^k \, \mathrm{d}s = \mu_k \int_{S_f} f_i \dot{u}_i^k \, \mathrm{d}s \qquad (2.51)$$

Thus the kinematic multiplier is obtained as follows:

$$\mu_k = \frac{\int_V \sigma_{ij}^k \epsilon_{ij}^k \, \mathrm{d}v}{\int_{S_f} f_i \dot{u}_i^k \, \mathrm{d}s} \qquad (2.52)$$

Infinitesimal strain theory and proportionally increasing load assumptions are adopted in order to derive this formula.

Collapse condition (failure): the failure mechanism is activated; the yielded part has a relevant dimension and the remaining parts cannot contrast the activation.

Failure multiplier: it's the maximum load multiplier that guarantees the equilibrium between the stress distribution σ_{ij}^f and the external loads $\mu_f f$ and moreover it generates the activation of the failure mechanism with compatible velocities $\dot{u}_f$ and strain velocities $\dot{\epsilon}_{ij}^f$. The first condition is straightforward since load is increased gradually through a series of statically admissible fields.

Since the stress field and actions are in equilibrium and velocities and strain velocities respect compatibility it is possible to state that internal and external dissipated energy is equal as follows:

$$\int_V \sigma_{ij}^f \epsilon_{ij}^f \, \mathrm{d}v = \int_{S_f} \mu_f f_i \dot{u}_i^f \, \mathrm{d}s = \mu_f \int_{S_f} f_i \dot{u}_i^f \, \mathrm{d}s \qquad (2.53)$$

Thus the failure multiplier is:

$$\mu_f = \frac{\sigma_{ij}^f \epsilon_{ij}^f \, \mathrm{d}v}{\int_{S_f} f_i \dot{u}_i^f \, \mathrm{d}s} \qquad (2.54)$$

The failure multiplier is both statically and kinematically admissible and this aspect will be clarified by the Static and the Kinematic Theorems.

Theorem (Static Theorem or Lower Bound Theorem). *The failure multiplier is the maximum of all the statically admissible multipliers.*

$$\mu_s \leq \mu_f \qquad \mu_f = \max \mu_s \qquad (2.55)$$

Proof. Reminding Eqn. (2.53) and considering a statically admissible field (e.g. in equilibrium) and as a kinematic field the collapse field. From the virtual velocity principle:

$$\int_V \sigma_{ij}^s \epsilon_{ij}^f \, \mathrm{d}v = \mu_s \int_{S_f} f_i \dot{u}_i^f \, \mathrm{d}s \qquad (2.56)$$

By subtracting Eqn. (2.53) and Eqn. (2.56) the following equation is obtained:

$$\int_V (\sigma_{ij}^f - \sigma_{ij}^s)\, \epsilon_{ij}^f \, \mathrm{d}v = (\mu_f - \mu_s) \int_{S_f} f_i \dot{u}_i^f \, \mathrm{d}s \qquad (2.57)$$

From the Drucker stability hypothesis:

$$\int_{S_f} f_i \dot{u}_i^f \, \mathrm{d}s > 0; \qquad (2.58)$$

And from the convexity of the failure surface (see Fig. 2.5):
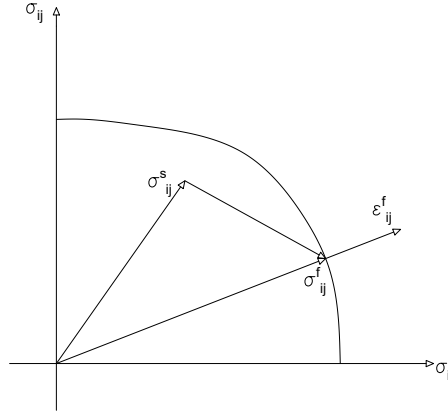
Figure 2.5: Static Theorem: yield surface

$$\int_V (\sigma_{ij}^f - \sigma_{ij}^s)\epsilon_{ij}^f \, \mathrm{d}v > 0; \qquad (2.59)$$

because the angle between the strain velocity vector and the stress difference vector is less than $\pi/2$ and so the dot product is positive.
So in conclusion:

$$\mu_f - \mu_s \geq 0; \qquad (2.60)$$

$\square$

Theorem (Kinematic Theorem or Upper Bound Theorem). *The failure multiplier is the minimum of all the kinematically admissible multipliers.*

$$\mu_f \leq \mu_k \qquad \mu_f = \max \mu_k \qquad (2.61)$$

Proof. Reminding equation Eqn. (2.51) and considering as a static field the collapse field and a kinematic field (e.g.it respect compatibility conditions). From the virtual velocity principle:

$$\int_V \sigma_{ij}^f \epsilon_{ij}^k \, \mathrm{d}v = \mu_f \int_{S_f} f_i \dot{u}_i^k \, \mathrm{d}s \qquad (2.62)$$

By subtracting Eqn. (2.51) and Eqn. (2.62) the following equation is obtained:

$$\int_V (\sigma_{ij}^k - \sigma_{ij}^f)\, \epsilon_{ij}^k \,\mathrm{d}v = (\mu_k - \mu_f) \int_{S_f} f_i \dot{u}_i^f \,\mathrm{d}s \qquad (2.63)$$

From the Drucker stability hypothesis:

$$\int_{S_f} f_i \dot{u}_i^f \,\mathrm{d}s > 0; \qquad (2.64)$$

And from the convexity of the failure surface (see Fig. 2.6):
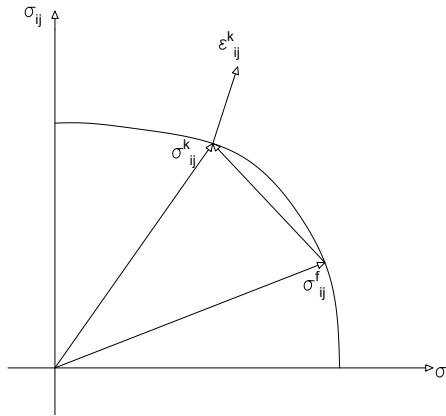
Figure 2.6: Kinematic Theorem: yield surface

$$\int_V (\sigma_{ij}^k - \sigma_{ij}^f)\, \epsilon_{ij}^k \,\mathrm{d}v \geq 0; \qquad (2.65)$$

So in conclusion:

$$\mu_k - \mu_f \geq 0; \qquad (2.66)$$

$\square$

2.2. Linear Programming

Linear programming (LP) is an iterative procedure that allows to minimise or maximise an objective function subject to linear equality and linear inequality constraints.

The core applications of such mathematical feature are related to economics matter since they can account for planning, production, transportation for which minimising cost and maximising profit is essential.

Linear programming basis were built by Fourier in the first half of the 19th but the first applications in structural mechanics were developed over a century later (Maier and Munro (1982)).

The aim of this technique is to solve the following problem that represent the LP problem in its most general and complete form:

$$\max_{\mathbf{x}} \quad \mathbf{c}^{\mathrm{T}}\mathbf{x} \qquad\qquad (2.67a)$$

$$\text{s.t.} \quad \mathbf{A} \cdot \mathbf{x} \leq \mathbf{b} \qquad\qquad (2.67b)$$

$$\mathbf{A_{eq}} \cdot \mathbf{x} = \mathbf{b_{eq}} \qquad\qquad (2.67c)$$

$$\mathbf{l_b} \leq \mathbf{x} \leq \mathbf{u_b}, \qquad\qquad (2.67d)$$

Where $\mathbf{c}$ is a vector defining the orientation of the function to maximize, $\mathbf{x}$ is the vector containing the LP variables, $\mathbf{A}$ and $\mathbf{A_{eq}}$ are the matrices regulating the inequality and equality constraints respectively and $\mathbf{l_b}$ and $\mathbf{u_b}$ are vectors that bound below and above the LP variables. When the problem involves just two variables, it can be easily visualised on a Cartesian plane and a visual solution can be determined. For example the constraint:

$$a_1 x_1 + a_2 x_2 = c \qquad\qquad (2.68)$$

represents a line dividing the plane into two half-planes that satisfy the inequality $a_1 x_1 + a_2 x_2 < c$ or $a_1 x_1 + a_2 x_2 > c$ respectively. Generally speaking, Eqn. (2.68) describes a family of lines $\forall a_1, a_2, c \in \mathbb{R}$ and the vector $\mathbf{a} = (a_1, a_2)$ describes the orthogonal direction with respect to the lines of the family and it is oriented through the ascending values of c.

For two variables, the objective function of a Linear Programming problem is an expression such as $f(x_1, x_2) = c_1 x_1 + c_2 x_2$ that has to be maximised or minimised. To show this function on a Cartesian plane the following family of lines is considered:

$$C = c_1 x_1 + c_2 x_2; \qquad\qquad (2.69)$$

For C that varies in $\mathbb{R}$ this is a set of parallel lines. The highest values of C are obtained moving through the direction indicated by the vector (c_1, c_2) as stated before. So if the problem is a maximisation the latter direction must be considered, and if it's a minimisation instead the opposite direction must be considered instead. The point that solves the problem must fulfill the objective function but also respect the constraints previously defined.

2.2.1. Example of a LP problem for two variables

The following problem is now considered and a visual solution is provided.

$$\max_{\mathbf{x}} \quad 7x_1 + 10x_2 \qquad\qquad (2.70a)$$

$$\text{s.t.} \quad x_1 + x_2 \leq 750 \qquad\qquad (2.70b)$$

$$x_1 + 2x_2 \leq 150 \qquad\qquad (2.70c)$$

$$x_2 < 400 \qquad\qquad (2.70d)$$

$$x_1 \geq 0; x_2 \geq 0 \qquad\qquad (2.70e)$$

In this case, the quantities previously described are: $\mathbf{c}^{\mathrm{T}}=\{7 \quad 10\}$, $\mathbf{x}^{\mathrm{T}}=\{x_1 \ x_2\}$, $\mathbf{b}^{\mathrm{T}}=\{750 \ 150 \ 400\}$, $\mathbf{l_b^{\mathrm{T}}}=\{0 \ 0\}$ and

$$\mathbf{A} = \begin{bmatrix} 1 & 1 \\ 1 & 2 \\ 0 & 1 \end{bmatrix}$$

The first three constraints represents an half-plane as shown in Fig. 2.7. more-

(a) $x_1 + x_2 \leq 750$, Eqn. (2.70b)

(b) $x_1 + 2x_2 \leq 150$, Eqn. (2.70c)

(c) $x_2 < 400$, Eqn. (2.70d)
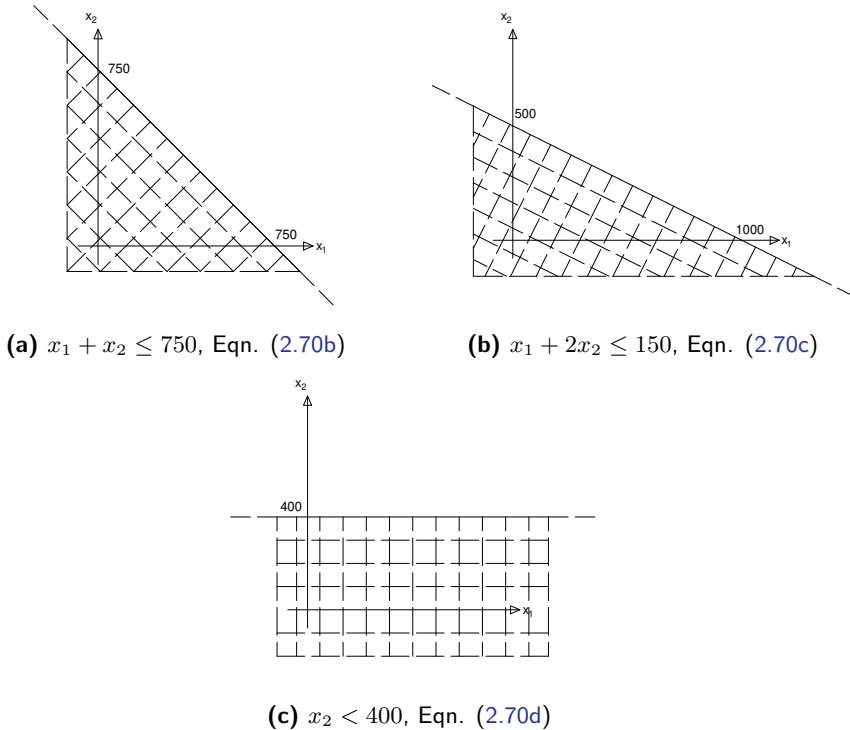
Figure 2.7: Inequality LP constraints

over the last two constraints enforce the solution to the positive x_1, x_2 quarter and so the admissible region is shown in 2.8 And it's defined as:
$S = (x_1, x_2) \in \mathbb{R} \mid x_1 + x_2 \leq 750; x_1 + x_2 \leq 1000; x_2 \leq 400; x_1 \leq 0; x_2 \leq 0$.
Once the domain is determined, parallel lines identified by a certain value of the objective function are drawn until the one corresponding to the maximum value of the objective function is obtained. This line will be tangent to the domain at one of its vertex. That point represents the solution of the optimisation problem. This process is described in Fig. 2.9. It's possible to notice that Linear Programming may lead to a non-unique solution (i.e. the objective function is parallel and not tangent to the domain defined by the constraint for
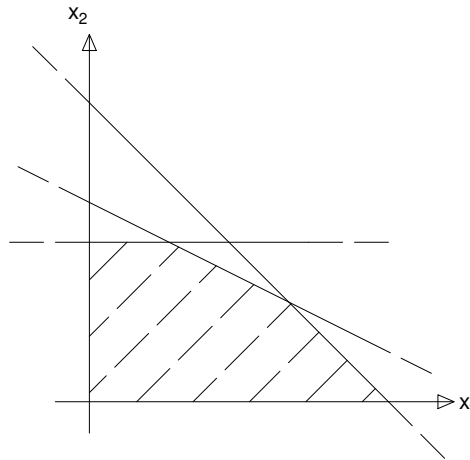
Figure 2.8: Admissible LP region
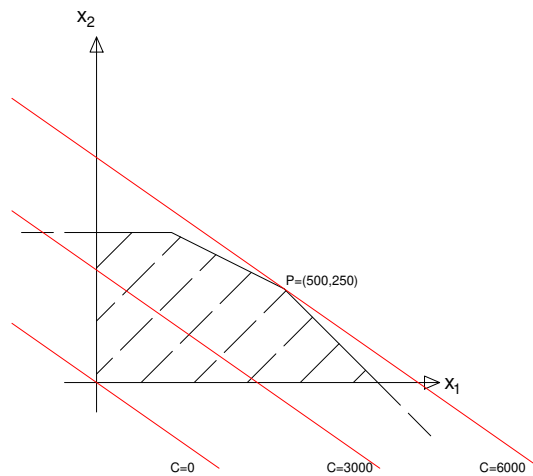
Figure 2.9: LP problem solution

it's target value). Moreover, the solution could not exist if no point satisfies the constraints (i.e. the intersection between the constraints conditions is empty)

If the size of the problem has higher dimensions (over than 3) a graphical method cannot be used to determine the solution, in this case the domain defined by the constraints is defined as a polytope and the solution is still identified by one of the vertices of the domain.

2.2.2.Duality of the LP problem

Each LP problem can also be formulated in its dual version. If we consider the following basic problem:

$$\max_{\mathbf{x}} \quad \mathbf{c}^{\mathrm{T}}\mathbf{x} \tag{2.71a}$$

$$\text{s.t.} \quad \mathbf{A} \cdot \mathbf{x} \leq \mathbf{b} \tag{2.71b}$$

$$\mathbf{x} \geq \mathbf{0} \tag{2.71c}$$

This can also be expressed in the following form that is called symmetric dual problem:

$$\max_{\mathbf{y}} \quad \mathbf{b}^{\mathrm{T}}\mathbf{y} \tag{2.72a}$$

$$\text{s.t.} \quad \mathbf{A}^{\mathrm{T}} \cdot \mathbf{y} \geq \mathbf{c} \tag{2.72b}$$

$$\mathbf{y} \geq \mathbf{0} \tag{2.72c}$$

The two formulations are related by this statements.

- Each variable in the primal LP becomes a constraint in the dual LP problem

- Each constraint in the primal LP problem becomes a variable in the dual LP

- The search of a maximum in the primal problem correspond to the search of a minimum in the dual problem and so the objective function direction is reversed.

Two theorems can be derived (see Matousek and Gärtner (2006) for more details):

Theorem (Weak duality theorem). *For each feasible solution y of the dual linear program (Eqn. (2.72)), the value $\mathbf{b}^{\mathrm{T}}\mathbf{y}$ provides an upper bound on the maximum of the objective function of the linear program (Eqn. (2.71)) i.e. for each feasible solution x of (Eqn. (2.71)) and each feasible solution y of (Eqn. (2.72)) we have:*

$$\mathbf{c}^{\mathrm{T}}\mathbf{x} \leq \mathbf{b}^{\mathrm{T}}\mathbf{y} \tag{2.73}$$

So, if Eqn. (2.71) is unbounded, Eqn. (2.72) has to be infeasible, and if Eqn. (2.72) is unbounded, then Eqn. (2.71) is infeasible.

Theorem (Strong duality theorem). *Consider the primal and the dual Linear Programming problems stated above one of this conditions must occur:*

- *No one of the problems has a feasible solution*

- *The Primal problem is unbounded and the Dual has no feasible solution*

- *The Primal problem has no feasible solution and the Dual is unbounded*

- *Both problems have a feasible solution and if x^* is the optimal solution of the Primal problem and y^* is the optimal solution of the Dual problem then:*

$$\mathbf{c}^\mathrm{T}\mathbf{x} \leq \mathbf{b}^\mathrm{T}\mathbf{y} \tag{2.74}$$

That is the maximum of the Primal Problem and the minimum of the Dual Problem

2.2.3. Linear Programming algorithms
The two most important methods used to solve Linear Programming problems are the Simplex method and the Interior Point method.

Simplex algorithm
It was developed by G.B. Dantzig in 1947 to solve the following canonical problem:

$$\min_{\mathbf{x}} \quad \mathbf{c}^\mathrm{T}\mathbf{x} \tag{2.75a}$$

$$\text{s.t.} \quad \mathbf{A} \cdot \mathbf{x} \leq \mathbf{b} \tag{2.75b}$$

$$x \geq \mathbf{0} \tag{2.75c}$$

Since the solution is known to be at least on one of the vertex of the polytope defined by the constraints Murty (1983) or in one of the extreme points , then the problem reduces to evaluate the value of the function on a finite number of elements. Unfortunately for most of the application this is impossible since the size of the problem is too big and this approach wouldn't be feasible.

So, the idea is to start with the iterative process from one of the vertex and evaluate the value of the objective function. If the point has not the maximum value then it is possible to find an edge where the value of the function increases moving away from the starting point. If this edge is finite then it connects the starting point to another one that has a bigger value of the objective function is unbounded and so the problem has no solution. Once the new vertex is reached the process starts again until the vertex corresponding to the highest value of the objective function is found; if this cannot be reached the the problem has

no solution. Travelling along this edges the number of vertex investigated is way lower than the whole amount. An example of this process for the simple case 2 variables case previously described is shown in Fig. 2.10 The solution of
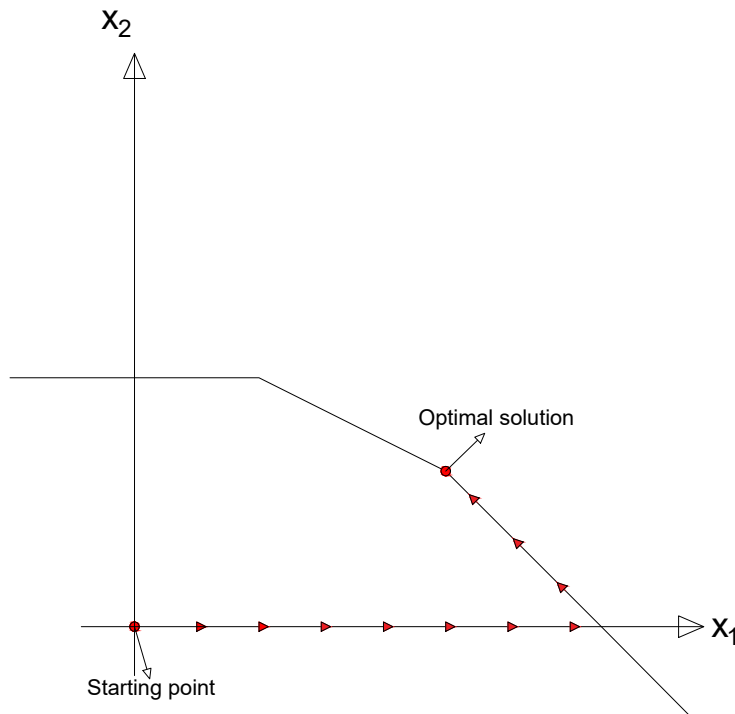
Figure 2.10: Simplex method solution process

the LP problem is achieved in two steps called Phase I and Phase II (Dantzig (2002)). Phase I consists in finding the starting point. This may be trivial in some cases, but generally speaking it may be achieved by applying the simplex algorithm to a modified and simplified version of the original problem.

The possible outcomes for Phase I are either the identification of the starting vertex or the conclusion that the linear problem is infeasible. Phase II consists in applying the simplex algorithm previously described to individuate iteratively which vertex correspond to the highest value of the objective function.

The possible outcomes for Phase II are either an optimal feasible solution or the conclusion that the problem is unbounded and this happens when one of the edges that is travelled is not finite. (Vanderbei (2001))

The simplex algorithm is characterized by a series of pivot operations that allows to move from a feasible basic solution to another one that has an higher value of the objective function. Nering and Tucker (1992)

Interior Point Methods

Interior Point methods have been developed after the simplex method, the are more complex but they allows to find a solution for problems that are out of the capabilities of the simplex method. Moreover Interior Points methods can also solve non-linear programming problems.

The first Interior Point method for Linear Programming was created by Karmarkar (1984). The reason for the name is the fact that the guess for the solution does not follow the boundary of the feasible set as in the simplex method, but it starts from a point within the feasible region ans it moves until it reaches the optimal point at the border of the region. This is also achieved improving the approximation of the optimal solution at each iteration, until it converges to the optimal one (see Strang (1987)). An example of this process for the simple case 2 variables case previously described is shown in Fig. 2.11
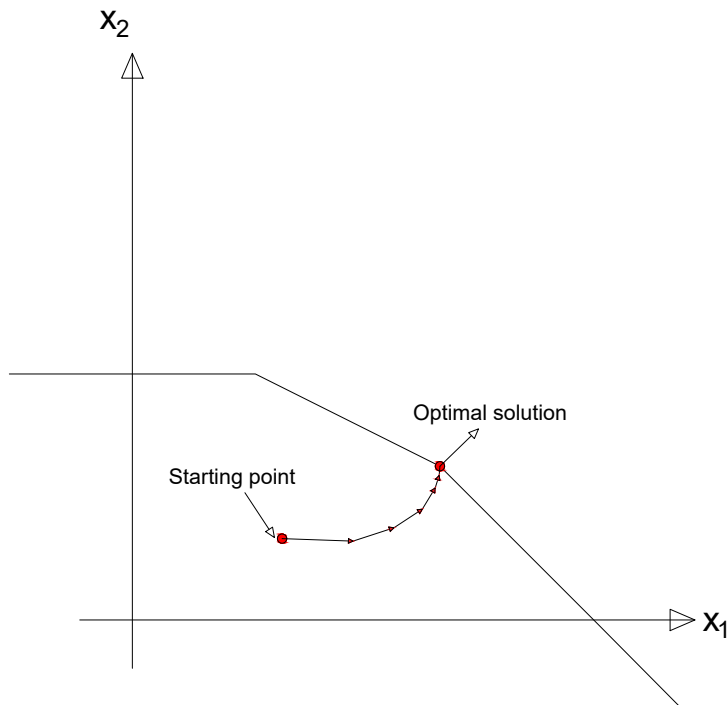
Figure 2.11: Interior Point method solution process

2.3. Finite Element Methods
2.3.1. Introduction

Finite element methods allows to solve complex physical problems by establishing and solving algebraic equations. The development of these methods began with the advent of electronic digital computers. The widely spread of

the method is due to the generality of the problem that can be analysed as well as the ease of establishing the governing equations. Although the method was initially developed to solve structural mechanics problems, it was then recognized that it can be applied for many other class of problems. Bathe (2006) In the beginning it was mainly carried on by mathematicians and physicists (see Courant et al. (1943),Courant and Hilbert (1953),Synge and Rheinboldt (1957),Mikhlin and Chambers (1964)) but important developments also came from engineers (Turner et al. (1956), Argyris and Kelsey (1960)). However the name "finite element" first appeared in Clough (1960), where the technique was used to solve plane stress analysis problems.

The most commonly used method for the structural analysis is the displacement-based FEM. The steps to follow are typically the following:

- idealization of the structure as an assemblage of elements interconnected by joints

- identification of joint displacements

- Resolution of force balance equations to determine the the unknown joints displacements

- Evaluation of the internal stress distribution thanks to the knowledge of elements boundary displacements

- Interpretation the results for both displacements and stresses (they must respect the initial hypothesis)

2.3.2.Formulation

The equations that describe the standard linear elastic problem are the following (see Przemieniecki (1985)):

- Strain-displacement equations $\qquad\qquad\qquad\qquad\qquad\qquad\qquad$ (6)

- Stress-strain equations $\qquad\qquad\qquad\qquad\qquad\qquad\qquad\qquad$ (6)

- Equilibrium equations $\qquad\qquad\qquad\qquad\qquad\qquad\qquad\qquad$ (3)

Strain-displacement equations

The deformed shape of a body can be entirely described by three displacements for each point.

$$u_x = u_x(x, y, z) \qquad\qquad (2.76)$$
$$u_y = u_y(x, y, z) \qquad\qquad (2.77)$$
$$u_y = u_z(x, y, z) \qquad\qquad (2.78)$$

The strains can be expressed as partial derivatives of the displacements. For small deformation the relation between the strain and displacement is linear and they can be expressed like (Timoshenko and Goodier (1934)):

$$\epsilon_{xx} = \frac{\partial u_x}{\partial x} \quad \epsilon_{yy} = \frac{\partial u_y}{\partial y} \quad \epsilon_{zz} = \frac{\partial u_z}{\partial z} \tag{2.79}$$

$$\epsilon_{xy} = \epsilon_{yx} = \frac{\partial u_y}{\partial x} + \frac{\partial u_y}{\partial x} \tag{2.80}$$

$$\epsilon_{yz} = \epsilon_{zy} = \frac{\partial u_z}{\partial y} + \frac{\partial u_y}{\partial z} \tag{2.81}$$

$$\epsilon_{zx} = \epsilon_{xz} = \frac{\partial u_x}{\partial z} + \frac{\partial u_z}{\partial x} \tag{2.82}$$

which can be summarized using index notation as:

$$\epsilon_{ij} = \frac{1}{2}(u_{j,i} + u_{i,j}) \tag{2.83}$$

where the subscript after the comma indicates the partial derivative with respect to that indices.

Stress-strain equations

Elastic strain are related to the stresses by means of the Hooke's law:

$$\epsilon_{xx} = \frac{1}{E}\left(\sigma_{xx} - \nu\left(\sigma_{yy} + \sigma_{zz}\right)\right) \tag{2.84}$$

$$\epsilon_{yy} = \frac{1}{E}\left(\sigma_{yy} - \nu\left(\sigma_{zz} + \sigma_{xx}\right)\right) \tag{2.85}$$

$$\epsilon_{zz} = \frac{1}{E}\left(\sigma_{zz} - \nu\left(\sigma_{xx} + \sigma_{yy}\right)\right) \tag{2.86}$$

$$\epsilon_{xy} = 2\,\frac{1+\nu}{E}\sigma_{xy} \tag{2.87}$$

$$\epsilon_{yz} = 2\,\frac{1+\nu}{E}\sigma_{yz} \tag{2.88}$$

$$\epsilon_{zx} = 2\,\frac{1+\nu}{E}\sigma_{zx} \tag{2.89}$$

$$\tag{2.90}$$

or in a matrix form as:

$$\begin{bmatrix} \epsilon_{xx} \\ \epsilon_{yy} \\ \epsilon_{zz} \\ \epsilon_{xy} \\ \epsilon_{yz} \\ \epsilon_{zx} \end{bmatrix} = \frac{1}{E} \begin{bmatrix} 1 & -\nu & -\nu & 0 & 0 & 0 \\ -\nu & 1 & -\nu & 0 & 0 & 0 \\ -\nu & -\nu & 1 & 0 & 0 & 0 \\ 0 & 0 & 0 & 2(1+\nu) & 0 & 0 \\ 0 & 0 & 0 & 0 & 2(1+\nu) & 0 \\ 0 & 0 & 0 & 0 & 0 & 2(1+\nu) \end{bmatrix} \begin{bmatrix} \sigma_{xx} \\ \sigma_{yy} \\ \sigma_{zz} \\ \sigma_{xy} \\ \sigma_{yz} \\ \sigma_{zx} \end{bmatrix} \tag{2.91}$$

where E is the Young module and ν is the Poisson's ratio.

Equilibrium equations

Equations of equilibrium in three dimensions relating the nine stress components are derived considering equilibrium of moments and stresses acting on a infinitesimal rectangular parallelepiped. It is possible to show that in absence of body moments, the stress tensor is symmetric and then $\sigma_{\mathbf{ij}} = \sigma_{\mathbf{ji}}$ By enforcing equilibrium three partial differential equations can be written:

$$\frac{\partial \sigma_{xx}}{\partial x} + \frac{\partial \sigma_{xy}}{\partial y} + \frac{\partial \sigma_{xz}}{\partial z} + b_x = 0 \qquad (2.92)$$

$$\frac{\partial \sigma_{yx}}{\partial x} + \frac{\partial \sigma_{yy}}{\partial y} + \frac{\partial \sigma_{yz}}{\partial z} + b_y = 0 \qquad (2.93)$$

$$\frac{\partial \sigma_{zx}}{\partial x} + \frac{\partial \sigma_{zy}}{\partial y} + \frac{\partial \sigma_{zz}}{\partial z} + b_z = 0 \qquad (2.94)$$

where (b_x, b_y, b_z) are the body forces in the three directions. The expression can be summarized using index notation as:

$$\sigma_{\mathbf{ij,j}} + bi = 0 \qquad (2.95)$$

or in vector notation form as:

$$\nabla \cdot \sigma = \mathbf{b} \qquad (2.96)$$

2.3.3.Procedure

Now that all the differential equations for the resolution of the problem are set, it is useful to see in detail all the step that lead to the determination of the stresses and strains in the whole body.

- Discretisation

- Evaluation of the stiffness properties of each structural element

- Evaluation of the stiffness properties of the whole structure

- Equilibrium enforcement

- Evaluation of the displacement throughout the continuum through shape functions

Discretisation

In order to solve the continuum problem we need to reduce the degrees of freedom to a finite number. This process is called discretisation and it is realized by dividing the continuum in a set of finite elements. Each element has a certain dimension, its own shape and a number of points that defines its degrees of freedom and the interactions with the adjacent elements. the discretisation of the structure implies that the solution is an approximation and

that the exact solution of the equations is guaranteed only in the nodes of the elements. Anyway, if elements are chosen in a correct way and other rules are followed, it is proved that increasing the number of the elements makes the solution converge to the exact solution.

Evaluation of the stiffness properties of each structural element

Each finite element has its own stiffness properties, this properties depend on the number of degree of freedom, on the elastic properties, on the boundary conditions and on the space in which they are considered (e.g. a beam element in a 2D analysis has less degrees of freedom than a beam in 3D analysis). If the stiffness properties of the element are gathered into a matrix K it is possible to write the following relation between the force applied to the DOFs of the element and the related absolute displacements:

$$\mathbf{F} = \mathbf{Ku} \qquad (2.97)$$

where K is called the local stiffness matrix and it's a square matrix of size $m \times m$ where m is the number of DOFs. The stiffness matrix has only real number entries and it's symmetric due to the Betti's reciprocal work theorem

Evaluation of the stiffness properties of the whole structure

Adjacent finite elements of the structure are connected by nodes. Since the absolute displacement at each node must be equal for all the finite elements which share that node, compatibility conditions must be enforced and it is possible to find a stiffness matrix for the whole structure K_s that relates all the forces applied to the DOFs of the structure with all the displacements. Thus Eqn.(2.97) becomes:

$$\mathbf{F_s} = \mathbf{K_s u_s} \qquad (2.98)$$

Equilibrium enforcement

In this step Eqn. (2.98) is solved and the displacements in all the nodes of the finite elements ($\mathbf{u_s}$) are found.

Evaluation of the displacements throughout the continuum through shape functions

Once the displacements of the degrees of freedom of the structure are found, it is necessary to find the displacements within the continuum to determine the strain and the stress fields. In the finite element method this is achieved through shape functions. Shape functions relate the displacement within a finite element to the known displacement of the nodes of the element itself.

Let's consider for example a triangular element whose node are called l, m and n. A vector $\delta = (\delta_l, \delta_m, \delta_n)$ which contains the displacements in the three directions for each node. Each point within the element has a 3 components displacement, one for each direction and this component are called u, v and w.

We want to define functions that have as input the coordinates of the point and as output the displacements of the point so they can be expressed as:

$$f(x, y, z) = \begin{bmatrix} u(x, y, z) \\ v(x, y, z) \\ w(x, y, z) \end{bmatrix} \quad (2.99)$$

This displacements must be tied to the displacements of the nodes, so it is necessary that if the coordinates of a node are replaced in Eqn. (2.99) then the displacements of the node are obtained. For example for the node l we have:

$$f(x_l, y_l, z_l) = \begin{bmatrix} u(x_l, y_l, z_l) \\ v(x_l, y_l, z_l) \\ w(x_l, y_l, z_l) \end{bmatrix} = \begin{bmatrix} u_l \\ v_l \\ w_l \end{bmatrix} = \delta_{\mathbf{l}} \quad (2.100)$$

The function f can be written as a matrix product between the so called shape functions $(N(x, y, z))$ dependant from the coordinates of the points and the displacements at the nodes.

$$f(x, y, z) = \begin{bmatrix} \mathbf{N}(x, y, z) \end{bmatrix} = \delta \quad (2.101)$$

or in an expanded form;ì:

$$f(x, y, z) = \begin{bmatrix} \mathbf{N_l(x, y, z)} & \mathbf{N_m(x, y, z)} & \mathbf{N_n(x, y, z)} \end{bmatrix} = \begin{bmatrix} \delta_{\mathbf{l}} \\ \delta_{\mathbf{m}} \\ \delta_{\mathbf{n}} \end{bmatrix} \quad (2.102)$$

So a shape function is written for each node and it has two fundamental properties:

- If the coordinates of a node are replaced into a shape function of the same node, the identity matrix is obtained

$$\begin{bmatrix} \mathbf{N_l}(x_l, y_l, z_l) \end{bmatrix} = \begin{bmatrix} 1 & 0 & 0 \\ 0 & 1 & 0 \\ 0 & 0 & 1 \end{bmatrix}$$

- If the coordinates of a node are replaced into a shape function of another node, the null matrix is obtained

$$\begin{bmatrix} \mathbf{N_m}(x_l, y_l, z_l) \end{bmatrix} = \begin{bmatrix} \mathbf{N_n}(x_l, y_l, z_l) \end{bmatrix} = \begin{bmatrix} 0 & 0 & 0 \\ 0 & 0 & 0 \\ 0 & 0 & 0 \end{bmatrix}$$

2.4.Discontinuity Layout Optimisation

Discontinuity Layout Optimisation is a limit analysis approach based on the Upper Bound Theorem of Limit Analysis and Linear Programming developed by Smith and Gilbert (2007). It allows to identify the critical layout of velocity discontinuities and its associated load factor amongst a large set of potential discontinuities in the case of plane strain plasticity. The full set of potential discontinuities is identified by all the lines connecting each pair of nodes of a grid superimposed to the domain. This problem is strongly related to the to the identification of the optimum layout of discrete bars in trusses (e.g. 'Michell' Trusses) and this aspect was formally identified in the past by Hegemier and Prager (1969). The standard DLO formulation is based on a kinematic approach but the dual equilibrium formulation can be derived and it's useful for the application of an adaptive nodal connection procedure.

2.4.1.Analogy with optimal truss layout optimisation
Truss layout optimisation

In order to demonstrate the analogy between the optimal layout of trusses and the basic DLO formulation for a cohesive media the original formulation for truss optimisation is here revisited.

For a planar truss design problem involving n nodes and m potential truss bars connecting those nodes, the equilibrium truss layout optimisation problem formulation that allows to achieve the minimum volume can be written as follows:

$$\min_{\mathbf{q}} \quad V = \mathbf{c}^{\mathrm{T}}\mathbf{q} \tag{2.103a}$$

$$\text{s.t.} \quad \mathbf{Bq} = \mathbf{f} \tag{2.103b}$$

$$\mathbf{q} \geq \mathbf{0}, \tag{2.103c}$$

where V is the volume of the structure, $\mathbf{q}^{T} = \{q_1^+, q_1^-, q_2^+, q_2^- ... q_m^-\}$ is a vector containing tensile and compressive forces, each non-negative: $\mathbf{c}^{T} = \{l_1/\sigma_1, l_1/\sigma_1, l_2/\sigma_2, l_2/\sigma_2 ... l_m/\sigma_m\}$, where l_i and σ_i are respectively the length and yield stress of each bar i. $\mathbf{B}$ is a suitable $(2n \times 2m)$ equilibrium matrix and $\mathbf{f}^{T} = \{f_1^x, f_1^y, f_2^x, f_2^y ... f_n^y\}$, where f_j^x and f_j^y are the x and y components of the external load applied to node j $(j = 1...n)$. The presence of supports at nodes can be accounted for by omitting the relevant terms from $\mathbf{f}$, together with the corresponding rows from $\mathbf{B}$.

Figure 2.12 (a)-(d) presents the steps involved in setting up and solving a simple truss layout optimisation problem.
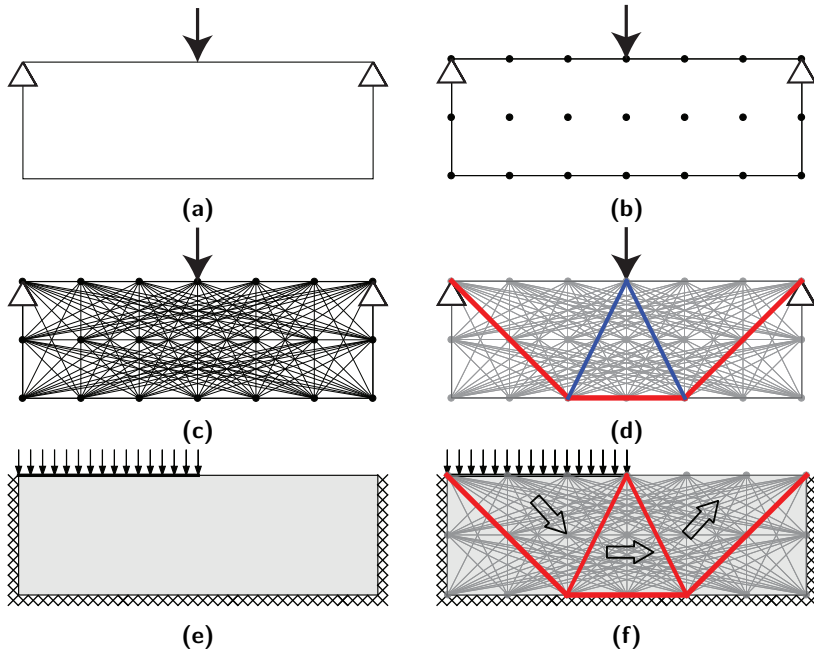
Figure 2.12: Truss and discontinuity layout optimisation problems: (a) truss design domain, loading and support conditions; (b) domain populated with nodes; (c) nodes interconnected with potential truss bars; (d) optimal truss layout (tensile bars shown in red; compressive bars shown in blue); (e) plastic analysis domain and loading conditions; (f) optimal layout of discontinuities at failure, also showing implied movements of the enclosed solid bodies.

Discontinuity Layout Optimisation

The layout of discontinuities that form at failure in the case of a quasi-statically loaded perfectly cohesive body in plane strain has been demonstrated to be analogous to the layout of bars forming an optimal truss (Smith and Gilbert (2007)).

The 'kinematic' slip-line DLO formulation for a body discretized using m nodal connections (slip-line discontinuities), n nodes and a single load case can be written as follows:

$$\min_{\mathbf{d}} \quad E = \mathbf{g}^{\mathrm{T}}\mathbf{d} \tag{2.104a}$$

$$\text{s.t.} \quad \mathbf{Bd} = \mathbf{u} \tag{2.104b}$$

$$\mathbf{d} \geq \mathbf{0}, \tag{2.104c}$$

where E is the total internal energy dissipated due to shearing along the discontinuities, $\mathbf{d}^T = \{s_1^+, s_1^-, s_2^+, s_2^-...s_m^-\}$, where s_i^+, s_i^- are non-negative relative shear displacement jumps between blocks of material along discontinuity i $(i = 1...m)$; $\mathbf{g}^T = \{c_1l_1, c_1l_1, c_2l_2, c_2l_2...c_ml_m\}$, where l_i and c_i are respectively the length and associated cohesive shear strength of discontinuity i. $\mathbf{B}$ is a suitable $(2n \times 2m)$ compatibility matrix and $\mathbf{u}^T = \{u_1^x, u_1^y, u_2^x, u_2^y...u_n^y\}$, where u_j^x and u_j^y are the x and y components of the (virtual) displacement jumps imposed at node j $(j = 1...n)$. Figure 2.12 (e)-(f) presents a coarse nodal discretisation DLO solution to the Prandtl punch problem, which results in the same optimal layout as for the truss problem described in Fig. 2.12(a)-(d); the analogy between truss equilibrium at a node and the compatibility of displacements of bodies sliding relative to each other is illustrated in Fig. 2.13.

2.4.2. Extended Kinematic formulation

The steps for the the DLO procedure are here outlined. First of all the domain is discretized using a grid of nodes and each pair of nodes is connected by potential discontinuities which allows jumps in rate of displacements ($\mathbf{d}$). Then Linear Programming is used to determine the subset of slip lines that are active in the failure mechanism. From now on for the sake of simplicity the terms 'dissipation energy' and 'displacement' may be used as shorthand respectively for 'rate of energy dissipation' and 'rate of displacement'. If a sufficient number of nodes is provided, a wide range of potential mechanisms can be investigated. Given n nodes, the number of connection obtained (m) is $n \times (n-1)/2$ (Dorn (1964)) even if this number includes longer overlapping discontinuities that are discarded. The kinematic formulation, described in Smith and Gilbert (2007) is here shown:
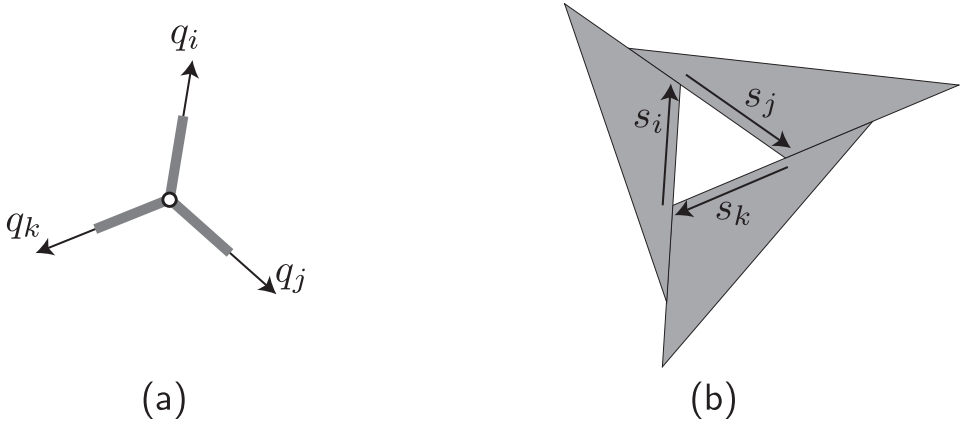
Figure 2.13: Analogy between nodal equilibrium and compatibility conditions: (a) truss equilibrium enforced at a node; (b) discontinuity (slip-line) compatibility condition enforced at a node, shown here with infinitesimal displacements magnified for sake of clarity.

$$\min_{\mathbf{d},\mathbf{p}} \quad \lambda\mathbf{f}_L^T\mathbf{d} = -\mathbf{f}_D^T\mathbf{d} + \mathbf{g}^T\mathbf{p} \tag{2.105a}$$

$$\text{s.t.} \quad \mathbf{Bd} = \mathbf{0} \tag{2.105b}$$

$$\mathbf{Np} - \mathbf{d} = \mathbf{0} \tag{2.105c}$$

$$\mathbf{f}_L^T\mathbf{d} = 1 \tag{2.105d}$$

$$\mathbf{p} \geq \mathbf{0}, \tag{2.105e}$$

where λ is the live load factor, $\mathbf{d}$ is the vector of relative jumps in displacement, $\mathbf{p}$ is the vector containing the plastic multipliers, $\mathbf{g}$ is a vector of dissipating coefficients, $\mathbf{f}_L^T$ and $\mathbf{f}_D^T$ are respectively the vectors of live and dead loads, $\mathbf{B}$ is the global compatibility matrix and $\mathbf{N}$ is the global flow rule matrix.

Compatibility conditions

The failure mechanisms investigated by the kinematic approach are characterized by rigid blocks separated by relative jumps of displacements. For each discontinuity, this displacements have a shear component s_i and a normal component n_i. In Eqn. (2.105b) the compatibility in a global form is enforced. For each discontinuity the compatibility constraint is expressed in the following form:

$$\mathbf{B}_i\mathbf{d}_i = \begin{bmatrix} \alpha_i & -\beta_i \\ \beta_i & \alpha_i \\ -\alpha_i & \beta_i \\ -\beta_i & -\alpha_i \end{bmatrix} \begin{bmatrix} s_i \\ n_i \end{bmatrix} = \begin{bmatrix} u_{A_i^x} \\ u_{A_i^y} \\ u_{B_i^x} \\ u_{B_i^y} \end{bmatrix} = \mathbf{0} \tag{2.106}$$

where α_i and β_i are respectively the x-axis and y-axis direction cosines for the discontinuity i connecting nodes A and B, u_{Ai} and u_{Bi} are the displacement imposed at nodes. A representation of the compatibility condition for a node is shown in Fig. 2.14.
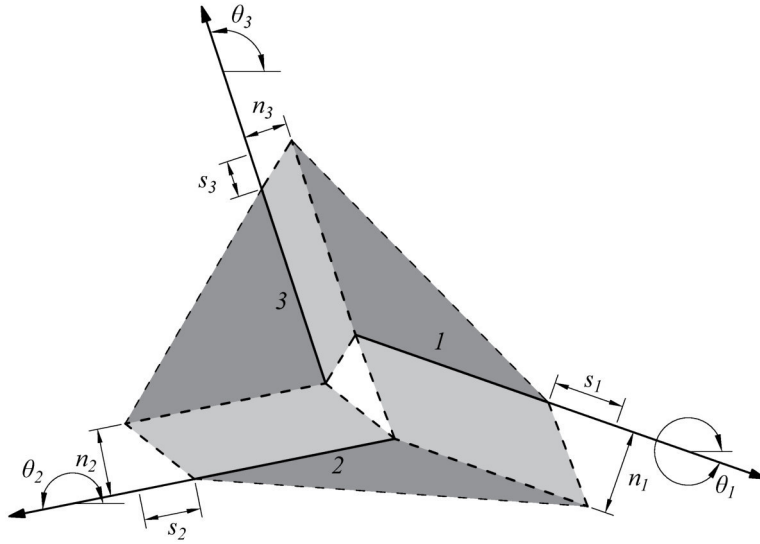
Figure 2.14: Compatibility conditions at nodes.

Thus, the global matrix B has dimensions $2n \times 2m$ where n and m are the number of nodes and discontinuities. It is also important to note that compatibility conditions are also enforced at the crossover between the discontinuities in an implicit way as demonstrated in Hawksbee (2012).

Flow rule conditions
Since the upper bound theorem of plasticity is applied, the flow rule constraints must be imposed (Eqn. (2.105c)), which for a single discontinuity and for the Mohr-Coulomb criterion with associative friction assumes the following form:

$$\mathbf{N}_i \mathbf{p}_i - \mathbf{d}_i = \begin{bmatrix} 1 & -1 \\ \tan \phi_i & \tan \phi_i \end{bmatrix} \begin{bmatrix} p_i^1 \\ p_i^2 \end{bmatrix} - \begin{bmatrix} s_i \\ n_i \end{bmatrix} = 0 \qquad (2.107)$$

where $\tan \phi_i$ is the coefficient of friction and $\mathbf{p_i}$ is a vector containing the plastic multiplier. The global matrix N has dimensions $2m \times 2m$ where m is the number of discontinuities.

Energy dissipation

Energy dissipation is considered in the term $\mathbf{g}^{\mathrm{T}}\mathbf{p}$ where $\mathbf{g} = \{g_1, g_2, \cdots, g_m\}$ has length $2m$ and stores dissipating coefficients. For the Mohr-Coulomb criterion the term $\mathbf{g_i}$ (for the single discontinuity) can be expressed as $\{c_i l_i, c_i l_i\}$.

Boundary conditions

Here a table resuming the principal boundary condition properties are shown. Table 2.1.

Table 2.1: Boundary conditions

Boundary type	Flow rule	Internal energy dissipation	Additional constraint
Free	None	No	No
Rigid/Internal	s and n	Yes	No
Symmetry	n	Yes*	No
Rigid load	s and n	Yes	Eqn. (2.108)

*Energy only dissipated in presence of limiting normal tension or compression at symmetry boundary.

where the equation regulating rigid loads is the following:

$$\left.\begin{array}{l} s_i = s_j \\ n_i = n_j \end{array}\right\} \forall i, j \in \mathbb{F} \tag{2.108}$$

and $\mathbb{F}$ is a set containing the loaded boundary discontinuities.

Load application

Eqn. (2.105a) shows that both live loads and dead loads can be applied. Live loads are collected in the vector $\mathbf{f}_{\mathrm{L}}^{\mathrm{T}} = \{\mathbf{f}_{\mathrm{L1}}^s, \mathbf{f}_{\mathrm{L1}}^n, \mathbf{f}_{\mathrm{L2}}^s, \mathbf{f}_{\mathrm{L2}}^n, \cdots, \mathbf{f}_{\mathrm{Lm}}^n\}$ where $\mathbf{f}_{\mathrm{Li}}^s, \mathbf{f}_{\mathrm{Li}}^n$ are the live and dead loads applied on the i-th discontinuity and similarly dead load are collected in the vector $\mathbf{f}_{\mathrm{D}}^{\mathrm{T}} = \{\mathbf{f}_{\mathrm{D1}}^s, \mathbf{f}_{\mathrm{D1}}^n, \mathbf{f}_{\mathrm{D2}}^s, \mathbf{f}_{\mathrm{D2}}^n, \cdots, \mathbf{f}_{\mathrm{Dm}}^n\}$ where $\mathbf{f}_{\mathrm{Di}}^s, \mathbf{f}_{\mathrm{Di}}^n$ where s and n have the same meaning. Since for the external boundaries displacements jumps must be identical to absolute displacements, loads applied in such discontinuities can be applied directly. For internal discontinuities instead, displacement jumps are not absolute and so loads applied within a body should be evaluated via summation.

In the case of self weight for example, the load applied on an internal discontinuities is the load of the strip of material lying vertically above it, appropriately redistributed in a shear and a normal component depending on the inclination of the discontinuity. However the evaluation of the load in such way it's not efficient and so a new approach that is deepened in the A is presented and it's part of a work currently in review. This new approach is based on the fact that for a non-dilational material, due to conservation of volume, all normal

displacements at boundaries must sum to zero. This is equivalent to say that the amount of material that flows off from a boundary must flow in at another boundary. To compute works done by body forces, it is thus not necessary to track the movement of material throughout the body but evaluate the potential of material that vanishes or appears at boundary and sum these to form the body force work term. Moreover, it is important to note that shear displacements do not affect the volume and so they don't appear in this formulation.

The loss of body force potential P due to a normal body force n acting on a discontinuity is evaluated as follows:

$$\Delta P = nl(k_h \gamma x_m + k_v \gamma y_m) \tag{2.109}$$

where (x_m, y_m) are the coordinates of the mid-point of the discontinuity, γ is the material unit weight, l is the length of the discontinuity, k_h and k_v are respectively the horizontal and vertical accelerations acting on the body (e.g. to model a seismic force acting on a body set $k_h = \pm 1$ for the live loads and $k_v = -1$ for the dead loads).

2.4.3. Equilibrium formulation

Duality principles can be used to derive an equivalent equilibrium formulation that can be expressed as follows:

$$\max_{\mathbf{t},\mathbf{q},\lambda} \quad \lambda \tag{2.110a}$$

$$\text{s.t.} \quad \mathbf{B}^{\mathrm{T}}\mathbf{t} - \mathbf{q} + \lambda\mathbf{f}_{\mathrm{L}} = -\mathbf{f}_{\mathrm{D}} \tag{2.110b}$$

$$\mathbf{N}^{\mathrm{T}}\mathbf{q} \leq \mathbf{g} \tag{2.110c}$$

where $\mathbf{t}$ is a vector containing nodal forces. $\mathbf{q} = [S_1, N_1, S_2, N_2, ..., S_m, N_m]^{\mathrm{T}}$ is a vector of discontinuity forces, where S_i and N_i are shear and normal forces acting on discontinuity i, and m is the number of members. A better understanding of the mathematical meaning of these terms is provided by Smith and Gilbert (2022).

Equation (2.110b) defines the equilibrium condition, e.g. for discontinuity i:

$$\begin{bmatrix} \alpha_i & \beta_i & -\alpha_i & -\beta_i \\ -\beta_i & \alpha_i & \beta_i & -\alpha_i \end{bmatrix} \begin{bmatrix} t_A^x \\ t_A^y \\ t_B^x \\ t_B^y \end{bmatrix} + \lambda \begin{bmatrix} f_{\mathrm{L}i}^{\mathrm{s}} \\ f_{\mathrm{L}i}^{\mathrm{n}} \end{bmatrix} - \begin{bmatrix} S_i \\ N_i \end{bmatrix} = - \begin{bmatrix} f_{\mathrm{D}i}^{\mathrm{s}} \\ f_{\mathrm{D}i}^{\mathrm{n}} \end{bmatrix} \tag{2.111}$$

where α_i and β_i have the same meaning of the kinematic formulation.

Equation (2.110c) defines the Mohr-Coulomb yield-criteria that for discontinuity i has the following form:

$$\begin{bmatrix} 1 & \tan\phi \\ -1 & \tan\phi \end{bmatrix} \begin{bmatrix} S_i \\ N_i \end{bmatrix} \leq \begin{bmatrix} c_i l_i \\ c_i l_i \end{bmatrix}. \tag{2.112}$$

Adaptive nodal connection procedure

Here the adaptive nodal connection procedure is explained; it allows to solve problems involving an high number of discontinuities starting from a core set and then adding only the necessary elements (i.e. the discontinuities that violate the chosen strength criterion).

First the problem is solved for a low number of potential discontinuities (e.g. connecting only adjacent nodes) using the primal formulation (Eqn. (2.105a)) and the nodal forces $\mathbf{t}$ at each node is obtained from the compatibility constraints. Therefore, the discontinuity force vector $\mathbf{q}$ in Eqn. (2.110b) for all potential discontinuities (i.e., discontinuities that are not included in the primal problem) can be obtained. For each of them, the degree of violation in Eqn. (2.110) is evaluated and the most violated are added to the core set and a new iteration begins. The iteration process stops when no more discontinuities are added.

Although the number of discontinuities added at each iteration is chosen via an heuristic procedure, it is shown that the solution obtained with the adaptive connection procedure is the same obtained by the standard DLO (i.e. considering all the potential discontinuities).

More information about the adaptive procedure can be found in A where a script for the analysis of plane strain plasticity problems with Python is provided and explained.

3. Application of DLO to masonry

Contrary to most of the geotechnical problems and metal forming problems that frequently involve only translational failure mechanisms,in the case of interaction between soil and structure or in the case of masonry under a seismic action rotations must be considered.

3.1.Interaction between soil and structure

In the soil structure interaction, the rotations occur mostly at the boundary between the two elements.

A formulations including rotations first presented in Gilbert et al. (2010) is here presented. That formulation has been extended afterwards to consider rotations within the soil with curved sliplines to analyze eccentricity in punch problems in Smith and Gilbert (2013) but the latter formulation is not considered in this work.

If a rotation between a structural element and the soil is considered and a Mohr-Coulomb criterion is adopted, then log-spiral yield lines are observed as shown in Fig. 3.1 Considering Fig. 3.1, the distance r_0 between the center of rotation and the extremal point b is:

$$r_0 = \frac{l}{1 + e^{\pi \tan(\phi)}};$$ (3.1)

where l is the length of the segment AB and where ϕ is the angle of friction of soil. If the boundary rotates by an amount ω then the effect is the same as
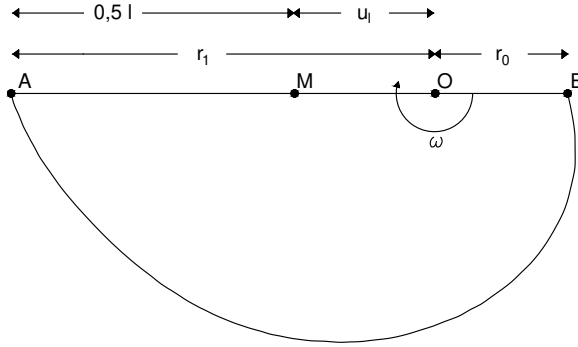
Figure 3.1: Log-spiral geometry for a rotation on a discontinuity AB

a rotation ω in the midpoint M plus an additional dilation $ul\omega$ where:

$$u = 0.5 - \frac{1}{(1 + e^{\pi \tan \phi})} \tag{3.2}$$

Elsewhere, movement can be assumed as purely translational, taken to be equal to the translation of the segment midpoint (including the dilational component). If the material also has cohesion c then the work done for a relative body rotation of ω is:

$$W_\omega = \frac{cl^2 u\omega}{\tan \phi} \tag{3.3}$$

The key formulation is the same as Eqn. (2.105) but vectors and matrices are properly modified as follows. The vector of relative displacements becomes $\mathbf{d}^T = \{s_1, n_1, \omega_1, s_2, n_2, \omega_2, ..., \omega_m\}$ where ω terms are for the rotations, the vector of plastic multipliers is supplemented with two other terms (p_i^3 and p_i^4) and the vector of dissipating coefficients becomes $\mathbf{g}^T = \{c_1 l_1, c_1 l_1, c_i l_i^2 u_i / \tan \phi_i, c_2 l_2, ..., c_m l_m^2 u_m / \tan \phi_m\}$. The compatibility condition for the single discontinuity becomes:

$$\mathbf{B}_i \mathbf{d}_i = \begin{bmatrix} \alpha_i & -\beta_i & \dfrac{l_i \beta_i}{2} \\[2mm] \beta_i & \alpha_i & -\dfrac{l_i \alpha_i}{2} \\[2mm] 0 & 0 & 1 \\[2mm] -\alpha_i & \beta_i & \dfrac{l_i \beta_i}{2} \\[2mm] -\beta_i & -\alpha_i & -\dfrac{l_i \alpha_i}{2} \\[2mm] 0 & 0 & -1 \end{bmatrix} \begin{bmatrix} s_i \\[2mm] n_i \\[2mm] \omega_i \end{bmatrix} \tag{3.4}$$

And the flow rule constraints may be written in this form:

$$\mathbf{N}_i\mathbf{p}_i - \mathbf{d}_i = \begin{bmatrix} 1 & -1 & 0 & 0 \\ \tan\phi_i & \tan\phi_i & u_il_i & u_il_i \\ 0 & 0 & 1 & -1 \end{bmatrix} \begin{bmatrix} p_i^1 \\ p_i^2 \\ p_i^3 \\ p_i^4 \end{bmatrix} - \begin{bmatrix} s_i \\ n_i \\ \omega_i \end{bmatrix} = 0 \quad (3.5)$$

3.2.Rigid block formulation

A natural application is modelling the masonry directly by modelling the joints even if the possibility to consider the failure of masonry blocks themselves can be considered is required. In the case of rigid blocks the rotation occurs at and endpoint with no associated log-spiral slip-line and so the u_i term is 0.5 and no cohesive work within the rigid bodies is done. So the flow rule constraints becomes:

$$\mathbf{N}_i\mathbf{p}_i - \mathbf{d}_i = \begin{bmatrix} 1 & -1 & 0 & 0 \\ \tan\varphi_i & \tan\varphi_i & \frac{1}{2}l_i & \frac{1}{2}l_i \\ 0 & 0 & 1 & -1 \end{bmatrix} \begin{bmatrix} p_i^1 \\ p_i^2 \\ p_i^3 \\ p_i^4 \end{bmatrix} - \begin{bmatrix} s_i \\ n_i \\ \omega_i \end{bmatrix} = 0 \quad (3.6)$$

The stages in the DLO analysis for the rigid block approach are illustrated in Fig. 3.2.
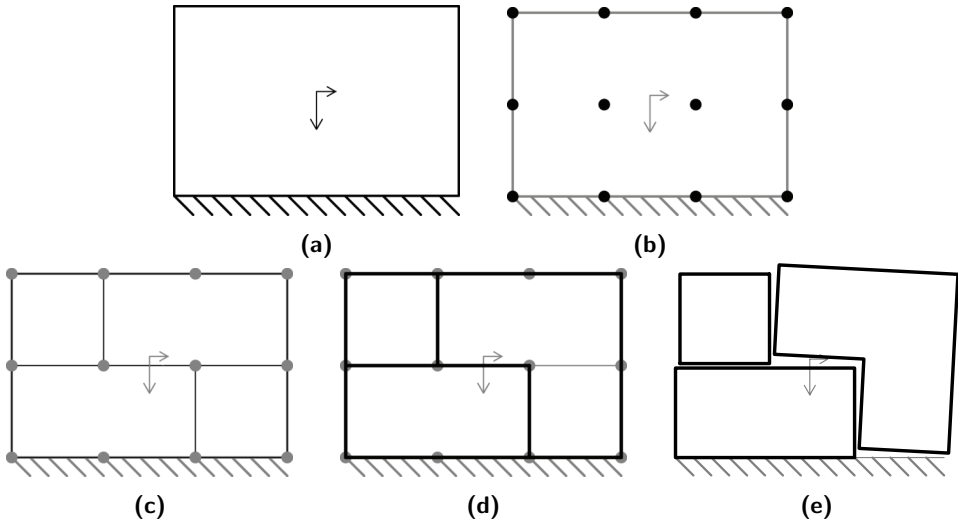
Figure 3.2: Stages in rigid block DLO procedure (a) starting problem (seismic and gravitational body forces applied to block of masonry); (b) discretisation of masonry body using nodes; (c) interconnection of nodes with actual masonry joints only; (d) identification of critical subset of potential discontinuities using optimisation (discrete block solution); (e) corresponding collapse kinematics.

3.3.Homogenized representation (periodic)

The homogenized approach allows failure on any plane and thus follows the conventional DLO approach outlined in Fig. 3.3 c, d and e. For the homogenized
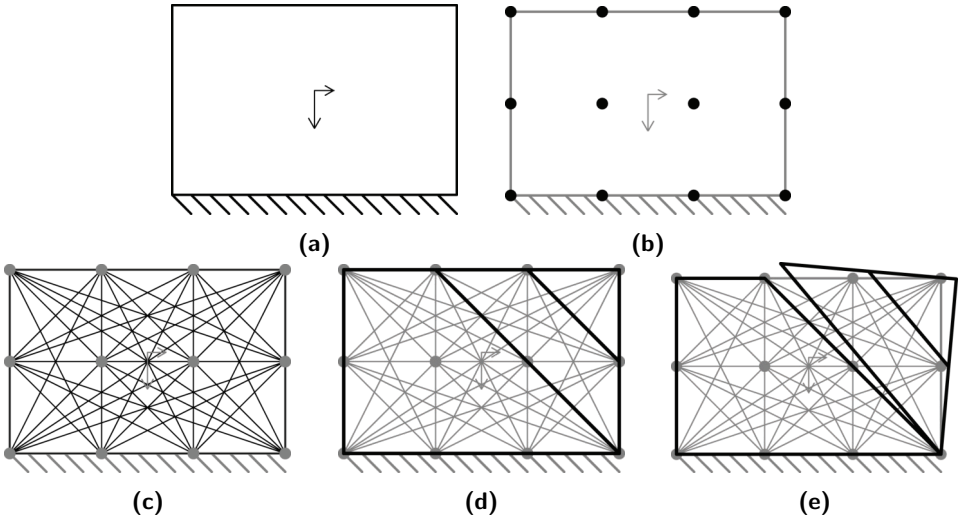
Figure 3.3: Stages in homogenized DLO procedure (a) starting problem (seismic and gravitational body forces applied to block of masonry); (b) discretisation of masonry body using nodes; (c) interconnection of nodes with all potential discontinuities; (d) identification of critical subset of potential discontinuities using optimisation (homogenized solution); (e) corresponding collapse kinematics;

approach, the formulation seen in (2.105) must be extended as follows:

$$\min \lambda \mathbf{f}_{\mathrm{L}}^{T}\mathbf{d} = -\mathbf{f}_{\mathrm{D}}^{T}\mathbf{d} + \mathbf{g}^{T}\mathbf{p}$$

subject to:

$$\mathbf{Bd} = \mathbf{0}$$

$$\mathbf{Np} - \mathbf{d} = \mathbf{0} \qquad (3.7)$$

$$\mathbf{f}_{\mathrm{L}}^{T}\mathbf{d} = 1$$

$$\mathbf{Qp} = \mathbf{0}$$

$$\mathbf{p} \geq \mathbf{0}$$

The formulation has been developed starting from the homogenized approach of (de Buhan and de Felice 1997,Tiberti and Milani 2019). However the formulation involves a more extensive set of plastic multipliers and correspondingly more complex matrices $\mathbf{N}$ and $\mathbf{Q}$ as described by Valentino et al. (2023).

Figure 3.4(a) illustrates the principle of the homogenization approach; instead of modelling individual masonry units, it selects a representative volume element (R.V.E.) to create a compound material that is applied everywhere in the domain, so a continuum problem can be created. The kinematic properties of the R.V.E. is defined by its rigid rotation Q and strain rate tensor $\mathbf{D}$:

$$\mathbf{D} = \begin{bmatrix} D_{11} & D_{12} \\ D_{12} & D_{22} \end{bmatrix}, \tag{3.8}$$

where $\mathbf{D}$ is a symmetrical matrix of the strain rate tensor at any point of the domain; D_{11}, D_{22} and D_{12} are its independent components relating to, respectively, horizontal, vertical and shear strains, see Fig. 3.4(b). The strain

(a)

(b)
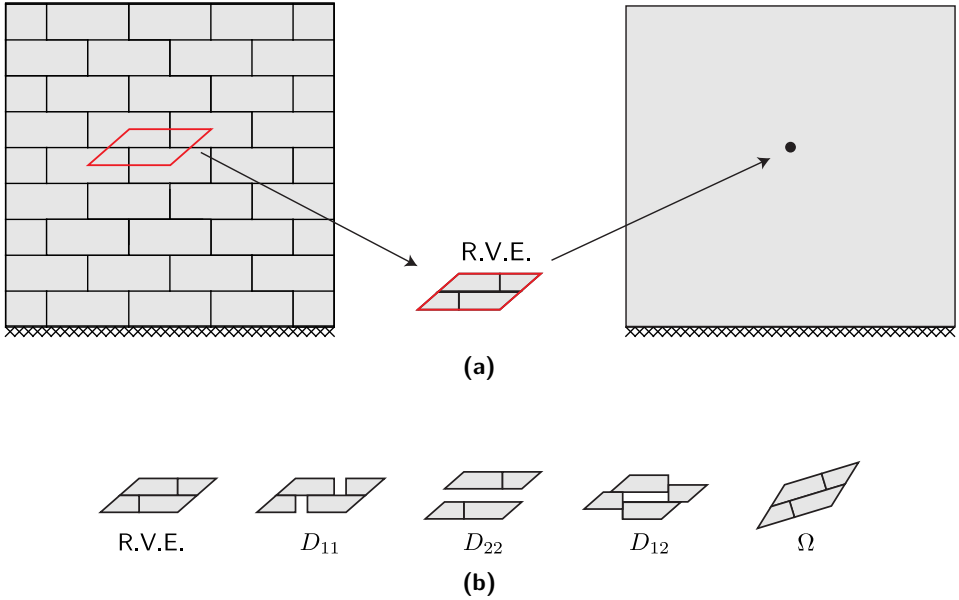
Figure 3.4: Homogenization approach: (a) representative volume element (R.V.E.); (b) Macroscopic strain rate variables $\{D_{11}, D_{22}, D_{12}\}$ and rigid rotation variable Ω

rate variables D_{11}, D_{22} and D_{12} are linked to DLO displacement variables s, n, ω using:

$$\begin{bmatrix} D_{11,\kappa} \\ D_{22,\kappa} \\ D_{12,\kappa} \end{bmatrix} = \begin{bmatrix} -\alpha_i \beta_i & \beta_i^2 & -\dfrac{\kappa \beta_i^2 l_i}{2} \\ \alpha_i \beta_i & \alpha_i^2 & -\dfrac{\kappa \alpha_i^2 l_i}{2} \\ \dfrac{\alpha_i^2}{2} - \dfrac{\beta_i^2}{2} & -\alpha_i \beta_i & \dfrac{\kappa \alpha_i \beta_i l_i}{2} \end{bmatrix} \begin{bmatrix} s_i \\ n_i \\ \omega_i \end{bmatrix} \tag{3.9}$$

where $\kappa = \pm 1$ is a coefficient introduced to distinguish the two end nodes of discontinuity i; and $D_{11,\kappa}$, $D_{22,\kappa}$, $D_{12,\kappa}$ are their strain rate variables.

Instead of directly imposing flow rules on DLO variables, now the strain rate variables D_{11}, D_{22}, D_{12} of the R.V.E. are constrained by examining flow rules for all potential discontinuities within the R.V.E. (see Fig. 3.4):

$$D_{12}r\rho + D_{22} + \Omega r\rho \geq \mu \left| D_{11}r\rho + D_{12} - \Omega \right| \tag{3.10a}$$

$$D_{12}r(\rho - 1) + D_{22} + \Omega r(\rho - 1) \geq \mu \left| D_{11}r(\rho - 1) + D_{12} - \Omega \right| \tag{3.10b}$$

$$D_{11} \geq \mu |D_{12} + \Omega|, \tag{3.10c}$$

where $\mu = \tan \phi$ is the coefficient of friction, r is the aspect ratio of masonry blocks (referred as AR in this work), and ρ is the interlocking ratio. And the associated energy dissipation within the R.V.E. is written as:

$$\Pi = \frac{c\,(D_{11} + D_{22})}{\mu}, \tag{3.11}$$

where Π is the internal energy dissipation associated with the strain rate variables shown in Fig. 3.4(b).

By introducing plastic multipliers $p_1, p_2, ... p_{12}$ that transform (3.10) into equality constraints, expressions (3.9), (3.10) and (3.11) can be rewritten to take the standard DLO form in (3.7). Interested readers can refer to Valentino et al. (2023) for details.

The stages in the DLO analysis for the rigid block approach are illustrated in Fig. 3.2.

4. Non-periodic masonry

Most of historical heritage buildings are made of masonry. While for some prestigious buildings the texture of the masonry is regular, this is not true for most of the cases. Moreover, in the actual realizations, things can be even more complex, since in several cases the building has a multi-leaf masonry, with the exterior curtain characterized by a regular texture, the inner leaf characterized by irregular textures instead, and the two leaf connected by means of a filling of (generally) poor quality Anzani et al. (2008); Llorens et al. (2021). Anyway, this kind of masonry will not be considered in the present work.

4.1. Basic classification

The current classification makes a distinction between periodic and non-periodic textures. The periodic texture is characterized by blocks having equal size and placed in a regular pattern, as shown in Figure 4.1a, so that the position of each block may be determined by a linear combination of two vectors (indicated as v_1 and v_2 in the figure).

When dealing with non-periodic masonry textures, we define two different typologies: the first one is the quasi-periodic texture described in Falsone and Lombardo (2007), given by blocks of different size but arranged in such a way that we can identify masonry courses, i.e. the horizontal mortar joint are almost aligned, as can be seen in Figure 4.1b; it is worth noting that the blocks have almost a rectangular shape as in the case of the periodic texture. The second one is the chaotic texture, in which blocks of different size are arranged arbitrarily; moreover, the blocks can have a shape very far from the rectangular one (see Figure 4.1c).
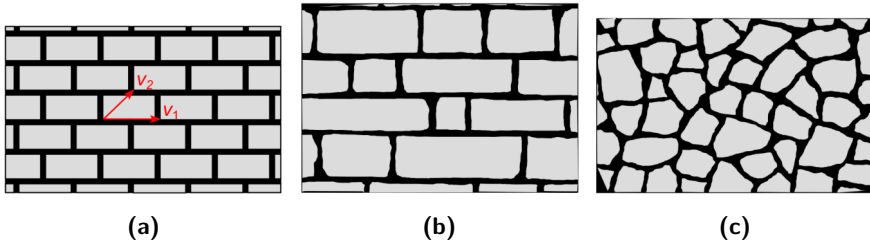
Figure 4.1: Masonry texture classification: (a) periodic, (b) quasi-periodic, (c) chaotic.

4.2.Proposed advanced classification

An advanced classification of the quasi-periodic masonry is here proposed. A periodic texture can be easily identified at sight and the same holds for a non-periodic texture but it is not straightforward to classify an irregular texture and so a simple algorithm is presented (see Fig. 4.3).

The first thing is to check at sight if the texture is periodic, then the horizontality of the mortar bed joints is checked and if this feature is not present then the texture is chaotic, otherwise the texture is quasi-periodic. Then the degree of bonding between the courses for the quasi-periodic texture can be evaluated. In order to do that, the key idea of minimum length path across the masonry panel used in Borri et al. (2020) is adopted and properly modified.

The paths of vertical minimum length along mortar joints are identified, first from the top to the bottom (red lines) and then from the bottom to the top (blue lines) as in Fig. 4.2(a) and the mean value of the length of these paths (p_i) is evaluated.

In the process of tracking paths the priority is to draw first the descending paths and then the ascending ones. This reason for this choice is that the failure mechanism involves mostly the upper part of the masonry and so the geometry of that part is more representative of the structural behaviour.

The mean local aspect ratio (AR) is then evaluated (defined as the ratio between the width and the height of each element) is evaluated and periodic masonry structure having the same mean aspect ratio is defined. For this periodic texture the length of the path (p_p) is evaluated as in Equation 4.1:

$$p_p = H + \left(\frac{H}{h} - 1\right) \cdot \frac{w}{2} \tag{4.1}$$

with H, w and h defined in Fig. 4.2(b).

If the ratio between the dimensions of the elements and the wall size is small, the formula becomes:

$$p_p = H \cdot \left(1 + \frac{AR}{2}\right) \tag{4.2}$$

These formulas have been deduced by simple geometrical observations and by merging the concepts of aspect ratio and minimum path length in a recent work in progress and so they were not in literature.

The value p is then evaluated; it's defined as the ratio between p_i and p_p. The value p makes a distinction between an Irregular Bond (IB) and a Stretcher Bond (SB). If the value is lower than 0.8 we are in the first case because a small ratio means the vertical joints are aligned, otherwise the elements are well staggered and we are in the second case.

In the end, the coefficient of variation of the heights of the courses is evaluated (v) and it can be used as a threshold to make a distinction between Similar height Stretcher Bond (SSB) and a Different height Stretcher Bond (DSB).

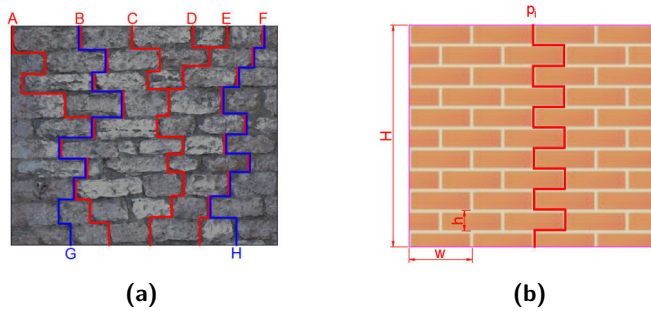**Figure 4.2:** Evaluation of the paths through masonry (a) Shortest paths for a portion of irregular masonry, (b) Path for a corresponding periodic texture with the same mean aspect ratio
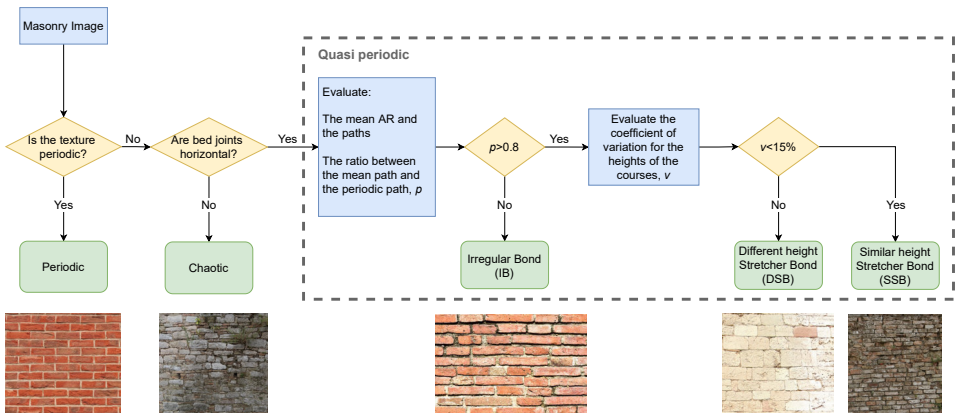

Figure 4.3: Proposed classification algorithm flowchart

4.2.1. Examples of classification of textures

Here the classification explained in 4.2 is applied to three different textures in order to show the procedure.

First of all an image is selected and properly scaled to make its height unitary. Then the shortest paths are traced and every value is collected (indicated with capital letters in Fig. 4.4).

SSB texture (Fig. 4.4(a))

The mean local AR of this texture is 1.69 and so the path for a periodic texture with the same local aspect ratio (p_p) is:

$$p_p = H + \left(\frac{H}{h} - 1\right) \cdot \frac{w}{2} = 1 + \left(\frac{1}{0.1} - 1\right) \cdot \frac{0.169}{2} = 1.76$$

The mean of the shortest path evaluated for this texture is:

$$p_i = 1.59$$

so the p value is:

$$p = \frac{p_i}{p_p} = \frac{1.59}{1.76} = 0.90 > 0.80$$

that is bigger than 0.8 so the texture is similar to a stretcher bond and the v parameter has to be evaluated.

So the height of each course is collected and the mean value (m) and the standard deviation (σ) are evaluated:

$$m = 0.1005$$
$$\sigma = 0.0137$$

so the coefficient of variation of the height of the courses (v) is:

$$v = \frac{\sigma}{m} = \frac{0.0137}{0.1005} = 0.1366 = 13.66\% < 15\%$$

so the texture is a Similar height Stretcher Bond or SSB.

DSB texture (Fig. 4.4(b))

The mean local AR of this texture is 1.71 and so the path for a periodic texture with the same local aspect ratio (p_p) is:

$$p_p = H + \left(\frac{H}{h} - 1\right) \cdot \frac{w}{2} = 1 + \left(\frac{1}{0.125} - 1\right) \cdot \frac{0.171}{2} = 1.60$$

The mean of the shortest path evaluated for this texture is:

$$p_i = 1.58$$

so the p value is:

$$p = \frac{p_i}{p_p} = \frac{1.58}{1.60} = 0.98 > 0.80$$
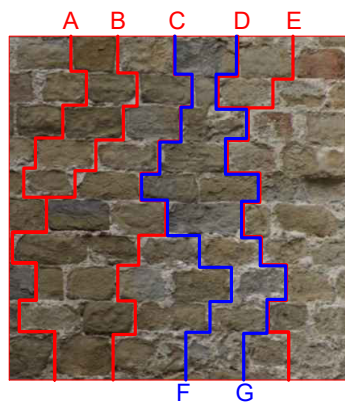
(a) A = 1.61, B = 1.64, C = 1.53, D = 1.59, E = 1.57, F = 1.59, G = 1.60
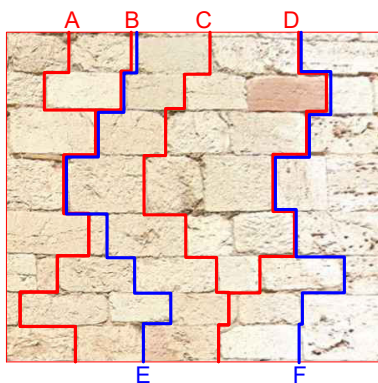
(b) A = 1.80, B = 1.55, C = 1.43, D = 1.47, E = 1.63, F = 1.64
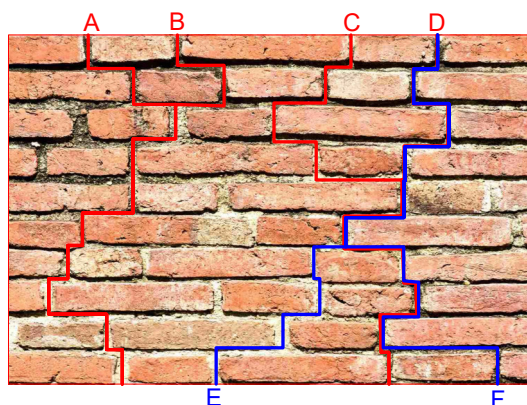
(c) A = 1.82, B = 1.85, C = 2.08, D = 1.79, E = 1.87, F = 2.07

Figure 4.4: Length of the shortest paths for different examples of application of the classification procedure: (a) SSB texture; (b) DSB texture; (a) IB texture

that is bigger than 0.8 so the texture is similar to a stretcher bond and the v parameter has to be evaluated.

So the height of each course is collected and the mean value (m) and the standard deviation (σ) are evaluated:

$$m = 0.1238$$
$$\sigma = 0.0241$$

so the coefficient of variation of the height of the courses (v) is:

$$v = \frac{\sigma}{m} = \frac{0.0241}{0.1238} = 0.1947 = 19.47\% > 15\%$$

so the texture is a Different height Stretcher Bond or DSB.

IB texture (Fig. 4.4(c))
The mean local AR of this texture is 3.48 and so the path for a periodic texture with the same local aspect ratio (p_p) is:

$$p_p = H + \left(\frac{H}{h} - 1\right) \cdot \frac{w}{2} = 1 + \left(\frac{1}{0.1} - 1\right) \cdot \frac{0.348}{2} = 2.57$$

The mean of the shortest path evaluated for this texture is:

$$p_i = 1.91$$

so the p value is:

$$p = \frac{p_i}{p_p} = \frac{1.91}{2.57} = 0.74 < 0.80$$

that is lower than 0.8 so the texture is an Irregular Bond or IB and there's no need to evaluate the v parameter.

4.3. Script for the generation of quasi-periodic textures

In order to have samples to use in the parametric analysis, a script has been developed. It allows to generate quasi-periodic masonry samples given this input parameters:

- local aspect ratio (AR)

- number of elements in the horizontal direction (N_x)

- mean width of the elements $(\bar{w})$

- coefficient of variation for the height of the courses (v)

- coefficient of variation for the width of the elements (v_w)

- a tolerance parameter that indicates the minimum distance between two vertical mortar joints in adjacent courses (Tol)

For the random generation of the width and the height of the elements a lognormal distribution is used. It allows to avoid negative values even if it has the drawback of asymmetry of distribution around the mean value. Anyway also the Gaussian distribution has been tested getting rid of negative values when they occur and the same conclusion can be drawn.

Once the local aspect ratio (AR) of the elements and the number of the elements in the horizontal directions (AR) are defined, a window that is $(N_x \cdot \bar{w})$ wide and $(N_x \cdot \bar{w} \cdot AR)$ high is generated and elements that exceed this borders are properly cut in order to obtain a rectangular shape. In order to achieve this, first all the height of the courses is generated and the process stops when the maximum height is reached and then each course if filled with elements whose width is also randomly generated.

For the Irregular Bond (IB) the value of v is set to 0 in order to analyze the variation just with the v_w parameter that is set to 0.3.
For the Similar height Stretcher Bond (SSB) v is set to 0.05 and v_w is set to 0.2
For the Different height Stretcher Bond (DSB) v is set to 0.2 and v_w is set to 0.2

The tolerance parameter is $\bar{w}/5$ for the SSB and DSB while for the IB is 0 (e.g. vertical masonry joints may be aligned). That is summarized in Table 4.1.

Parameter	SSB	DSB	IB
v	0.05	0.20	0
v_w	0.20	0.20	0.30
Tol	$\bar{w}/5$	$\bar{w}/5$	0

Table 4.1: Parameters used for the generation of quasi-periodic masonry.

4.4. Texture acquisition by images

Every non-periodic masonry has a unique texture and so the evaluation of the exact arrangement of stones and mortar joints may be difficult. For this reason a method to represent the texture in an analysis model can be useful. One way of proceeding is through digital processing of images. The texture of the wall can be captured in a image to identify the arrangement of the masonry joints (and consequently the position and shape of each block) and/or some geometrical parameters necessary to calibrate the homogenization approach

In Cavalagli et al. (2013) for example the texture is obtained from a colour photograph. Figure 4.5(a) shows an example of the conversion from greyscale

image to binary filtered image, in this case used by Cavalagli et al. (2013) to inform an homogenization-based analysis, while in Fig. 4.5(b) the bonding pattern is automatically identified from the binary image via a script, for use in a rigid block analysis.
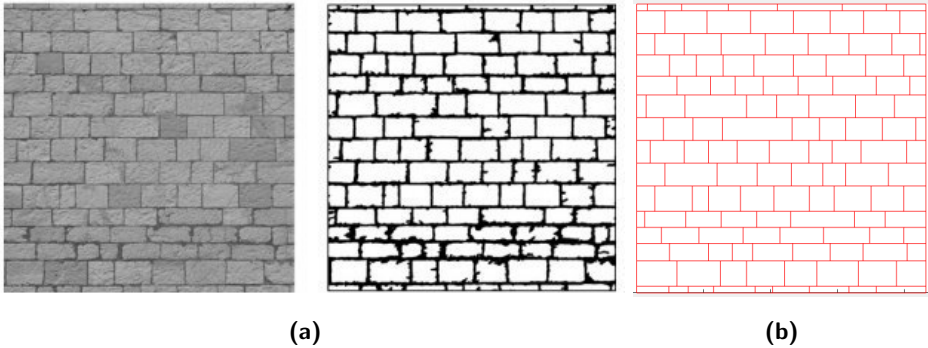

(a)   (b)

Figure 4.5: Automated acquisition from images: (a) Grey scale image and associated binary image obtain by filtering, (b) Equivalent bonding pattern obtained

If the masonry facade is plastered instead this approach is not viable and so it is necessary to resort to thermographic images. Thermographic images are helpful because they allow a masonry bonding pattern to be determined under a layer of render or other adornment, without the need for damaging intrusive work. In this case part of the electromagnetic radiation emitted from a body (in the infrared range) depends on the temperature of the body itself; when a heat flux passes through the wall, since the thermal conductivity of mortar and units is different, the temperature of the two phases will be different too and so the location of these two elements can be identified. Fig. 4.6, extracted from Cluni et al. (2020), shows the effect of the digital processing algorithm that transforms the thermographic image into a more clear black and white one. While this is enough for an assessment of the mechanical properties of the masonry via homogenization, this is not true if the exact pattern of discontinuities needs to be represented in the DLO analysis and so the same procedure shown in Fig. 4.5 must be used.

Moreover in Cavalagli et al. (2018) the acquisition of images of non-periodic texture is used to create a statistical equivalent periodic texture (see Fig. 4.7) and then determine the failure surface and the elastic properties.
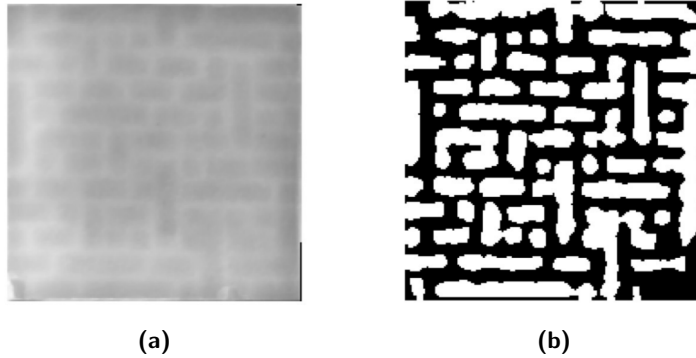
Figure 4.6: (a) Gray-scale image obtained from thermal imaging camera (a), black and white corresponding image
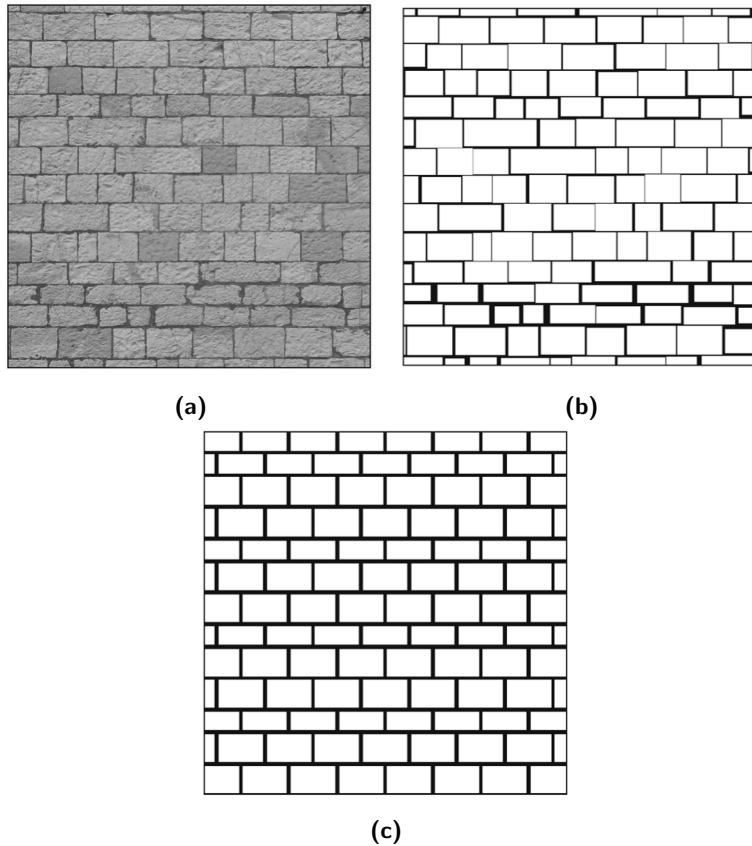

Figure 4.7: Realisation of a statistical equivalent periodic texture (a) Gray-scale image of a quasi-periodic wall; (b) black and white corresponding image; (c) Statistically Equivalent Periodic Texture

5. Parametric analysis

A parametric analysis taking into account several parameters is conducted. In Section 5.1 three different textures, one for each kind described by the current classification are considered, and the failure load of the panel under a seismic action is evaluated when the height of the panel (and so the global Aspect Ratio) varies.

In Section 5.2 other parameters are considered such as the effect of cohesion in mortar joints, the effect of the local Aspect Ratio and the Effect of non-rigid elements is considered. Since this parameters affect the outcome for all the texture, a periodic texture is adopted for the sake of simplicity in this section.

In Section 5.3 for the new classification, square shaped panels of periodic and quasi-periodic textures are analysed both for a rigid block and an homogenized DLO formulation in order to asses the influence of the texture.

Finally in Section 5.4 some examples of wall with openings are shown for different kind of textures to show that the same considerations hold also in this case.

5.1.Variation with the global Aspect Ratio

A parametric analysis with the aim of asses the influence of the textures has been conducted, considering blocks as rigid and cohesionless mortar with associative friction. In this section, the former classification (described in Section 4.1) is considered and so three different configurations of masonry are taken in account.

- a periodic texture, in which equal blocks are arranged according to a periodic pattern, and so it is possible to identify two vectors which through a linear combination are able to locate every block.

- a quasi-periodic texture, in which blocks can have different width and height, but they are arranged so that each adjacent block has the same height. So it is possible to identify courses on the texture, and we have continuity on the horizontal mortar joints. The vertical mortar joints between two adjacent courses cannot be aligned.

- a chaotic texture, in which the width and the height of the blocks is random and it is not possible to identify horizontal courses anymore, so vertical mortar joints may be aligned.

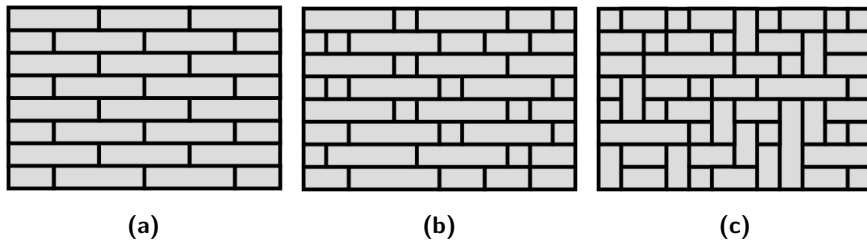An example of these texture typologies is shown in Figure 5.1.

| (a) | (b) | (c) |

Figure 5.1: Masonry texture examples for the current classification: (a) periodic, (b) quasi-periodic, (c) chaotic.

For the sake of clarity it is highlighted that in the case of chaotic texture, the blocks have been reduced to rectangles to simplify the analysis especially for the future realization of experimental tests. The height and the width of the blocks is then modular, which is not true in general, but again this is due to the fact that experimental tests on sample walls, realized with half height UNI brick and its subdivision, are in plan Cluni et al. (2019).

For each of them, the variation of the load multiplier, λ, with the ratio between the height and the width of the wall is evaluated and the presence of a vertical load above the top row, q, is considered. Each elementary volume of the masonry dV is subject to a vertical body force proportional to the specific weight γ, $\gamma\,dV$, and an horizontal body equal to $\lambda\gamma\,dV$. The load q has the dimension of a force over a surface whereas the body force is a force per unit volume. The components for dead and live loads body forces are evaluated for each potential discontinuity as follows: the weight of the strip lying above the discontinuity is evaluated by multiplying the surface for the density and then it is divided into a shear and a normal component depending on the inclination.

In the following we assumed $\gamma = 1$ and unitary thickness of the wall. It is worth noting that when $q > 0$ a load equal to λq is applied horizontally on the top of the wall.

The aim of this parametric analysis was to assess the influence of geometrical and mechanical parameters involved in the model, so the geometry of the blocks has been simplified as follows: each block has the shorter dimension equal to
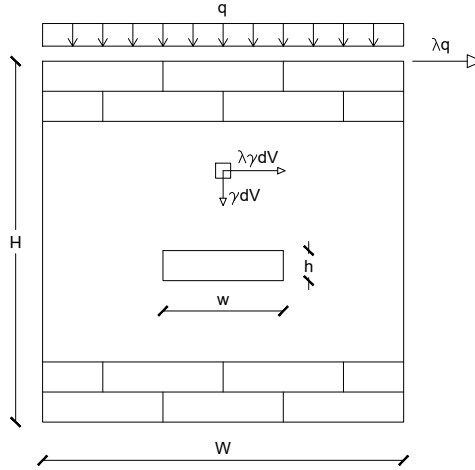
Figure 5.2: Geometrical parameters of the wall and of the blocks and applied forces.

0.5 and the other one varies from 0.5 to 2 by steps of 0.5 randomly. The discontinuities are considered to occur only along mortar joints i.e. the blocks are rigid. The geometrical parameters and the forces are shown in Figure 5.2. The parameter H/W and w/h can also be referred as global Aspect Ratio and local Aspect ratio (or AR) respectively.

Periodic masonry

For the first kind of texture, the periodic one, as we may expect, there is a perfect symmetry of failure mechanism and the same value of the failure multiplier for both directions. When $q = 0$, for H/W values below ≈ 1.25 the mechanism is translational, otherwise the mechanism is rotational, as can be also assessed with a simplified analytical calculation (see 5.2.2). For greater values of q the threshold between the two mechanisms reduces as q increases, a shown in Figure 5.3. It is worth noting that when $q > 0$ and horizontal load equal to λq is applied to the top row.

In Figure 5.4 the layout of mortar joints subjected to displacements and rotations for the case $H/W = 2$ and $q = 0$ is shown. For the sake of clarity it is specified that this figure and the following ones in the work showing the texture and the failure mechanism are not labelled because the dimensions are expressed in units. Red lines represents relative shear displacements and green lines represents relative rotations, so each portion delimited by these lines defines a part of the wall that translates or rotates with respect to the other parts. In Figure 5.4 (c) for example a great block (from height 2 to height 12) rotates clockwise with respect to the the basis and other minor rotations are
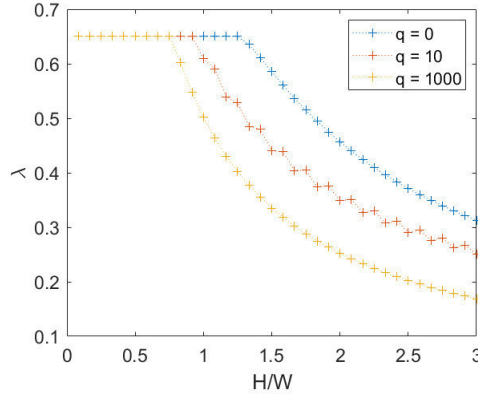
Figure 5.3: Periodic masonry, failure multipliers for different values of vertical load q.

present at a lower height.

(a)   (b)   (c)
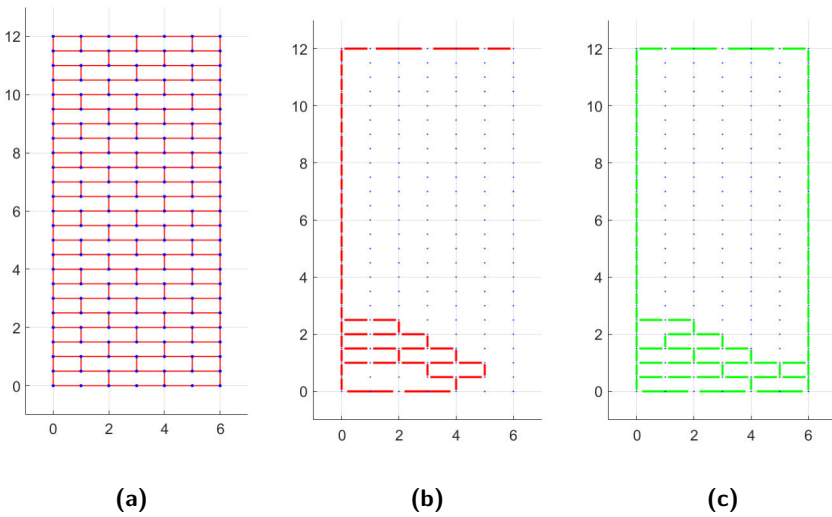
Figure 5.4: Periodic masonry with $H/W = 2$: (a) texture, (b) mortar joints with displacements $s \neq 0$ for right oriented force, (c) mortar joints with rotations $w \neq 0$ for right oriented force. (Dimensions expressed in units).

Quasi-periodic masonry

In this case the failure multiplier and the associated layout of rotations and translations depends on the seismic action orientation, as shown in Figure 5.5.

If the average value between the right and the left outcome is evaluated, a more regular and significant relation is obtained as shown in Figure 5.6.

The threshold between the pure translational mechanism and the rotational

(a)   **(b)**
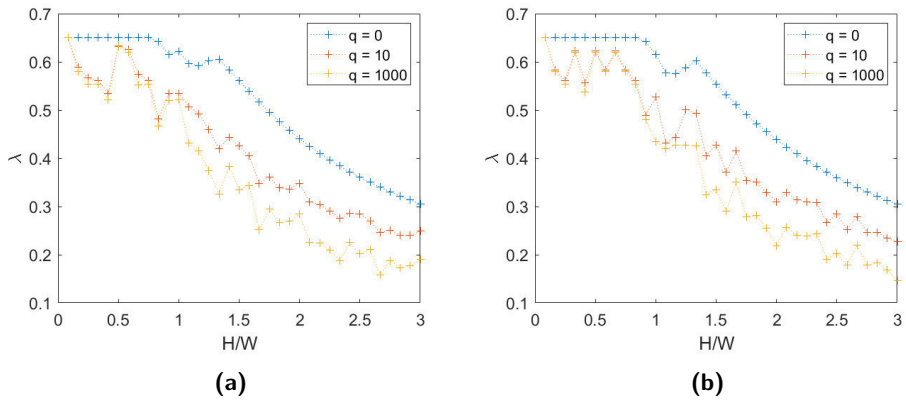
Figure 5.5: Quasi-periodic masonry, failure multipliers for different q: (a) right-oriented force, (b) left-oriented force.
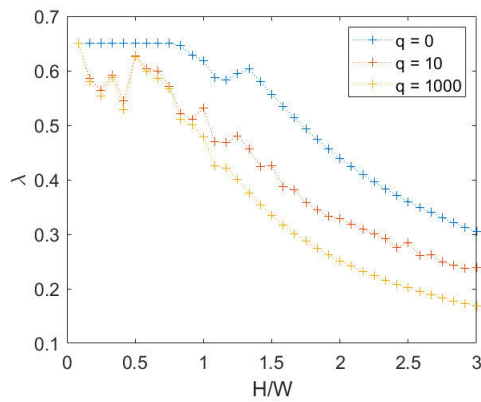
Figure 5.6: Quasi-periodic masonry, failure multipliers for different q: mean values for right- and left-oriented forces.

mechanism is not so clean in this case, due to the incomplete participation to rotation of the wall width (i.e. local mechanisms). This happens for H/W between 0.8 and 1.25 in the case of $q = 0$ and it is shown through an example of the layout of translational and rotational discontinuity for quasi-period masonry, $q = 0$ and two different H/W ratios respectively equal to 1, Figure 5.7, and 2, Figure 5.8.

(a)   (b)   (c)

Figure 5.7: Quasi-periodic masonry with $H/W = 1$: (a) texture, (b) layout of displacements (s) for right oriented force, (c) layout of rotations (w) for right oriented force. (Dimensions expressed in units).

(a)   (b)   (c)
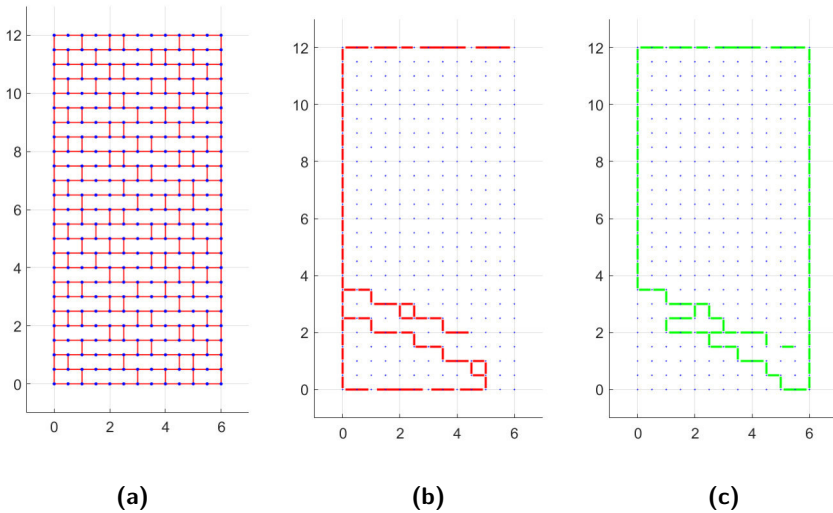
Figure 5.8: Quasi-periodic masonry with $H/W = 2$: (a) texture, (b) layout of displacements (s) for right oriented force, (c) layout of rotations (w) for right oriented force. (Dimensions expressed in units).

For a more clear view of the outcome, only mortar joints subjected to displacements ans rotations greater than 1% of the maximum values are shown. Moreover, the more irregular layout of discontinuities makes the masonry prone

to a partial failure mechanism. The latter feature isn't present in the periodic masonry where the mechanism changes abruptly from pure translational to a rotational global mechanism. The presence of a load above the wall makes partial rotational mechanisms occur even for small H/W ratios. This is because this load has an horizontal component that is proportional to the load itself and not to the mass of the wall and so when the H/W ratio is small, the seismic action modelled by a body force it is not sufficient to cause the overturning but the contribute of this load is significant instead. In other words the center of the mass of the structure moves up due to the mass associated to the load.

Chaotic masonry

In the case of chaotic masonry, the failure multiplier and layout of relative displacements and rotations depends on direction too, since also this texture is not symmetric, as the quasi-periodic one. For this analysis, a single random wall with H/W equal to 3 has been generated, and for every smaller height the top rows have been removed regularizing the upper boundary, presenting an irregular surface due to the presence of non-horizontal mortar planes. Only the response for $q = 0$ is showed in Figure 5.9.
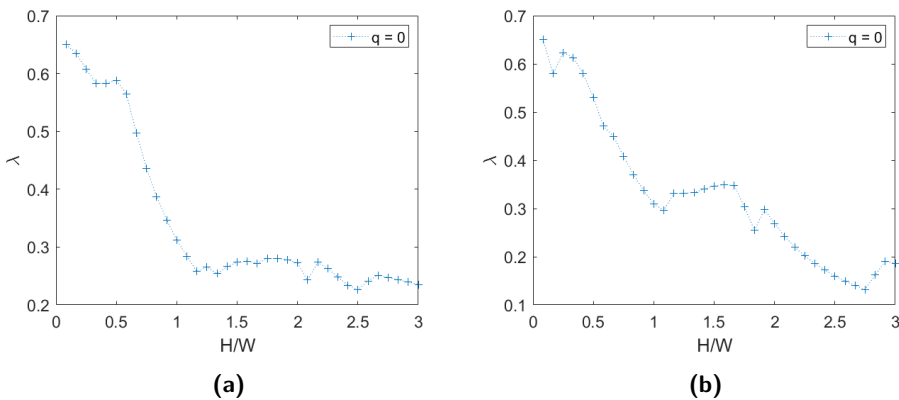
Figure 5.9: Chaotic masonry, failure multipliers for $q = 0$: (a) right-oriented force, (b) left-oriented force.

It may be notice that for chaotic masonry the failure multiplier is much lower, due to the presence of vertical oriented stone elements which are easier to overturn since they slenderness is higher (low values of the local aspect ratio w/h).

Moreover it is possible to see that in the case of chaotic texture, the failure mechanism involves just a part of the width of the panel even for high values of H/W. This is showed for $H/W = 2$ in Figure 5.10.

A comparison between the three different textures for $q = 0$ is showed in the Figure 5.11.
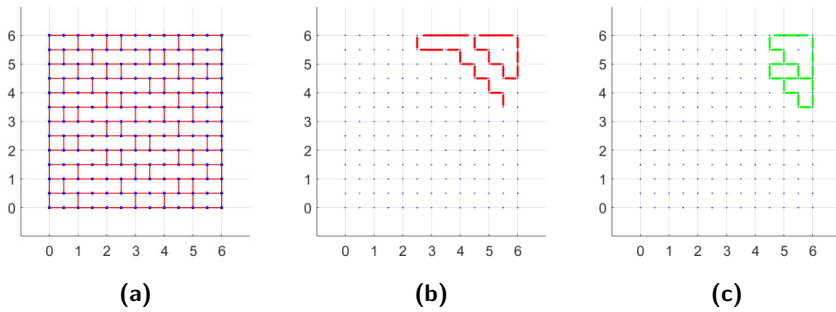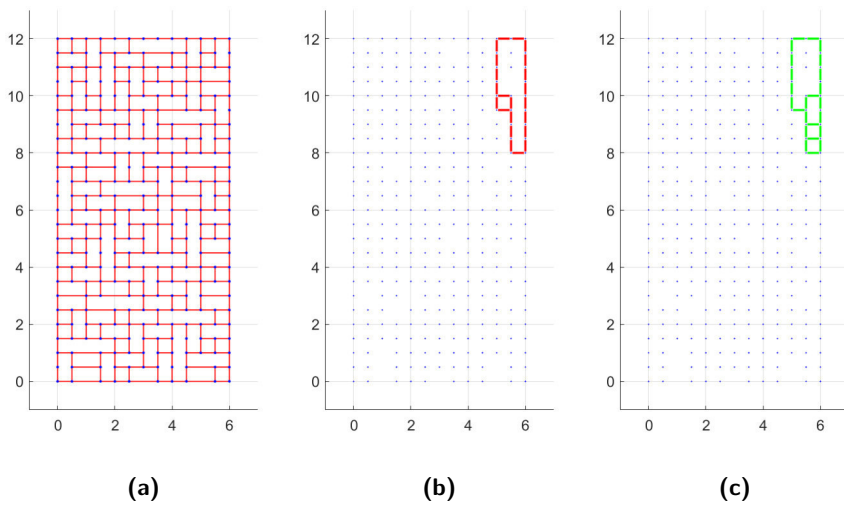
Figure 5.10: Chaotic masonry with $H/W = 2$: (a) texture, (b) layout of displacements (s) for right oriented force, (c) layout of rotations (w) for right oriented force. (Dimensions expressed in units).
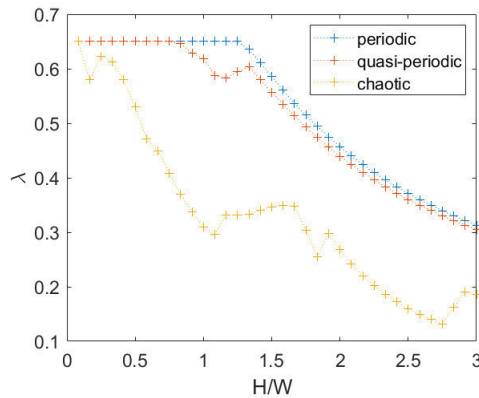

Figure 5.11: Comparison of failure multiplier at $q = 0$ for different textures (averaging the response to left- and right-oriented forces for quasi-periodic and chaotic textures).

From the figure it is clear that the effect of the difference between the periodic and quasi-periodic textures is relevant just in the transition between translation and rotation (for H/W values between 1 and 1.4) whereas for higher values of H/W a global rotational mechanism prevails and so the effect of shifting the vertical mortar joints position can be neglected.

For the sake of completeness it is specified that both for the quasi-periodic and the chaotic masonry just one sample is tested since the aim of this section was to highlight a general trend between the failure multiplier and the height of the panel for different textures. Of course this work could be extended generating many samples for each height and evaluating the mean values and the deviation.

5.2. Other aspects

5.2.1. Effect of cohesion in mortar joints

In the present Section the influence of cohesion in vertical mortar joints, c, is investigated. In particular, in all the analysis that follow c is unitary.

For the sake of simplicity only the case of periodic masonry is shown in the following figures so that other parameters such as the texture cannot influence the outcome. When just a translational mechanism is involved, the presence of cohesion provides an increase of the failure multiplier inversely proportional to the wall height (see 5.2.2)

When rotational mechanism occurs instead, the increase depends from the layout of relative displacements and rotations at failure. In Figure 5.12 it is possible to observe the values of the failure multiplier for $q = 0$. It is also possible to notice in the same figure that the influence of cohesion is negligible for an high global Aspect Ratio, where the mechanism is rotational.
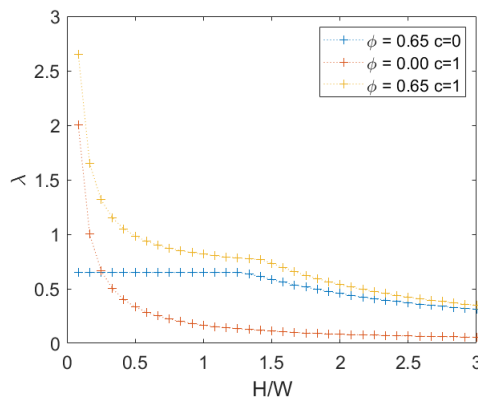
Figure 5.12: Periodic masonry, failure multiplier for different combinations of cohesion c and internal friction angle φ.

When the load on the top increases instead we can see that the presence of

cohesion is negligible due to the arise of rotational mechanism even for a small height/width ratio as explained in Section 5.1. This is visible in Figure 5.13
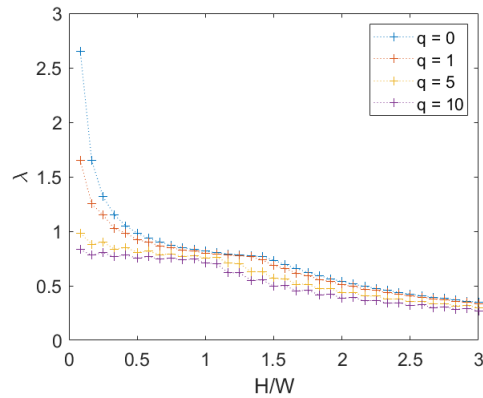
Figure 5.13: Periodic masonry, failure multiplier for $c = 1$ and a several set of loads q.

5.2.2.Effect of the local Aspect Ratio (AR)

We now take in account the variation of the local Aspect Ratio (AR) in both cases of absence and presence of cohesion. Several ratios were investigated with the following results. For the first case, see Figure 5.14a, it is observed that a lower local Aspect Ratio AR makes the rotational mechanism occur for a lower global Aspect Ratio H/W ratio due to the tendency of slender elements to be overturned, as can also be seen in the physical explanation subsection at the end of 5.2.2. When cohesion is present instead, see Figure 5.14b, it appears that AR does not affect the solution and the value of the H/W ratio associated to the transition from translational to rotational.

We note that the number of rows is constant and therefore the overall height of the panel increases as h increases.

Physical explanation

Two different failure mechanism for the wall are considered:

- translation of the entire wall slipping over the base;

- rotation of a portion of the wall around one of the edge of the base.

In the rotational mechanism, it is assumed that a portion delimited by a line inclined of ψ is involved, see Figure 5.15, where $\tan \psi$ is equal to the local Aspect Ratio (AR).

Adopting a Mohr-Coulomb criterion, in the case of translational mechanism we have that the value of λ at failure, λ_t, is given by

(a) **(b)**

Figure 5.14: Periodic masonry, failure multiplier for different values of the local AR : (a) $c = 0$, (b) $c = 1$.

Figure 5.15: Rotation mode failure mechanism of the wall.

$$\lambda_t \left(\frac{\gamma W H t}{W t} + q \right) = \left(c + \frac{\gamma W H t + q W t}{W t} \tan \varphi \right) \Rightarrow \lambda_t = \frac{c + (\gamma H + q) \tan \varphi}{\gamma H + q}$$

$$(5.1)$$

In the case of rotational mechanism, we have that the value of λ at failure, λ_r, is given by

$$\lambda_r \left(\gamma A h_g + q H \right) = \gamma A d_g + q \frac{W}{2} \Rightarrow \lambda_r = \frac{\gamma A d_g + q \frac{W}{2}}{\gamma A h_g + q H} \tag{5.2}$$
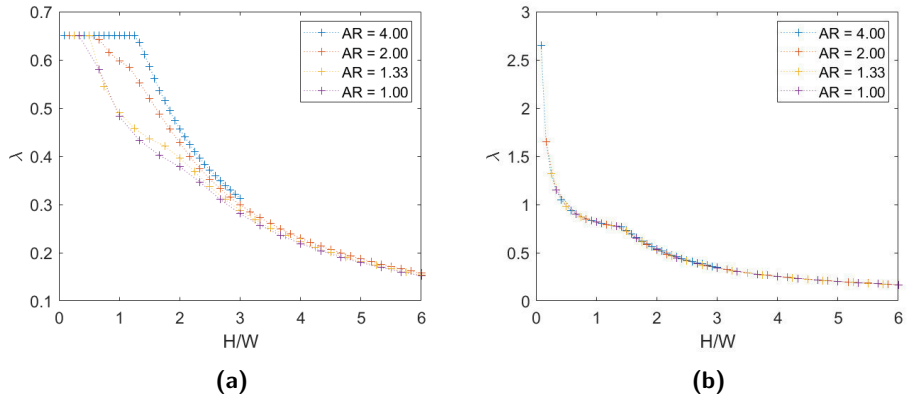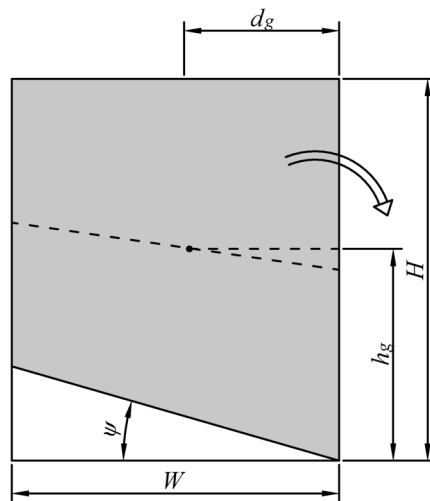
where A is the area of the portion of the wall involved in the rotation and (d_h, h_g) locate its centroid with respect to the pivot point:

$$A = \frac{W (2H - W \tan \psi)}{2} \tag{5.3}$$

$$d_g = \frac{W}{3} \frac{3H - W \tan \psi}{2H - W \tan \psi} \tag{5.4}$$

$$h_g = \frac{H}{2} + d_g \tan \psi \tag{5.5}$$

In the case $\gamma = 1$, $t = 1$, $c = 0$, $q = 0$ and $\tan \psi = AR = 4$ we have that $\lambda_r = \lambda_t$ for $H/W \approx 1.24$, while with $q = 10$ we have $\lambda_r = \lambda_r$ for $H/W \approx 1.06$, showing that as q increases the transition point decreases.

The values of λ_t and λ_r with the previously used values of γ, t, q, c and $\tan \psi$ are shown in Figure 5.16.

5.2.3.Effect of non-rigid elements

In all the previous mentioned models the cracks were supposed to occur only along mortar joints, so a rigid block approach was considered and therefore only the properties of mortar were considered. If the hypothesis of non-rigid blocks is considered instead, more potential discontinuities have to be modelled with different properties from the already present ones within the blocks. In a first step, a periodic masonry is considered, and the new discontinuities are selected to be just vertical and in the middle of the stone elements. The configuration is shown in Figure 5.17: blue lines represents mortar joints and the green ones the new potential discontinuities considered. A grid with joints spaced 1.0 in horizontal and 0.5 in vertical directions is used.

A Mohr-Coulomb criterion is adopted also to describe the stone elements. Several combinations of cohesion and friction for the blocks have been considered, letting the properties of the mortar constant ($c = 0$ and $\tan(\varphi) = 0.65$). The variation of the failure multiplier with these two parameters has been analysed in two different plots, as shown in Figure 5.18 for $H/W = 4/3$ and $q = 0$, and it led to some expected considerations.
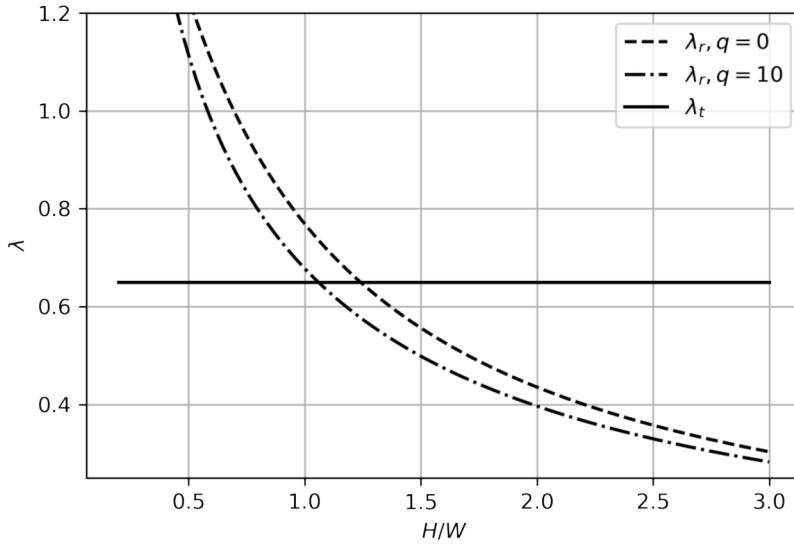
Figure 5.16: Values of λ_r and λ_t for various values of H/W and two different values of q.
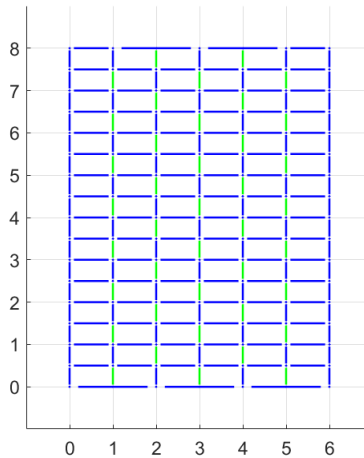

Figure 5.17: Potential discontinuities assuming non-rigid blocks: blue lines represent discontinuities belonging to mortar joints and the green ones discontinuities within the blocks. (Dimensions expressed in units).

Figure 5.18: Periodic masonry, failure multiplier for different values of cohesion c and internal friction angle φ of the blocks: (a) effect of variation of φ for different values of c, (b) effect of variation of c for different values of φ.

First of all, the failure multiplier cannot be higher than in the case of non-rigid blocks since adding more potential discontinuities can only lead to a decrease of energy required for the mechanism activation. As we may expect, when the mechanical properties of the stone elements are way better than the mortar joints ones, the failure multiplier doesn't change from the previous case and the mechanism will affect only mortar joints. Vice versa when these properties are close to the mortar joints ones, the masonry panel is equivalent to a rigid stones panel with half-length stone elements and with vertical mortar joints aligned. That can bring to a relevant decrease on the failure multiplier. Between these extreme cases, it is straightforward to notice that the failure multiplier increases both with stones cohesion and friction as expected. Moreover the influence of cohesion seems greater than the influence of friction.

To assess the influence of the mesh used for the identification of the potential discontinuities, a refined discretisation is also considered and the difference in terms of results with the latter one are discussed. In particular, a grid with dimension of 0.25 both in horizontal and in vertical direction is used, as shown in Figure 5.19.

This new configuration leads to results that are extremely close to the precedent discretisation ones, see Figure 5.20, except when brick cohesion is equal to 0.

5.3. Quasi-periodic masonry investigation for square shaped panels

In this section, square shaped panels samples (i.e. global Aspect Ratio $= 1$) are generated as explained in Section 4.3 and so they follow the new classification (Section 4.2).

For the analysis both the rigid block approach and the homogenized continuum approach are adopted, in order to test their suitability.
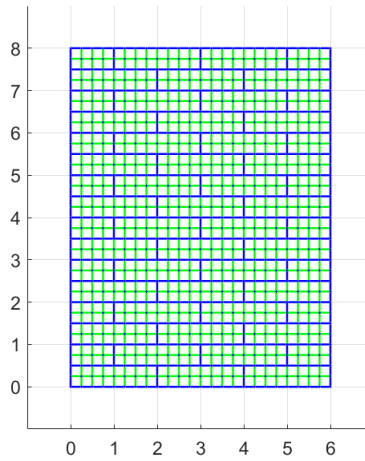
Figure 5.19: Potential discontinuities assuming non-rigid blocks with a refined discretisation: blue lines represents discontinuities belonging to mortar joints and the green ones discontinuities within the blocks. (Dimensions expressed in units).
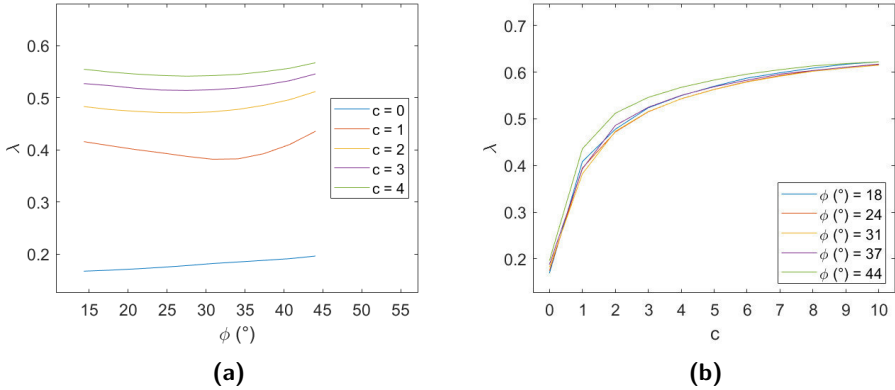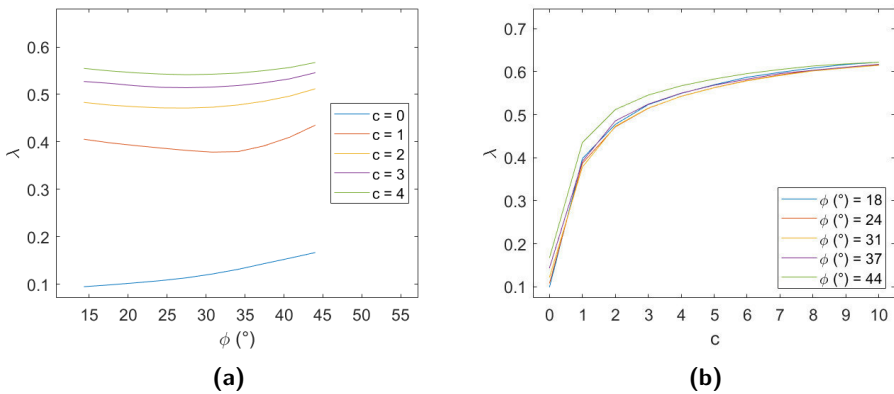

Figure 5.20: Periodic masonry, failure multiplier for different values of cohesion c and internal friction angle φ of the blocks: (a) effect of variation of φ for different values of c, (b) effect of variation of c for different values of φ.

5.3.1.Discretisation methods for homogenization

Since the homogenized method has been developed for the periodic texture, a way to adapt it to non-periodic texture must be found. For a non-periodic texture both the distribution of the mortar joints and the local Aspect Ratio vary throughout the panel. In this study it has been decided to detect the variation of the local Aspect Ratio via several discretisation methods explained below.

Statistical methods

The non-periodicity in masonry walls can be converted into equivalent periodicity via statistical means. Statistical methods provide a means of converting non-periodic masonry walls into periodic problems that are solvable via the homogenized DLO formulation. Here three approaches are proposed.

- Uniform aspect ratio, Fig. 5.21(b). An equivalent periodic masonry wall is assumed, with block aspect ratio calculated as the mean value of the local aspect ratio of all blocks in a non-periodic masonry wall.

- Stratification, Fig. 5.21(c). The panel is divided into horizontal layers, where mean local aspect ratio is calculated in each layer.

- Sub-regions, Fig. 5.21(d). Similar to stratification, the panel is divided into predefined sub-regions instead. After discussing some options the decision was to consider only the elements that are totally included into the region for the evaluation of the mean Aspect Ratio.This method may be seen as the uniform aspect ratio method applied for different parts of the panel and it is useful to have an insight about the relation between number of elements and number of regions requested.

| (a) | (b) | (c) | (d) |
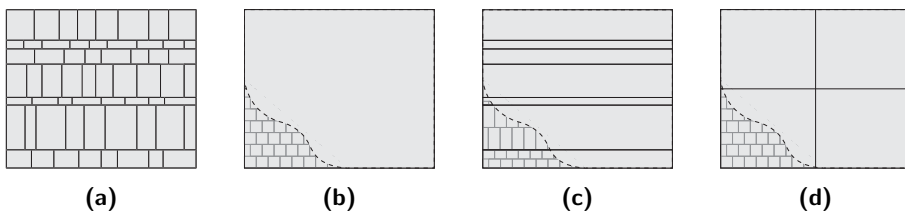
Figure 5.21: Statistical methods to convert a non-periodic masonry into a periodic problem for homogenized approach: (a) a non-periodic masonry wall; (b) using uniform aspect ratio in the entire domain; (c) stratified via multiple layers; (d) using sub-regions (four in this case)

Methods that map the Aspect Ratio

In this approach, the DLO homogenization method is adapted such that the aspect ratio (AR) used in the computation of the parameters for any given

discontinuity is based on an average aspect ratio determined from its path through the masonry texture. Fig. 5.22(a) illustrates example discrete block layouts of a masonry panel, and a series of grid points on a square grid. To each grid point is assigned the aspect ratio of the block in which it resides. Bilinear interpolation of the aspect ratio is then applied within each grid square giving contour plots as shown in Fig. 5.22(b). An average aspect ratio $\bar{AR}$ for a discontinuity is then computed by integrating the interpolated values of AR along the discontinuity and dividing by the discontinuity length (L) as follows:

$$\bar{AR} = \frac{1}{L} \left(\int_0^L AR \, dl \right) \tag{5.6}$$

The value of $\bar{AR}$ is then used in equation (3.10) in the homogenised formulation.

(a) (b)
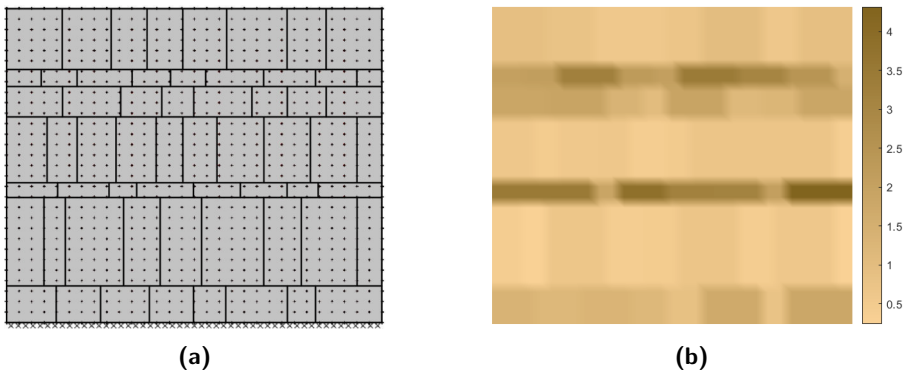
Figure 5.22: Method that maps the Aspect Ratio for a 30x30 rectangular grid: (a) Layout of elements and superimposed grid for courses with various Aspect Ratio; (b) Linear interpolated map of Aspect Ratio through the panel for courses with various Aspect Ratio. Note that the discretisation leads to sharp gradients between different aspect ratio blocks

5.3.2.Horizontal loading on plane masonry walls
Example of application

Here all methods described in Section 5.3.1 are applied to a sample of masonry to provide a clear image of the outcomes. The texture is generated through a script (see 4.3 for a detailed explanation).

For the example an Irregular Bond texture of AR = 3 having approximately 8x24 elements is chosen. The coefficient of friction used is 0.75 and the cohesion is 0. Results are shown in Table 5.1.

In all the homogenized models, the AR value is visually associated to a certain brown color intensity. The more bright the colour is, the less is the value of the aspect ratio. It is worth notice that the homogenized solution is independent

from the number of the elements and the results will be more close to the rigid models when the number of elements increases as it will be shown below.

Parametric analysis

First, two cases of square shaped walls are considered and results are shown in Table 5.2 and Table 5.3. The aspect ratio of the wall is 3 and the number of elements varies from 4x12 to 16x48. The coefficient of friction used is 0.75 and the cohesion is 0.

For each table, five different samples for each kind of texture are analysed and for each of them both the right and the left orientated seismic action is considered for an amount of 10 failure multipliers. Then, methods defined in Section 5.3.1 are applied and the minimum, maximum and mean values are shown.
Rigid block models with associative friction are also considered and results are compared to the homogeneous methods. Differences between methods are then discussed to point out that some methods are suited for certain textures and others are not.

The irregular bond has the lower values for the failure multiplier as expected and the mean value is always lower than the periodic one. Low elements samples have a high variability between the minimum and the maximum value. Low elements samples also have an high variability compared to the periodic texture the 4x12 sample with aspect ratio 3 seems to be the more sensitive to an irregular texture since also the maximum values are lower than the periodic values.

Since a pattern shows that the texture is negligible when the dimension of the elements is small compared to the size of the wall, another analysis has been carried on, making the number of the elements increase progressively and collecting the results for a rigid block analysis.

For this purpose, square walls with aspect ratio 3 are considered, the number of elements varies from 4x12 to 20x60 and for each texture the minimum, the maximum and the mean values of 5 samples randomly generated are evaluated. Mean values are shown in Fig. 5.23 and it is clear that the Irregular Bond has generally the lowest value of the failure multiplier.

This is because for the SSB and the DSB texture, exchanging the order of the courses has an effect when the single case is considered as shown in Fig. 5.24 but when several samples are analysed and the mean value is evaluated, the effect of variation with respect to the periodic texture is negligible as shown in Fig. 5.25 for the DSB case. It is possible to notice that the mean values for the DSB texture almost overlap the periodic outcome except when few elements are involved.

In Fig. 5.26 comparison between methods and textures are shown. The "uniform AR" curve is obtained through the regions method for just one region. The "original AR" curve instead is the curve corresponding to the aspect ratio

Table 5.1: Horizontal loading on plane masonry walls: Example of application, outcome for all the methods for both seismic direction orientation

Dir.	rigid	stratification	uniform AR	2x2 regions
left				
	$\lambda = 0.5592$	$\lambda = 0.5087$	$\lambda = 0.4823$	$\lambda = 0.4876$
right				
	$\lambda = 0.6105$	$\lambda = 0.5087$	$\lambda = 0.4823$	$\lambda = 0.4836$
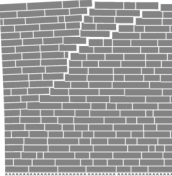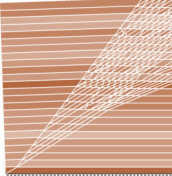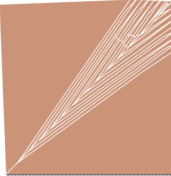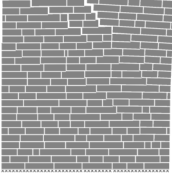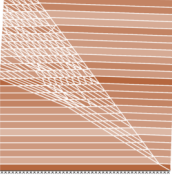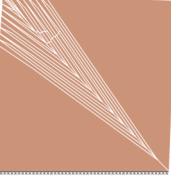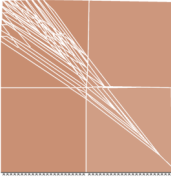
Dir.	3x3 regions	10x10 maps	20x20 maps
left			
	$\lambda = 0.4786$	$\lambda = 0.4788$	$\lambda = 0.4871$
right			
	$\lambda = 0.4729$	$\lambda = 0.4982$	$\lambda = 0.4804$
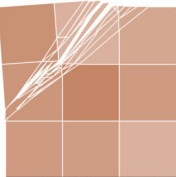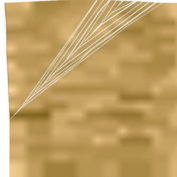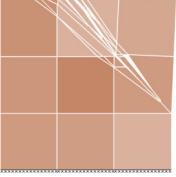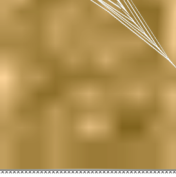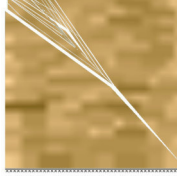
Table 5.2: Horizontal loading on plane masonry walls: Parametric analysis.
Square wall with AR 3 and 16x48 elements.
For each texture 5 samples and both seismic action orientation are considered and the
minimum, maximum and mean values of the failure multiplier are shown

Texture	Rigid blocks	Homogenized			
		Uniform aspect ratio	Stratif.	Sub-regions	Aspect ratio mapping method
Periodic	0.5455	0.4924	0.6863	(2x2) 0.4926	(10x10) 0.4940
				(3x3) 0.4951	(20x20) 0.4942
SSB-min	0.5441			(2x2) 0.4935	(10x10) 0.4928
SSB-max	0.5541	0.4924	0.7123		
SSB-mean	0.5505			(3x3) 0.5029	(20x20) 0.4931
DSB-min	0.5348			(2x2) 0.4963	(10x10) 0.4955
DSB-max	0.5629	0.4924	0.7239		
DSB-mean	0.5472			(3x3) 0.5029	(20x20) 0.4873
IB-min	0.5264			(2x2) 0.4902	(10x10) 0.4596
IB-max	0.5555	0.4924	0.7069		
IB-mean	0.5424			(3x3) 0.4909	(20x20) 0.4985

Table 5.3: Horizontal loading on plane masonry walls: Parametric analysis.
Square wall with AR 3 and 4x12 elements.
For each texture 5 samples and both seismic action orientation are considered and the
minimum, maximum and mean values of the failure multiplier are shown

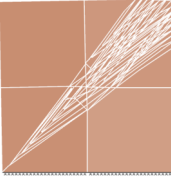| Texture	Rigid blocks	Homogenized			
		Uniform aspect ratio	Stratific.	Sub-regions	Joint position mapping methods
Periodic	0.712	0.4924	0.5048	(2x2) 0.4776	(10x10) 0.4871
				(3x3) 0.4592	(20x20) 0.4908
SSB-min	0.6358			(2x2) 0.4640	(10x10) 0.4745
SSB-max	0.7299	0.4924	0.5146		
SSB-mean	0.6879			(3x3) 0.4382	(20x20) 0.4719
DSB-min	0.6568			(2x2) 0.4536	(10x10) 0.4813
DSB-max	0.7069	0.4924	0.4951		
DSB-mean	0.6806			(3x3) 0.3936	(20x20) 0.4839
IB-min	0.5951			(2x2) 0.4617	(10x10) 0.4304
IB-max	0.7026	0.4924	0.5239		
IB-mean	0.6415			(3x3) 0.4398	(20x20) 0.4216

Figure 5.23: Horizontal loading on plane masonry walls: Parametric analysis. Comparison between textures for a rigid block analysis with associative friction.
SSB = Similar height Stretcher Bond texture
DSB = Different height Stretcher Bond texture
IB = Irregular Bond texture

(a)   (b)   (c)
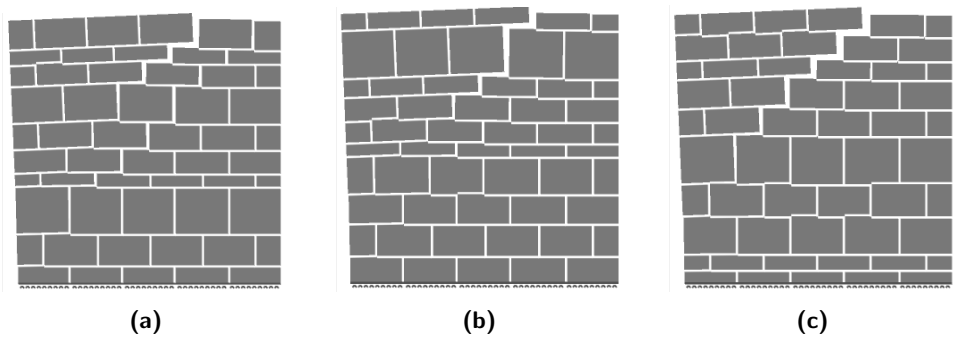
Figure 5.24: Rigid block analysis for a DSB texture and three different order of courses
(a) First order: Failure multiplier $= 0.516$; (b) Second order: Failure multiplier $= 0.5376$; (c) Third order: Failure multiplier $= 0.499$
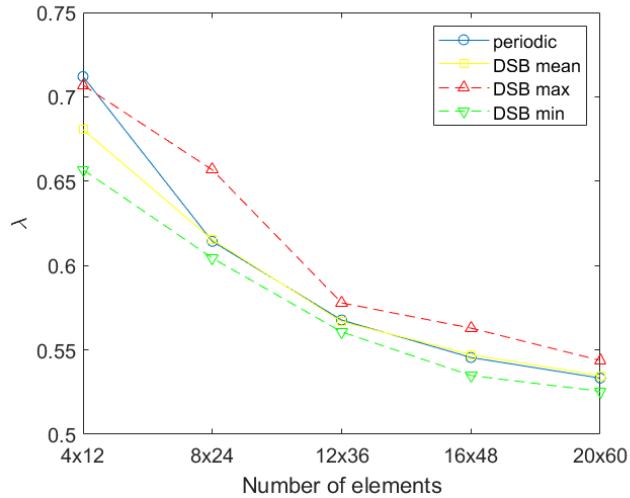
Figure 5.25: Comparison between the mean, the minimum and the maximum value for the DSB texture and the periodic outcome.

chosen at the beginning as input for the sample generation script. This values aren't the same for the presence of boundary elements that generally have a lower AR and so they globally reduce the AR evaluated in the regions models. This effect becomes negligible for an high number of elements since the effect of boundary elements is less important. The stratification method returns values that are always above the "original AR" values. The sub-regions method with 4 regions (2x2) rapidly converges to the value of the uniform aspect ratio method when the number of elements increases since each region contains more elements and so mapping irregularities and different aspect ratios is less effective. For this reason in the case of 9 regions (3x3) for a small number of elements we have a value that is far from the "original AR" value. It may be notice that in this case, even for a small number of elements the failure multiplier rapidly tend to the value of the "original AR".

Moreover, in this graphs the mean value between the right oriented and the left oriented seismic force is shown, since when samples are built in this way the outcome is not highly dependent on the direction. The texture that shows the higher dependence on the direction is the IB for which the different outcome is shown in Fig. 5.27.

Non-uniform distribution of the Aspect Ratio

In the previous section a parametric analysis was carried on starting from samples randomly generated through a script. This has 2 implications: first, the AR of the elements is homogeneously distributed throughout the panel and second, when the number of elements is very high, the mean AR will tend
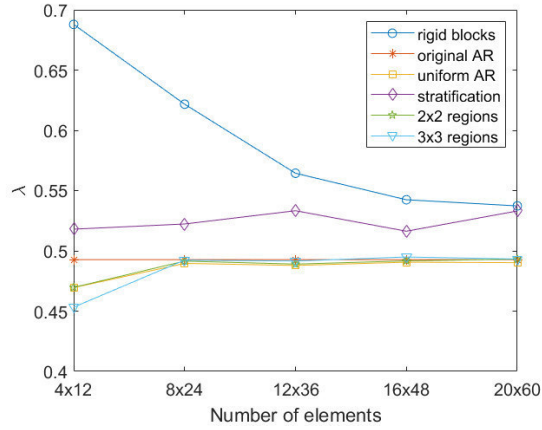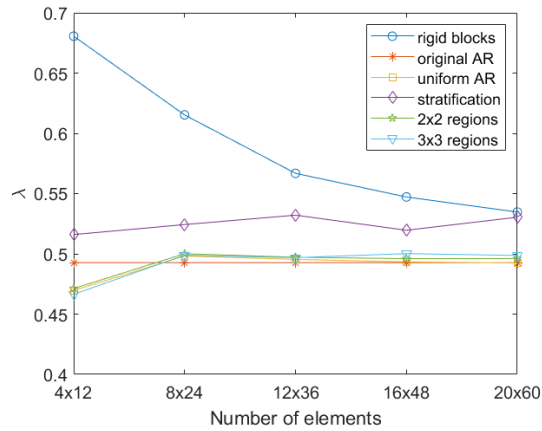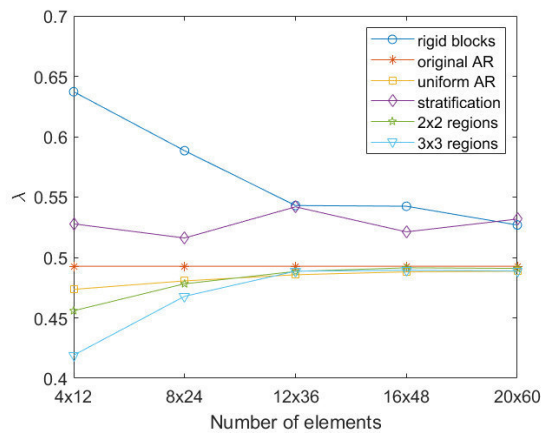
Figure 5.26: Horizontal loading on plane masonry walls: Parametric analysis.
(a) comparison between methods for a SSB texture; (b) comparison between methods
for a DSB texture; (c) comparison between methods for an IB texture.
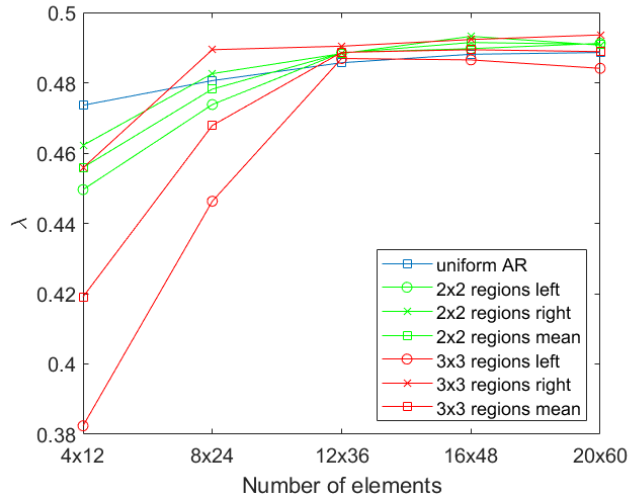
Figure 5.27: Horizontal loading on plane masonry walls: Parametric analysis. Dependence on the orientation for the IB texture

to the "original AR" value. Existing masonry instead does not always have this feature because it is often formed by elements with certain values of the AR that are not smeared throughout the panel but they have a certain spatial correlation due to the builder decisions and necessities. In these cases, using a uniform AR or regions that are not representative of the problem may lead to an incorrect result. To overcome this problem, there are two possible solutions. The first one is increasing the number of regions until they provides a correct representation of the problem and the second one is using a method that maps the AR. A straightforward example is presented in this section, to outline how with the second method is not necessary to know in advance the distribution of the AR in the panel because it will be automatically detected by a grid and the AR will be defined continuously by linear interpolation. It consists in a panel that has the top right quarter of mean AR 1 and the rest of mean AR 3. An example for the equivalent 12x36 number of nodes of the previous section is shown in Fig. 5.28

In this case it is easy to individuate the minimum number of sub-regions necessary to discretize the problem accurately is a 2x2 but in general, if the distribution and the shape of inclusions is not so neat, a pre-analysis is necessary, increasing the number of regions gradually to see when it fits the problem as will be shown in the Fig. 5.29 for this simple case. Moreover, it should be notice that if we reduce the size of the windows too much we will always find difference in the mean aspect ratio because the number of the elements within the regions will be low and not representative of the original AR of the panel. The results for an IB textures are shown in Fig. 5.30 Due to the asymmetry of
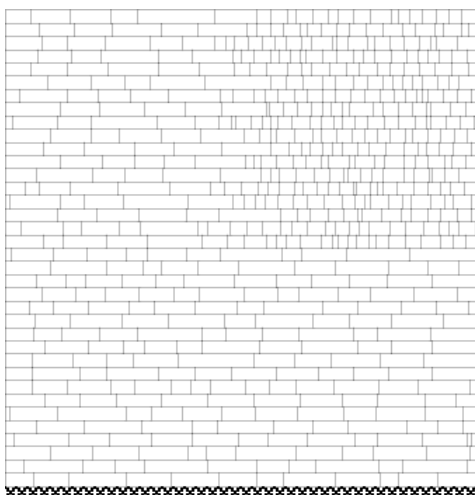
Figure 5.28: Non-uniform distribution of the Aspect Ratio: 12x36 Irregular Bond masonry with a quarter part with different AR.

(a) (b) (c)
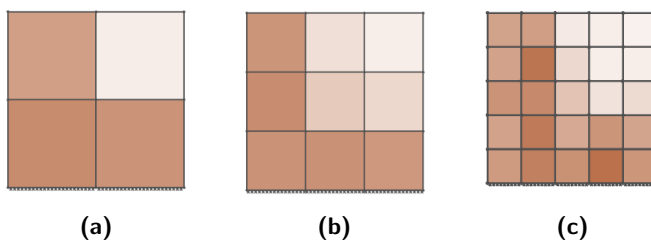
Figure 5.29: Non-uniform distribution of the Aspect Ratio: Increasing number of elements to catch geometrical imbalances in the AR distribution: (a) 2x2 regions; (b) 3x3 regions; (c) 5x5 regions
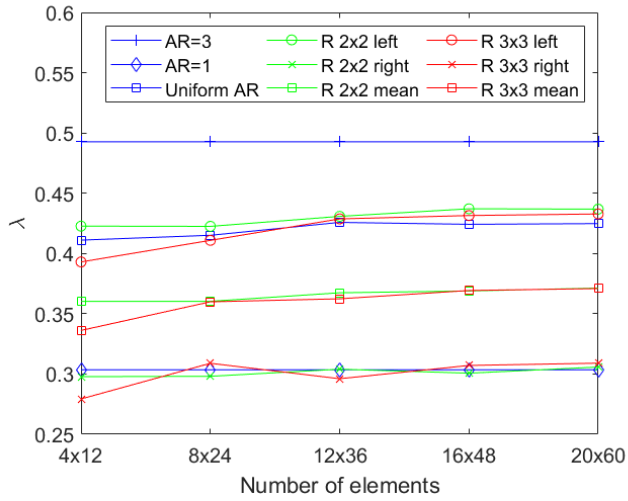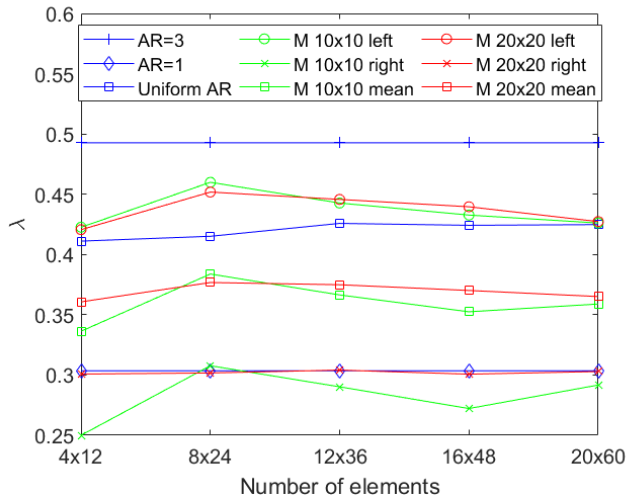
Figure 5.30: Non-uniform distribution of the Aspect Ratio: IB texture masonry, outcome for both directions: (a) sub-regions method; (b) method that maps the AR
R = sub-regions method
M = method that maps the AR

the problem, the mean value of each method is meaningless and that is clear from the graphs. For the left oriented seismic action, since the left part of the masonry has a mean $AR = 3$ as most of the masonry, the outcome for both methods is close to the Uniform AR method. For the right oriented seismic action instead, the outcome is close to the failure multiplier of the panel if we assume that the AR is the one of the quarter masonry on the top right since the mechanism involves that part. As said before, in this case the sub-regions method seems to be more accurate but it's because of the simplicity of this example. The method that maps the AR instead seems to be more unstable but that is because it can also catch local mechanisms that require less energy to activate.

Example of application for a true chaotic texture

In this section a simple application of a very chaotic texture is addressed. The actual texture is shown in Fig. 5.31 and it has been simplified by using segments representing the mortar joints in the rigid block model. The rigid block analysis

Figure 5.31: Example of a chaotic texture

outcome is shown in Fig. 5.32 Currently the homogenized models are not applied in this case since a simple modification of the local Aspect ratio throughout the wall cannot catch all the aspects that such kind of textures has and moreover the Aspect Ratio concept applied to shape that are far from being rectangular is not very accurate.

5.4.Application to walls with openings
Ferris Tin-Loi wall

Three different change in the geometry with respect to the periodic one are considered and an example is shown for the Ferris Tin-Loi case (Ferris and Tin-Loi (2001)) (see Fig. 5.33(a)) in which each block had dimensions 4 x 1.75 units, the coefficient of friction is 0.75 and cohesion is 0 .

(a) **(b)**
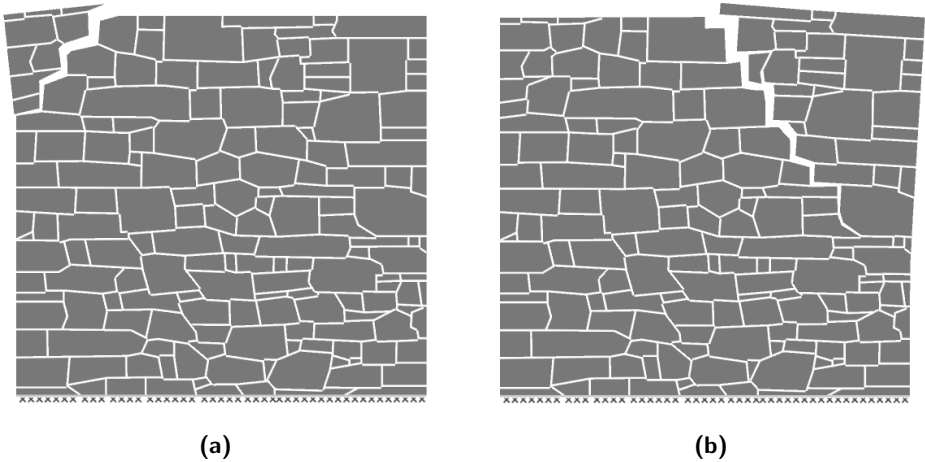
Figure 5.32: Rigid block outcome for the chaotic texture
(a) left oriented seismic action, Failure multiplier = 0.527; (b) right oriented seismic action, Failure multiplier = 0.470.

Irregular bond textures with the same mean aspect ratio
A simple way to achieve it is by shifting the vertical mortar joints in each row leaving the number of elements per row unmodified.
An example of irregular bond is generated randomly shifting the vertical mortar joints Fig. 5.33(b). Red dashed lines indicate an alignment of vertical mortar joints.
The failure multiplier will be lower when mortar joints are aligned, especially if they are aligned in a way that they form a narrow ladder oriented in the same direction as the seismic action as shown in Fig. 5.34(b).

SSB-DSB textures with course dependent aspect ratio
Samples are easily generated by shifting the horizontal mortar joints leaving the vertical mortar joints unchanged as in Fig. 5.33(c).
In this case the aspect ratio of each course will be different from the others.
The expectation is to obtain results close to the original periodic texture, sometimes with an higher failure multiplier as in Fig. 5.34(c) and sometimes with a lower one.

A combination of previous textures
In the end a combination of the first two approaches is tested Fig. 5.33(d).
A texture so generated should show higher differences with respect to the periodic one as shown in Fig. 5.34(d).
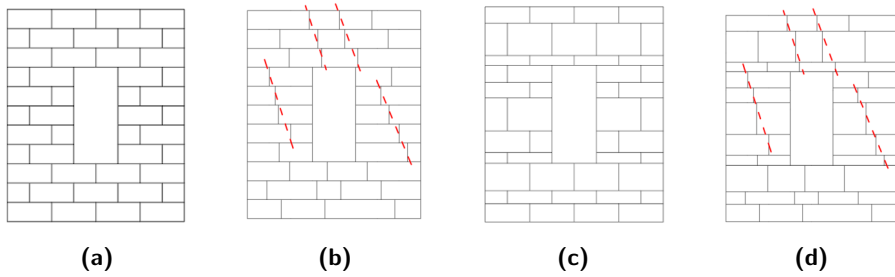
Figure 5.33: Wall with openings, Ferris Tin-Loi wall : (a) Ferris Tin-Loi original texture (b) Irregular bond texture; (c) SSB/DSB texture; (d) Combination of the previous textures
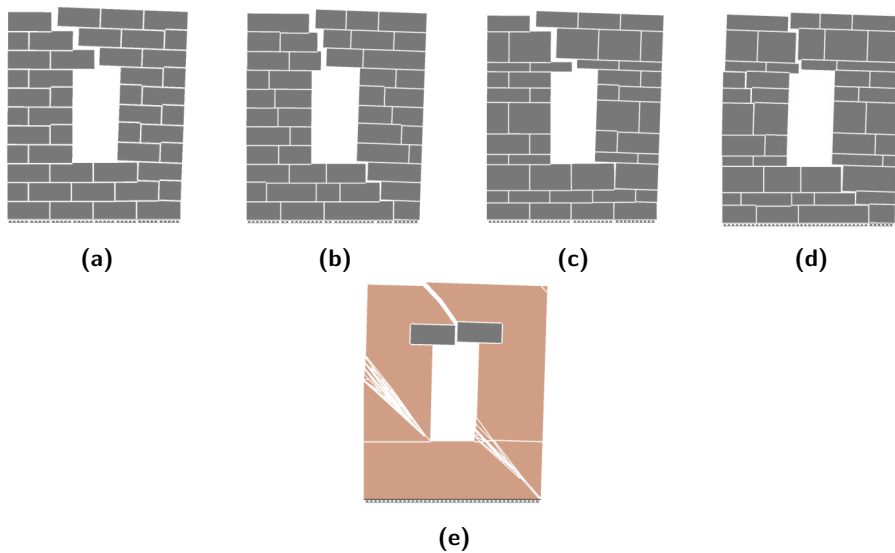
Figure 5.34: Wall with openings, Ferris Tin-Loi wall : results obtained from textures in Fig. 5.33, (a) Failure multiplier = 0.4037; (b) Failure multiplier = 0.3722; (c) Failure multiplier = 0.3741; (d) Failure multiplier = 0.4069; (e) Homogenized solution, Failure multiplier = 0.2872

Facade with openings

As a real case application, the masonry facade with openings analysed in Valentino et al. (2023) is chosen, and the above mentioned changes to the texture are applied. In the periodic case each block has dimensions 0.6 x 0.3 m and so the aspect ratio is 2. The facade is 9.0 x 10.8 m and it has six openings all with dimensions 1.2 x 2.1 m.

In this analysis the coefficient of friction assumed is 0.65 and the cohesion is 0. For the Irregular Bond texture (IB), the joints are shifted in order to make the block overlap for a tenth of their width. For the Different Stretcher Bond textures (DSB) the height of two adjacent courses are modified by increasing or decreasing the value by 40 %. Two different DSB texture are generated, by inverting the course reduced in height with the course increased in height. These two textures are called DSB1 and DSB2. The combination texture has been generated as explained in the previous section.

Seismic action

Here the effect of a seismic action is considered. The outcome for the periodic texture is shown in Fig. 5.35(a) for the rigid block model and in Fig. 5.35(b) for the homogenized model. For the DSB textures, only the right mechanism is shown since the texture it's symmetric, for the IB and the combinations textures both seismic orientation are shown (Fig. 5.35(c, d)). It is possible to notice from Fig. 5.35(e, f) that also in this case, the Irregular Bond has the weakest structural behaviour while the DSB textures have a similar failure multiplier. The combinations textures inherit the weak behaviour from the IB and in fact the Failure multiplier is close to that value and lower than the periodic and the DSB as shown in Fig. 5.35(g, h).

Rigid settlement

Here the effect of a rigid settlement is considered. The outcome for the periodic texture is shown in Fig. 5.36(a) for the rigid block model and in Fig. 5.36(b) for the homogenized model. For the same reasons of the seismic case, the DSB textures outcome is presented just for one orientation. in the DSB1 texture there is a significant decrease of the failure multiplier, that is not reflected in DSB2, showing that changing the order of the rows may lead to a certain variation, this is shown in Fig. 5.36(c, d). The IB has again the weakest behaviour and it may be noticed that in this case also the failure mechanism is orientation dependent, in Fig. 5.36(e) for example, a crack occurs in the outer part of the upper opening while in Fig. 5.36(f) it occur in the inner part. The combination textures outcome, as in the previous application, are quite similar to the IB outcome, both in terms of failure multiplier and failure mechanism, as shown in Fig. 5.36 (g, h).
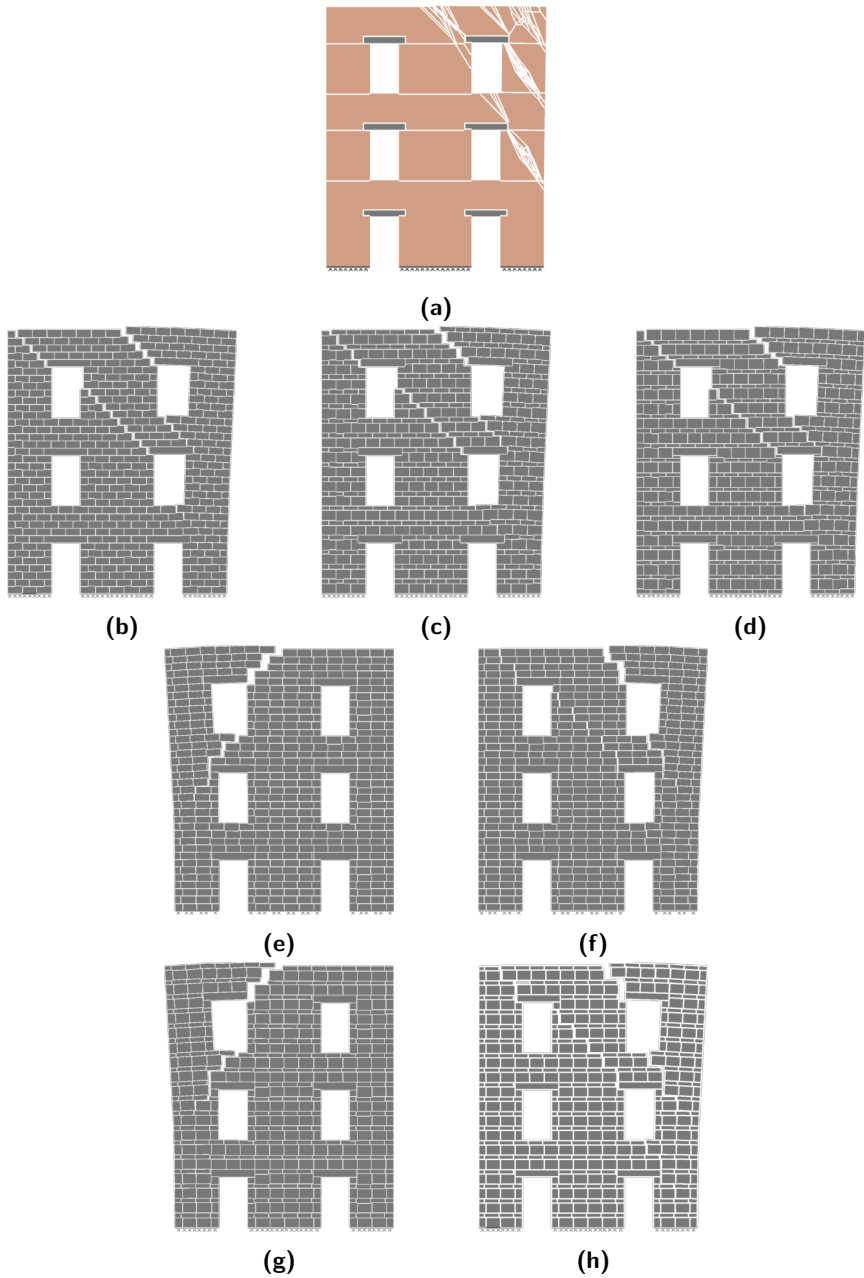
Figure 5.35: Facade with openings: results for the different textures for a seismic action, (a) Periodic texture, Failure multiplier = 0.2845; (b) Homogenized solution, Failure multiplier = 0.2394 (c) DSB1, Failure multiplier = 0.2851; (d) DSB2, Failure multiplier = 0.2839; (e) IB (left orientation), Failure multiplier = 0.2593 ; (f) IB (right orientation), Failure multiplier = 0.2603 ; (g) Combination (left orientation), Failure multiplier = 0.2601 ; (h) Combination (right orientation), Failure multiplier = 0.2611
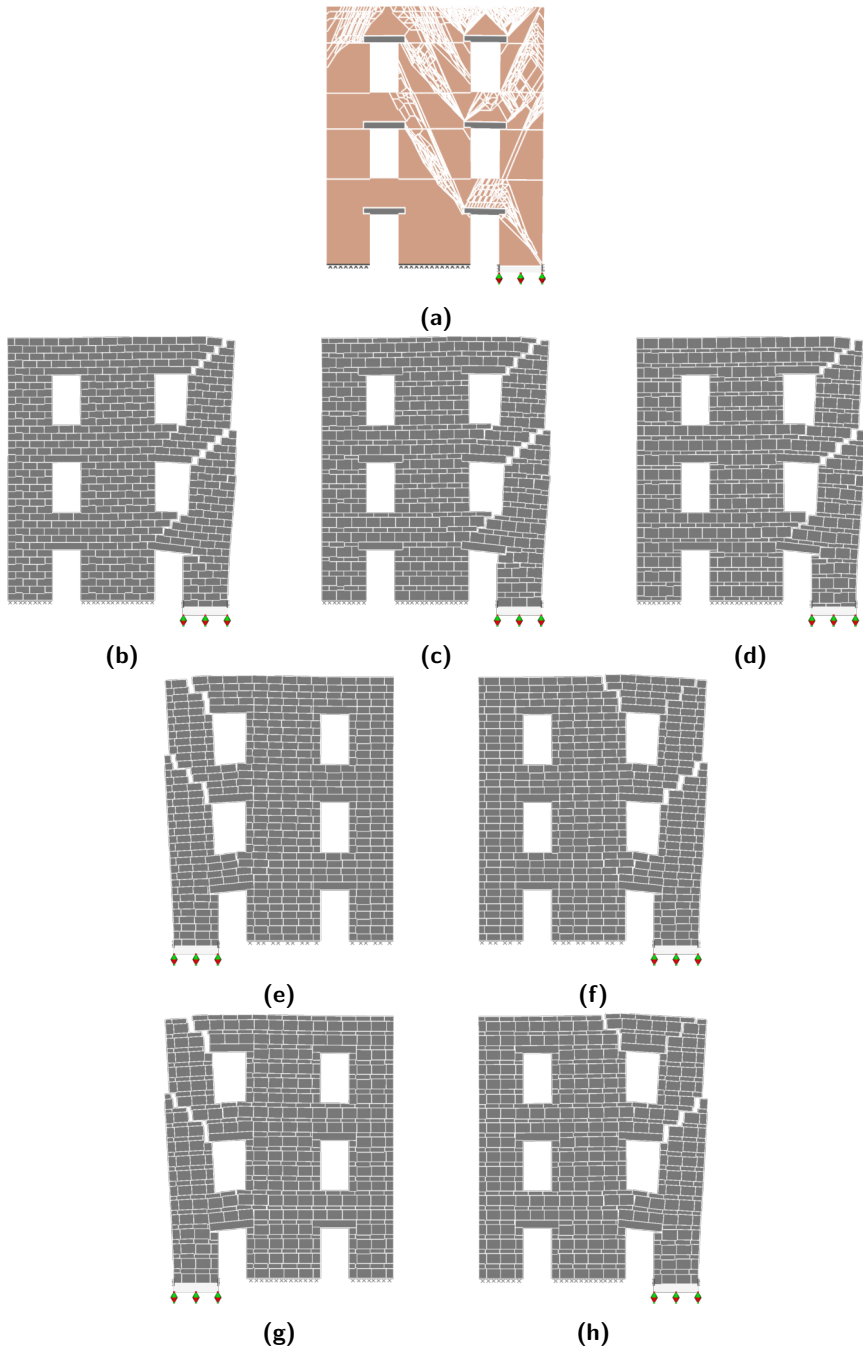
Figure 5.36: Facade with openings: results for the different textures for a rigid settlement, (a) Periodic texture, Failure multiplier = 0.5918; (b) Homogenized solution, Failure multiplier = 0.4549; (c) DSB1, Failure multiplier = 0.6354; (d) DSB2, Failure multiplier = 0.5928; (e) IB (left orientation), Failure multiplier = 0.5228; (f) IB (right orientation), Failure multiplier = 0.5541 ; (g) Combination (left orientation), Failure multiplier = 0.5232 ; (h) Combination (right orientation), Failure multiplier = 0.5470

5.5. Discussion

Discontinuity Layout Optimization has been applied to different textures in order to outline their influence. The rigid block analysis is capable of considering the effective texture and also the size of the elements and so it is the more representative method to describe the behaviour of such irregular masonry. Anyway the results obtained overestimates the failure multiplier and for an high number of elements it may be cumbersome.

Homogenized method instead are independent on the size of the elements and the result is more accurate when the stones are effectively a micro-structure for the wall (i.e. when the size of the wall is way bigger than the stones). Moreover they also provide a safe lower bound and so when the wall has an high number of elements they can be useful and give a rapid answers by simply knowing the mean Aspect Ratio of the wall or the Aspect ratio of portion of the wall depending on the method.

If a masonry panel has a small number of elements (up to 8×24 elements), the sub-regions method better detects the irregular distribution. However for all of the homogenization approaches, the failure multiplier is significantly lower than the rigid block model except when the failure mechanism involves one element, in this case the outcome is not representative of the structural behaviour of the panel.

A Masonry that has a localized distribution of the Aspect Ratio can be addressed by more advanced methods such the method that maps the Aspect Ratio. However these methods only have degree of value at certain representative lengths. If the mapping is taken to the level of individual masonry units then it appears there is little advantage over explicitly modelling these units using a rigid block approach.

If the masonry shows a localized distribution of the Aspect Ratio, and this may happen for the historical masonry, the dependence on the direction is too high and the Uniform Aspect Ratio will fail to provide a correct solution. Moreover, for the sub-regions method it is necessary to know in advance the optimal number of regions to catch this localization.

The Method that maps the Aspect Ratio instead automatically detects the position of the elements and it is useful for overcome this issue.

In the subsection 5.4 there is only an homogenized model for all the texture. This is mainly due to the fact that the irregular textures were built manually following simple rules that leads to an unaltered mean Aspect Ratio. For this particular cases it seems that only the method that maps the Aspect Ratio would individuate difference between textures but this aspect will not be addressed in this work. In existing and in random generated masonry instead, difference between the textures are detected also by simple regions homogenized methods as in Fig. 5.26.

Advantage of DLO is that can directly mix homogenised and discrete modelling if there are distinct masonry patterns to be captured.

A possible future extension of the adaptive solution also for the homogenized masonry will further reduce the time of analysis.

6. FEM comparison

In this chapter a comparison between DLO rigid blocks limit analysis and a FE analysis is carried out. For the comparison two textures have been chosen, a Periodic texture and an Irregular Bond texture both having about the same number of elements (8x24). Square panels are chosen (as in 5.3) and the local Aspect Ratio (AR) is 3 (exact for the periodic texture and mean for the IB texture). In the end also a chaotic like texture is tested in order to show that also for more complicated textures the method provides valuable results.

6.1.FE model characteristics

The FE model has been developed in Abaqus (Smith (2009)) since it allows to model contact surfaces in a simple yet effective way. Moreover it is a well known software for FE analysis and so its reliability has been demonstrated by several authors. In this section the main characteristics are discussed. The model is assembled combining stone elements modelled with an elastic isotropic material and frictional contact interfaces. The elastic material has Young module $E = 5800 MPa$ and a Poisson ratio $\nu = 0.2$. The density is assumed as unitary since it does not influence the analysis in case of pure frictional behaviour of joints.

This block elements are then assembled using frictional interfaces having coefficient of friction $\tan \phi = 0.75$. For the tangential behaviour of the contacts the friction formulation is set as "Penalty" and the no limit on shear stress is imposed. For the normal behaviour a "hard contact" type is chosen and so interpenetration of the blocks is not allowed. The lower part of the panel is fixed linking the displacement to a master node.

For the analysis, a single step of 1 second is defined even if it is symbolic since the load is applied with a quasi-static approach and so dynamic effects

are not considered. The gravity load is applied instantly whereas the horizontal body force is applied linearly in the time interval from a null value to the value of 1g.

For the mesh a 4-node bi-linear plane stress quadrilateral, with reduced integration and hourglass control element is adopted (CPS4R). The mesh size is about 12 mm and in any case not less then a tenth of the size of the element.

6.2. Comparison results

The periodic texture and the Irregular Bond texture randomly generated are shown respectively in Fig. 6.1(a) and Fig. 6.1(b). The solution obtained for

(a)   (b)
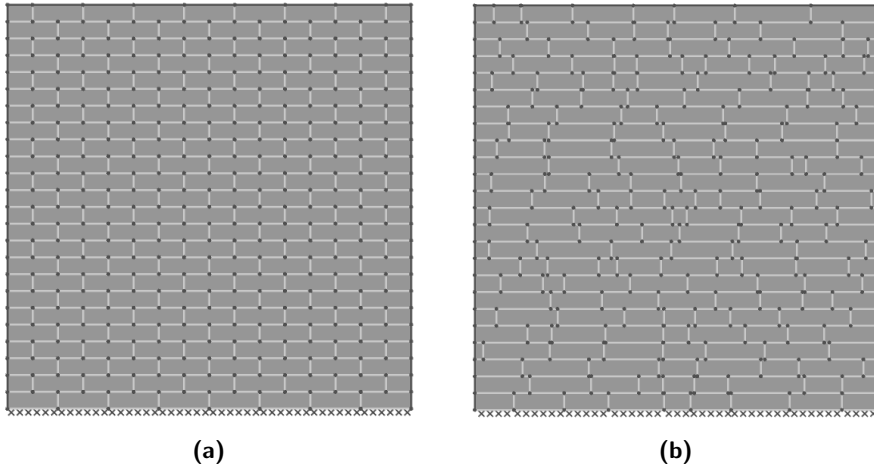
Figure 6.1: Texture of the samples used for the comparison with the FE models; (a) 8x24 elements periodic texture, (a) 8x24 elements Irregular Bond texture

the periodic texture by means of DLO is shown in Fig. 6.2(a) and the failure multiplier is 0.6143. The solution obtained for the same texture by means of the Finite Element analysis is shown in Fig. 6.2(b). To evaluate the value of the horizontal acceleration that causes failure the following reasoning has been adopted.

The shear and normal reaction forces of the wall at its basis are evaluated in time (named as $RF1$ and $RF2$ respectively). While the normal reaction is constant in time since gravity is applied instantly and moreover it is slight influenced by the failure mechanism, the shear reaction increases linearly with time until the first crack occurs and it becomes constant where the wall reaches its failure.

So, since the horizontal acceleration is applied in a step of 1 second and it goes from 0 to 1g, the time step also indicated the horizontal acceleration in terms of g and since the vertical acceleration is constant and applied instantly it also coincides with the load factor λ.

The trend of the shear reaction force ($RF1$) vs the load factor (λ) for the

Figure 6.2: Comparison between models for the periodic texture; (a) DLO method, failure multiplier = 0.614 (b) FE method, crack opening load factor = 0.608

periodic texture is shown in Fig. 6.3. The blue dots represents $RF1$ values eval-
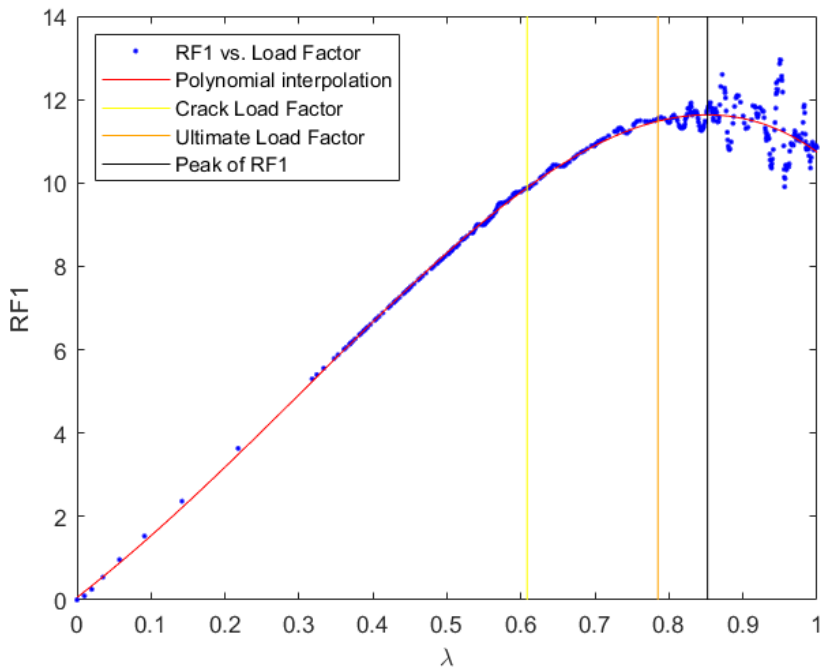
Figure 6.3: Shear reaction force $RF1$ VS load factor λ for the periodic texture

uated for each step time and they are closer in the left part of the diagram since Abaqus reduced gradually the time step in order to have a better convergence

and accuracy.

These points are then fitted with a polynomial curve of degree 4 with a coefficient of determination $R^2 = 0.97$ (red curve). The derivative of this fitted curve is evaluated, and the slope of the first part is obtained.

Since the loss of shear reaction force is gradual, a method to identify the load factor associated to the first crack is necessary. For this purpose, the slope of the first part of the diagram is evaluated (i.e. the maximum slope) and the first crack is associated to a loss of 25% of the maximum slope and it's individuated in Fig. 6.3 by a vertical yellow line.

To evaluate the ultimate load factor first the hypothesis of the factor associated to the highest value of $RF1$ was adopted (individuated by the black vertical line) but if the unfitted plot is observed it is clear that at that point the solution is already unstable and out of the physical meaning. For this reason as ultimate load factor is considered the point where the graphs starts becoming unstable and this value is individuated by the vertical orange line. The value for this ultimate load factor for the periodic texture is 0.785.

Anyway, since the limit analysis individuates the beginning of the failure mechanism and not its evolution, the failure multiplier of obtained by DLO must be compared to the load factor associated to the opening of the cracks that in the FE analysis is 0.608 that is a good agreement since in the DLO solution is was 0.614.

So the failure mechanism for the FE analysis shown in Fig. 6.2 (b) is obtained for a load factor $= 0.608$ and it is displayed with the aid of a gradient showing the absolute displacements and vectors showing their direction. The line between the displacements indicated by the yellow color and those indicated by the green color matches the main crack of the DLO mechanism (Fig. 6.2 (a)) quite well.

The comparison for the failure mechanism at the opening of the crack and at the ultimate load factor is shown in Fig. 6.4. For the Irregular Bond texture the same procedure has been carried on. The solution obtained for the Irregular Bond texture by means of DLO is shown in Fig. 6.2(a) and the failure multiplier is 0.583. The solution obtained for the same texture by means of the Finite Element analysis is shown in Fig. 6.5(b).

The trend of the shear reaction force ($RF1$) vs the load factor (λ) for the Irregular Bond texture is shown in Fig. 6.6. This time the polynomial interpolation of the same order has a coefficient of determination $R^2 = 0.68$ due to the high scattering of the last part where the FE analysis diverges. Anyway it has been tested that if those values are eliminated and the rest of the plot if fitted the results are similar and so the full analysis is shown here for the sake of completeness.

In this case the crack load factor evaluated is 0.551 and it's lower than the periodic texture crack factor as it happens for the DLO analysis.

Also the ultimate load factor (0.675) is lower than the periodic one (0.785) and this confirms that the Irregular bond texture has a lower seismic capacity

Figure 6.4: Comparison between FEM failure mechanism for the periodic texture for two different load factors; (a) crack opening load factor $= 0.608$, (b) ultimate load factor $= 0.785$
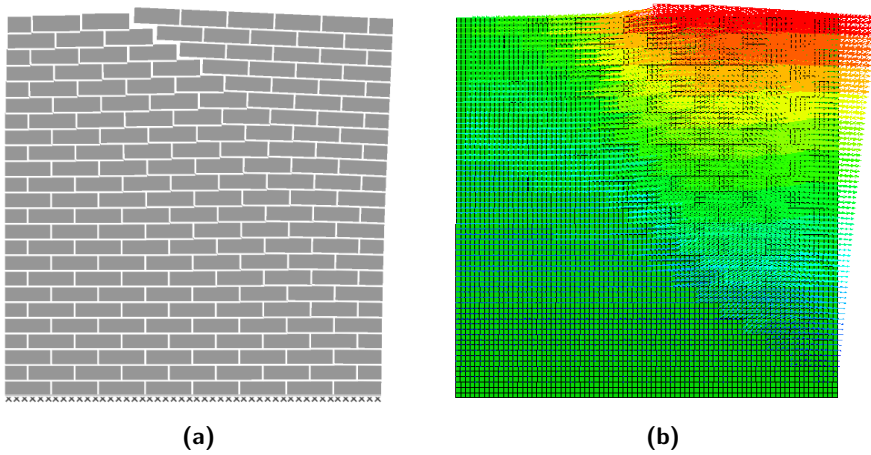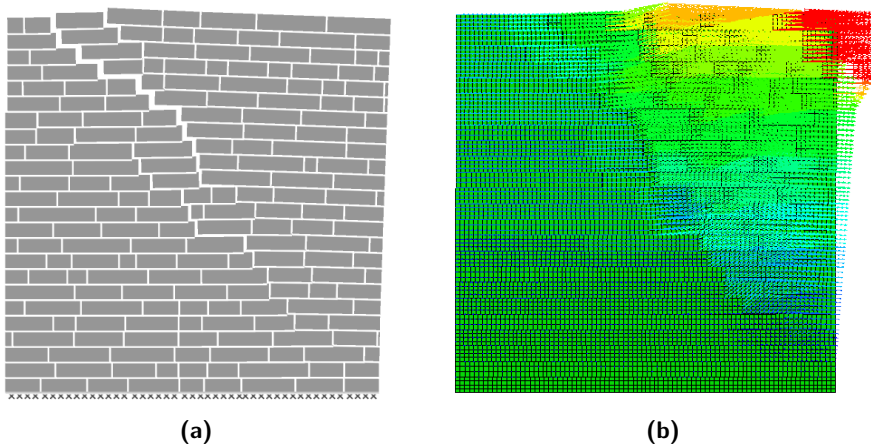

Figure 6.5: Comparison between models for the Irregular Bond texture; (a) DLO method, failure multiplier $= 0.583$ (b) FE method, crack opening load factor $= 0.551$
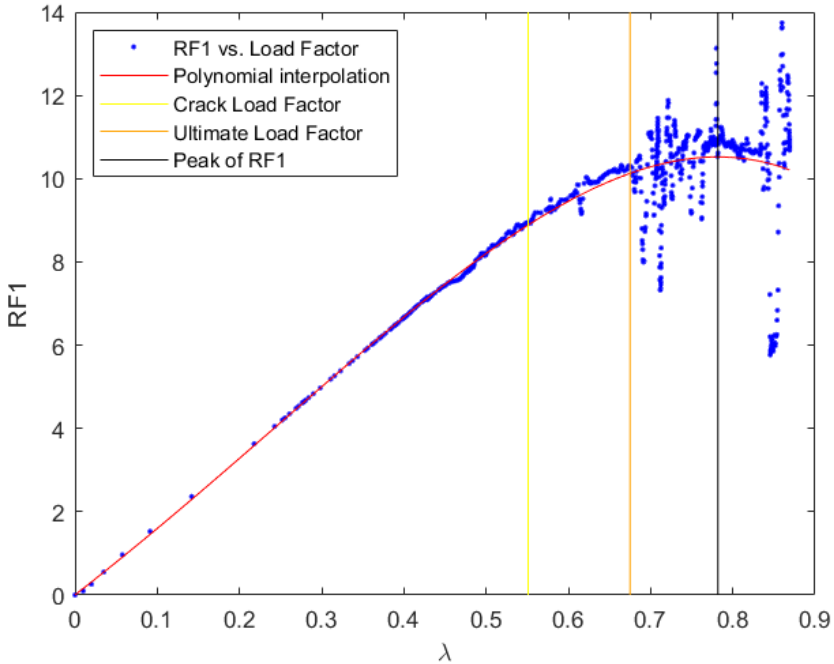
Figure 6.6: Shear reaction force $RF1$ VS load factor λ for the Irregular Bond texture

and it's more subjected to instability,

If the failure mechanisms are compared there is a clear agreement between the DLO analysis and the FE analysis. The only difference is found in a local failure mechanism that involves the upper right part of the FE model. Anyway it is reasonable to state that the detachment of that part would not influence a lot the shear reaction force at the basis of the wall.

The comparison for the failure mechanism at the opening of the crack and at the ultimate load factor is shown in Fig. 6.7.

6.2.1.Case of chaotic masonry

Also the case of a simple chaotic texture realised with equivalent rectangular shaped elements as in Fig. 5.1(c) is analysed. The chosen texture is shown in Fig. 6.8.

The $RF1$ vs λ plot in this case is very irregular over a certain value of λ as it it possible to see in Fig. 6.9 and for this reason a polynomial curve couldn't approximate the first branch of plot very well. For this reason values over a certain λ have been excluded for the analysis since they didn't have a physical meaning and so in Fig. 6.10 a plot similar to the previous cases is obtained.

In this case the polynomial interpolation of the same order has a coefficient of determination $R^2 = 0.92$.

(a)   (b)
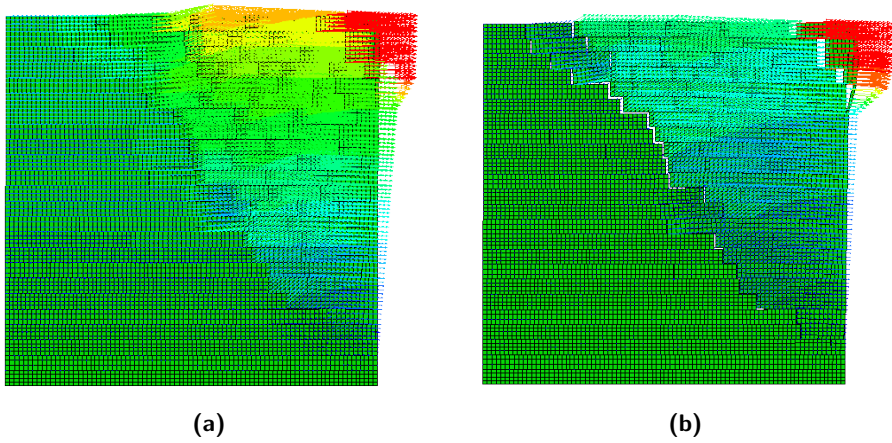
Figure 6.7: Comparison between FEM failure mechanism for the Irregular Bond texture for two different load factors; (a) crack opening load factor = 0.551 , (b) ultimate load factor = 0.675
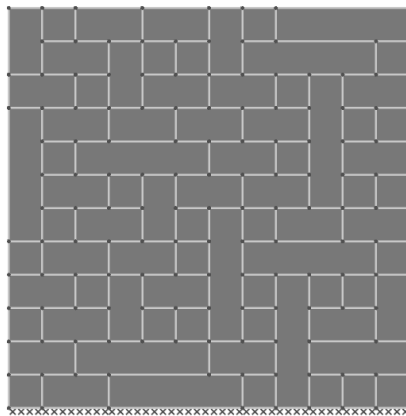
Figure 6.8: Texture of the chaotic sample used for the comparison with FE methods.
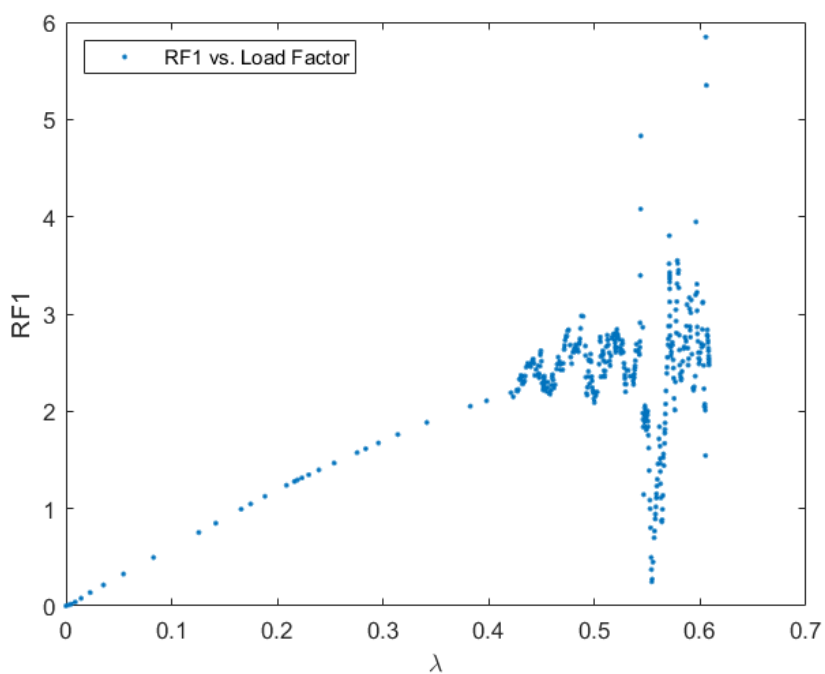
Figure 6.9: Shear reaction force $RF1$ VS load factor λ for the Irregular Bond texture - full plot.
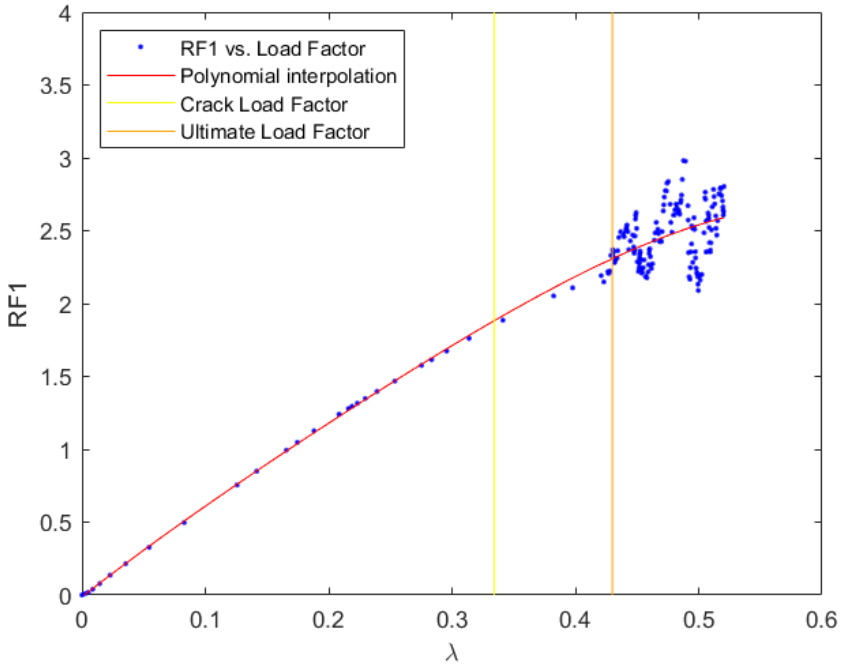
Figure 6.10: Shear reaction force $RF1$ VS load factor λ for the Irregular Bond texture.

The solution obtained for the Chaotic texture by means of DLO is shown in Fig. 6.11(a) and the failure multiplier is 0.407.

(a)   (b)
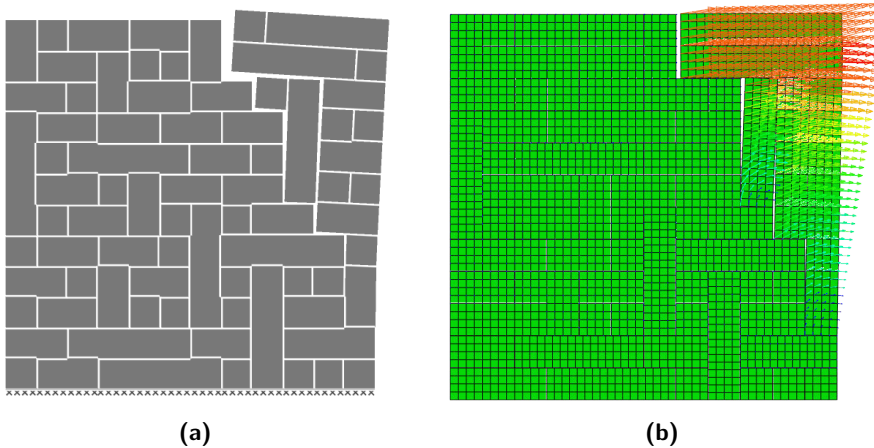
Figure 6.11: Comparison between models for the Chaotic texture; (a) DLO method, failure multiplier = 0.407 (b) FE method, crack opening load factor = 0.334

The solution obtained for the same texture by means of the Finite Element

analysis is shown in Fig. 6.11(b).

In this case the crack load factor evaluated is 0.334 and it's again lower than the one evaluated by the DLO limit analysis.

Moreover, the ultimate load factor (0.430) is lower than both the periodic and the Irregular Texture ultimate load factors.

The comparison for the failure mechanism at the opening of the crack and at the ultimate load factor for the chaotic texture is shown in Fig. 6.12.
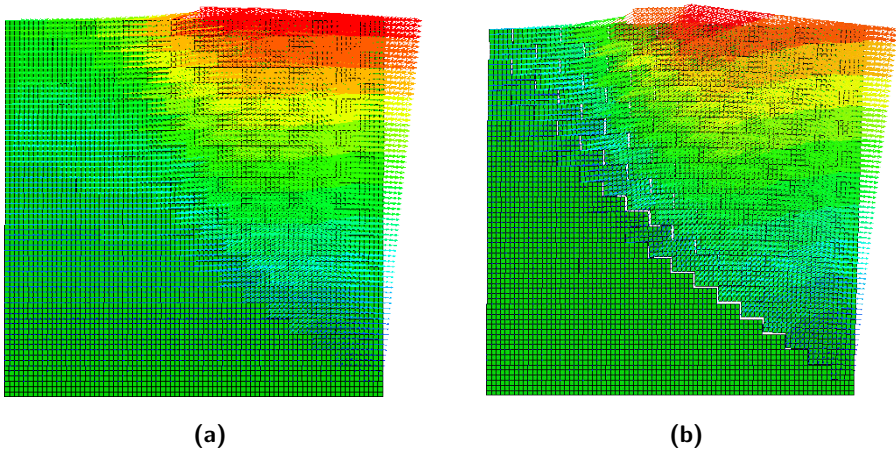

(a)   (b)
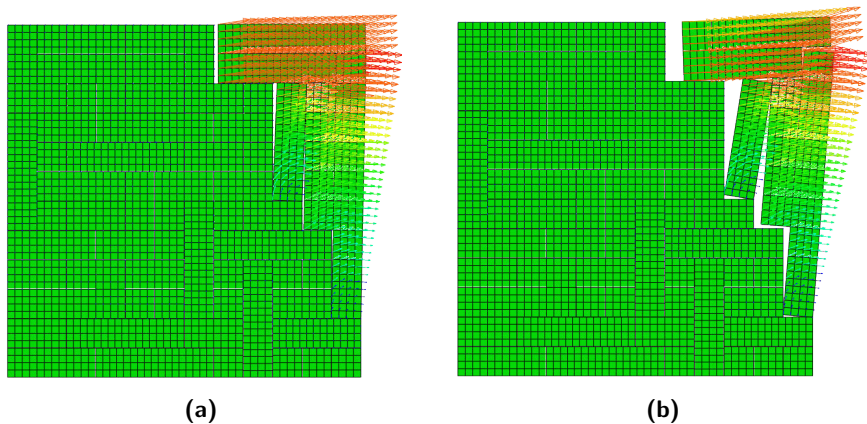
Figure 6.12: Comparison between FEM failure mechanism for the chaotic texture for two different load factors; (a) crack opening load factor = 0.334 , (b) ultimate load factor = 0.430

6.3. Computational effort

Once the agreement between the outcome for the two different methods is established, also the time needed for the analysis must be compared. In order to make the comparison, all the models are run on an Intel I7-8565U CPU (1.80 - 1.99 GHz) computer with 16 GB of RAM and running 64-bit Windows 10 was used.

The elapsed time is resumed in Table 6.1 that shows the DLO rigid block analysis is way faster than the FE analysis. Although many aspects of the FE analysis may be modified in order to reduce the computational effort, such the refinement of the discretisation, the use of rigid blocks instead of an elastic material and other solver options, it is clear that both the time of analysis and the memory requested are not comparable.

This is the reason why this method was chosen from the beginning for this parametric analysis. The sample tested for the comparison have around 200 blocks and they still takes hours to converge to the final solution.

Some of the samples analysed in Sec. 5.3.2 exceed 1200 blocks and dozens of them are generated, so a FE incremental analysis would take too much time with no benefit in the evaluation of the load factor.

Table 6.1: Elapsed time for both model and for three different textures

Texture	Method	CPU time		
		(hr)	(min)	(sec)
Periodic	DLO	-	-	2
	FEM	-	51	54
Quasi-periodic (IB)	DLO	-	-	2
	FEM	2	14	47
Chaotic	DLO	-	-	1
	FEM	-	15	43

6.4. Discussion

In this chapter two different methods for the analysis of the in plane behaviour of masonry under a seismic action have been addressed. The two methods have a completely different approach.

In the DLO method limit analysis is applied by means of a Linear Programming problem that allows to individuate the right failure mechanism amongst an huge number of potential mechanisms. The solution is then achieved in a single step though inside the Linear Programming a lot of equations and inequality are solved through iterations by means of an efficient solver. For this reason a single set of relative displacement is defined and it's associated to a single load factor. The evolution of the crack pattern cannot be evaluated.

In the FE analysis instead, the solution is achieved by steps by means of a non-linear analysis. The load is applied as a quasi-static horizontal body force and it increases at each step of the analysis, so the displacement field can be evaluated at each step as well as stress in each point of the domain. Moreover the blocks are modelled with a linear elastic isotropic material and this allows to have strain also within these elements.

In conclusion FEM is a powerful tool that allows to carry on a wide range of possible analysis and to evaluated an high number of parameters. DLO instead only evaluates the relative displacements and the plastic multipliers for the mechanisms that requires the less energy of activation. Therefore is the aim of the analysis is just the evaluation of the failure load and the failure mechanism, DLO rigid block analysis provides a fast and powerful tool. Especially in the case of historical masonry buildings under seismic condition it is a good choice since the failure is likely to occur in the mortar joints and not within the elements. For this reason a FE analysis may result cumbersome just to provide information that is not strictly necessary.

The same reasoning may be adopted for Discrete Element Methods that are not investigated in this work. Unlike DEM approaches, DLO only evaluates

relative displacements and so the number of unknowns is further reduced but it can't be applied to analysis whose aim is to evaluate the temporal evolution of the mechanism and to deal with large deformations.

7. Conclusions

Here the main conclusion of this work are drawn.

In this work Discontinuity Layout Optimisation (DLO) numerical analysis is employed to carry out a parametric analysis which involves both geometrical and mechanical factors in order to characterise the effect of non-periodic masonry textures. For the current masonry classification the parameters studied are the height of the panel, the slenderness of the stones (i.e. the local aspect ratio) and the mechanical characteristics of the mortar.

A new classification of non-periodic textures has been proposed and the variation of the failure loads for this different textures has been evaluated generating random samples.

Moreover the analysis has been conducted both with a discrete approach and an homogenised approach and the advantages and limitations have of these methods have been discussed.

These methods have been also applied to a whole facade with openings to show the reliability and the accuracy.

In the end a comparison with a FE non-linear analysis has been addressed, showing the huge reduction in the computational effort for the study of the failure loads using DLO instead of FE.

The conclusion are shown in the following bullet point list, divided in sections for the sake of clarity.

7.1. Effect of Variation of the height of the panel for the current classification

- For the current classification, the effect of the variation of the global Aspect Ratio (H/W) has been considered. All but the periodic texture show an irregular variation with the height of the panel along with an asymmetry of the failure multiplier and the failure mechanism. In particular, for a certain range of the global Aspect Ratio, the quasi-periodic texture has a local mechanism while the quasi chaotic texture has always this feature. The periodic texture instead always behave globally. In terms of failure multipliers, the periodic texture shows the higher values (i.e. a better structural capacity), the quasi-periodic texture has intermediate values and the chaotic has the worst behaviour.

- The presence of a vertical load above the wall along with its associated seismic mass causes a decrease of the failure multipliers cause it makes rotations occur for lower values of the failure multiplier.

7.2. Study of the variation of geometrical and mechanical parameters for a periodic texture

- The presence of cohesion in vertical mortar joints has been analysed and its effect has been checked with analytical formulas.

- The effect of the variation of the local Aspect Ratio has been studied and the failure multipliers decreases when w/h decreases (i.e. for slender elements).

- The possibility for the failure to occur within the blocks has been considered, and it has been shown that both cohesion and friction of blocks influence the outcome. Anyway for historical masonry mortar is very weak compared to blocks and so the failure occurs along mortar joints.

7.3. New classification for quasi-periodic textures and evaluation of their influence by means of DLO

- A new classification procedure for non-periodic masonry textures has been proposed with three main classes: periodic, quasi-periodic and random. The quasi-periodic classification is further subdivided into Similar height Stretcher Bond (SSB), Different height Stretcher Bond (DSB), and Irregular Bond (IB). The classification is determined systematically using 2 parameters: the index, p, of the staggering of vertical mortar joints and the coefficient of variation v of the height of the courses.

- A method of modelling a range of textures and masonry panel sizes using the Discontinuity Layout Optimization (DLO) method has been demonstrated. This essentially achieves a 'rigid block' analysis with associative friction. Each analysis utilised seismic loading to the left and right to quantify stability.

- For each texture the masonry unit layout was varied randomly. The variability in results was shown to reduce when the number of masonry units in the panel increases and it is greatest for the Irregular Bond. For example the Irregular Bond has a variation of about 10% with respect to the periodic texture for a 4×12 sample, while for a 20×60 sample the variation is about 1%. It is difficult to make quantitative statements since if a critical alignment of bonds in irregular masonry manifest near a corner of the panel then a low strength will result. For this reason, if the aim is to investigate also the local mechanisms, it is required to model all masonry explicitly by means of a rigid block analysis. This could be done through image analysis in order to produce a quick and detailed model. Although the step between image and model is not always straightforward, the current interest on machine learning techniques merged with image digital processing techniques may lead to efficient solutions.

- In addition to the rigid block analysis, the use of an homogenized approach using DLO was also investigated. In this case the masonry panel is represented by a single representative aspect ratio that may be determined from image/statistical analysis of the masonry panel or other classification techniques. If a non-periodic masonry panel has a great number of elements (20×60 in this case), a single uniform aspect ratio was demonstrated to provide answers below and to within 10% of the rigid block analysis.

- Four sub-variants of the homogenisation approach were considered to account for variation of geometry within a given panel: use of a single region (uniform local aspect ratio), subdivision of the region into horizontal layers, subdivision of the region into other sub-regions and continuum mapping of the local aspect ratio across the region with each discontinuity adopting an average local aspect ratio along its length. However not every wall panel characterisation has the same computational complexity and the trade off between these two aspects is not worthwhile for each of them. Anyway if the panel has been geometrically characterised thoroughly it seems more straightforward to

simply model every block explicitly. This is true until the number of blocks is very high since it can increase the computational effort of a rigid block model considerably and since also the effect of the texture is less relevant in this case a simple homogenised model obtain by characterising portions of the wall statistically is suggested.

- It is hypothesised that if major heterogeneities are individuated (e.g. two different walls joined by a continuous joint line) they can be properly modelled via the homogenization approach that can provide a convenient 'low cost' first analysis option.

7.4. FEM comparison

- FE models in Abaqus have been created to make a comparison with the DLO rigid block approach. The comparison shows a good agreement both for the failure multipliers and for the failure mechanisms. Although the FE analysis can provide more information, it requires a great computational effort and so DLO is proved to be a quick and reliable tool for the assessment of the structural capacities of masonry panels under seismic loads. The difference in time between the a FE approach and the DLO analysis is dependent on the number of elements and on the texture but even for the simplest case analysed the FE elapsed time was a thousand times bigger than the DLO elapsed time. This was the main reason to use such method for the systematic evaluation of the impact of the textures and other geometrical and mechanical aspects.

7.5. Future work

As a future perspective, the realisation of real samples with different texture to be tested in laboratory is in plan. Moreover an extension of the current analysis with an extension to the failure within the blocks (as already partially investigated in Sec. 5.2.3) is expected. For the moment the homogenised model is based on rigid block failure modes so it cannot reproduce the compression failure of the elements. An extension to investigate also this failure modes could be useful in order to provide quick and reliable solutions for many other problems.

A. Python DLO script

In this section a new script in Python for the analysis of plane plasticity problem is presented. The basic script is then enhanced in order to allow treatment of cohesive-frictional materials, with self-weight treated herein in a new and conceptually elegant way. Moreover various examples are presented to illustrate the capabilities of the script and the displacements are represented with vectors to provide a better insight of the failure mechanism.

This work has been already developed in a paper currently in revision.

A.1. Basic formulation

In this section a formulation for a simple cohesive media is presented. However unlike the formulation used in the analogy with the optimal layout of trusses (Eqn. (2.104)) in this case a more general formulation is adopted, which also allows the potential for dilational displacements to occur along slip-line discontinuities (see Fig. A.1):

$$\min_{\mathbf{d},\mathbf{p}} \quad \lambda \mathbf{f}_{\mathrm{L}}^{\mathrm{T}}\mathbf{d} = \mathbf{g}^{\mathrm{T}}\mathbf{p} \tag{A.1a}$$

$$\text{s.t.} \quad \mathbf{Bd} = \mathbf{0} \tag{A.1b}$$

$$\mathbf{Np} - \mathbf{d} = \mathbf{0} \tag{A.1c}$$

$$\mathbf{f}_{\mathrm{L}}^{\mathrm{T}}\mathbf{d} = 1 \tag{A.1d}$$

$$\mathbf{p} \geq \mathbf{0}, \tag{A.1e}$$

where $\mathbf{f}_{\mathrm{L}} = \{S_{\mathrm{L}1}, N_{\mathrm{L}1}, S_{\mathrm{L}2}, N_{\mathrm{L}2}..N_{\mathrm{L}m}\}$ is a vector of live loads acting on the discontinuities, $\mathbf{d}^{\mathrm{T}} = \{s_1, n_1, s_2, n_2...n_m\}$ are the relative shear and normal
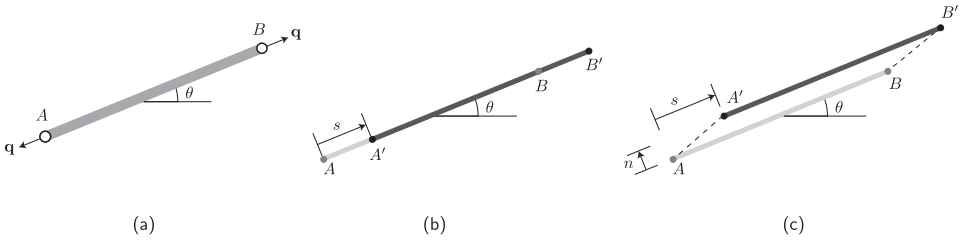
Figure A.1: Variables in truss and DLO problems: (a) force variable of a truss bar i; (b) shear displacement variable of a slip-line i moving from AB to $A'B'$; (c) shear and normal displacement variables. For (b) and (c) and sign convention adopted in this work, the indicated relative displacement jump occurs moving across the discontinuity from below to above.

displacements along the discontinuities; λ is the load factor, and so $\lambda \mathbf{f}_L^T \mathbf{d}$ in Eqn. (A.1a) is the live loads work. Also, $\mathbf{p}$ is a vector of non-negative plastic multipliers used to describe the plastic flow of the discontinuities, and so the right hand side of Eqn. (A.1a) is the internal energy dissipation. With this in mind, the objective function Eqn. (A.1a) identifies the minimum value of the live load that causes the collapse of the structure.

Although theoretically live loads can be applied to any discontinuity, in general they are only applied to discontinuities lying on free boundaries, such that S_{Li} and N_{Li} is zero for any non-free boundary i.

The displacements involved are all *relative* and the following sign convention is adopted: shear displacements s are taken as positive clockwise (as shown in Fig. 2.13b) and normal displacements n dilational displacements are taken as positive. Thus 'inward' displacement into a body at a boundary corresponds to dilation at that boundary and correspondingly a normal load at a boundary is considered positive if it is applied inwards with respect to the domain boundary, such that it does positive work. So, for example, if the same positive load is applied to the upper boundary or to the lower boundary it is oriented downwards or upwards respectively. In a same way a boundary shear load is considered positive if it acts anti-clockwise around the boundary.

In Equation (A.2), the compatibility matrix $\mathbf{B}_i$ of the ith discontinuity can be written as:

$$\mathbf{B}_i \mathbf{d}_i = \begin{bmatrix} \alpha_i & -\beta_i \\ \beta_i & \alpha_i \\ -\alpha_i & \beta_i \\ -\beta_i & -\alpha_i \end{bmatrix} \begin{bmatrix} s_i \\ n_i \end{bmatrix} = \mathbf{0} \tag{A.2}$$

where $\alpha_i = \cos\theta_i$ and $\beta_i = \sin\theta_i$ are the direction cosines associated with the discontinuity.

Constraint (A.1c) imposes a flow rule linking displacements s_i and n_i. For the example shown in Fig. A.1b, only shear plastic flow is involved, such that

the flow rule of the ith slip-line would be written as:

$$\mathbf{N}_i \mathbf{p}_i - \mathbf{d}_i = \begin{bmatrix} 1 & -1 \\ 0 & 0 \end{bmatrix} \begin{bmatrix} p_{1,i} \\ p_{2,i} \end{bmatrix} - \begin{bmatrix} s_i \\ n_i \end{bmatrix} = \mathbf{0} \qquad \text{(A.3)}$$

where the normal plastic flow is set to zero. Note that the flow rule constraint (A.3) is applied to all internal slip-lines. For what regards boundary slip-lines, the equation needs to be modified to satisfy each boundary condition.

Note that the use of $p_{1,i} + p_{2,i}$ in the work equation A.1a, with $p_{1,i}$, $p_{2,i} \geq 0$, ensures that work done is always positive, regardless of the direction of displacement s_i. Since Eq. (A.1a) is being minimized, the flow rule can be viewed as being equivalent $p_{1,i} + p_{2,i} = |s_i|$; this is illustrated on Table A.1, which shows a range of possible $p_{1,i}$, $p_{2,i}$ values for cases where $s_i = 10$ or $s_i = -10$, indicating that the optimal (lowest) value will always occur when $p_{1,i} + p_{2,i} = |s_i|$.

Table A.1: Examples of plastic multiplier values, $p_{1,i}$, $p_{2,i}$, showing that the optimal (minimum) work value coincides with $p_{1,i} + p_{2,i} = |s_i|$.

$s_i = p_{1,i} - p_{2,i}$	$p_{1,i}$	$p_{2,i}$	Work $(p_{1,i} + p_{2,i})c_i l_i$	Minimum?
10	10	0	$10c_i l_i$	Yes
10	11	1	$12c_i l_i$	No
10	15	5	$20c_i l_i$	No
-10	0	10	$10c_i l_i$	Yes
-10	1	11	$12c_i l_i$	No
-10	5	15	$20c_i l_i$	No

Live load is applied directly on boundary discontinuities. For the sake of simplicity, a unit normal load is used:

$$\mathbf{f}_{\text{L}i}^{\text{T}} = \begin{cases} [0, l_i], & \text{for } i \in \mathbb{F}, \\ [0, 0], & \text{otherwise,} \end{cases} \qquad \text{(A.4)}$$

where $\mathbb{F}$ is a set containing discontinuities where a load is applied, and l_i is the length of the ith discontinuity. Note that this defines a 'flexible' load, i.e., the loaded boundary line is free to deform since each normal displacement can be different.

A.1.1. Boundary conditions

As mentioned previously, boundary conditions affect the flow rule and work terms associated with the relevant discontinuities. For a fixed boundary, there's no need to add further constraints, since the relevant discontinuities have the same properties as internal ones. For free boundaries, the flow rules in (A.1c) do

not need to be applied, since the displacements (i.e., s_i and n_i) don't need to be coupled. In addition, since no internal energy is dissipated on free boundaries, plastic multiplier terms are not included in the work calculation, Eqn. (A.1a).

In the examples considered in this Appendix, each boundary is visually represented as follows:

- **Free boundary**: line only

- **Fixed boundary**: cross hatch

- **Symmetry boundary**: dot-dash line

- **Loaded boundary**: directional load arrows

A.2. Python implementation of basic DLO formulation

The formulation described in Section A.1 has been programmed in the Python script `dlo_basic`.

A.2.1. Program code excerpts

The key parts of the formulation described in Section A.1 are now associated with the corresponding program code. Specifically, function `DLO` performs the high-level steps required to solve a DLO problem.

Firstly a polygonal problem domain is created:

```
poly = Polygon(vt)
```

in which the geometrical library `shapely` is used to generate a polygon using its vertices `vt`.

Nodes and discontinuities are then generated:

```
Nd = createNodes(poly)
Cn = createDiscontinuities(poly, Nd)
```

where `Nd` is a $(n \times 2)$ array of nodes, with rows defining the x and y coordinates of nodes. `Cn` is a $(m \times 3)$ array of discontinuities, with each row defining the indices of the connected nodes and the discontinuity length. Note that only nodes and discontinuities lying entirely inside the polygonal domain are created and this allows to also deal with convex geometries. Also, overlapping connections are filtered out to remove redundant collinear discontinuities.

Boundary conditions are then defined:

```
bd = setCnBoundaryCondition(Nd,Cn,vt,edgebd)
```

which generates an array `bd` defining boundary conditions for all discontinuities.

A DLO problem is then set up and solved:

```
factor, d, p = solveLP(Nd, Cn, bd, mat)
```

and results are displayed graphically:

```
plot(vt, d, Cn, Nd, bd)
```

Further details of the key steps involved are now presented.

Setting up the DLO optimisation problem

As successfully utilized by He et al. (2019), the convex optimisation package `cvxpy` (Diamond and Boyd 2016) is here used to solve the minimization problem (A.1), processed in function `solveLP`.

Firstly, all coefficient vectors and matrices in problem (A.1) are obtained:

```
B  = calcB(Nd, Cn)
N  = calcN(bd)
g  = calcg(Cn, mat['cohesive'])
fL = unitLoad(bd)
```

Boundary conditions are then considered:

```
activeN, activeG = boundaryConditions(bd)
```

which generates two vectors `activeN` and `activeG`, containing binary data used later to impose boundary conditions to the flow rule matrix `N` and the energy dissipation vector `g`.

Optimisation variables are then created:

```
d = cvx.Variable(2 * m)
p = cvx.Variable(2 * m)
```

Note that matrix multiplications in `cvxpy` (from version 1.0) are defined using the symbol "@". The objective function (2.105a) is created using:

```
energy = (g * activeG).transpose() @ p
obj = cvx.Minimize(energy)
```

where the array `activeG` is used as a mask to set certain coefficients in `g` to 0, to fit the boundary conditions involved.

All constraints in problem (A.1) are contained in a list `cons`:

```
cons = []
cons.append(B @ d == 0)
cons.append(fL @ d == 1)
cons.append(p >= 0)
cons.append(cvx.multiply(N@p-d,activeN)==0)
```

The optimisation problem can now be created and solved:

```
prob = cvx.Problem(obj, cons)
factor = prob.solve(solver='ECOS')
```

where here the LP problem is initially solved via the free `ECOS` solver (Domahidi et al. 2013), which is installed with the `cvxpy` package. The optimisation variables can then be obtained:

```
d = np.array(d.value).flatten()
p = np.array(p.value).flatten()
```

Compatibility constraints

To improve computer memory efficiency, the compatibility matrix in Eq. (A.2) is stored in a sparse matrix. Therefore, it is necessary only the values and locations of non-zeros (i.e., row and column identifiers) in matrix $\mathbf{B}$. Since `numpy` can handle element-wise calculations in arrays, it is convenient to define local compatibility matrices for all discontinuities:

```python
s, n = np.arange(0,2*m,2), np.arange(1,2*m,2)
alpha, beta = X / l, Y / l
values = [[alpha, -beta],
          [beta, alpha],
          [-alpha, beta],
          [-beta, -alpha]]
rows = [n1*2,
        n1*2+1,
        n2*2,
        n2*2+1]
columns = [s, n]
```

where here `s` and `n` are respectively vectors of shear and normal displacements in $\mathbf{d}$; see equation (A.1b). Also `n1` and `n2` are indices of the first and second nodes connected by discontinuities.

The above script collects all non-zeros in the $\mathbf{B}$ matrix and their corresponding locations. To create the sparse matrix, the following function is called:

```python
return toSparseMatrix(values, rows, columns, shape = (n
    *2, m*2))
```

which creates a $2n \times 2m$ sparse matrix using the non-zeros provided.

Flow rule

The flow rule matrix N in Eq. (A.3) is calculated as follows:

```python
values = [[one , -one],
          [zero, zero]]
columns = [s, n]
rows = [np.arange(0,2*m,2),\
        np.arange(1,2*m, 2)]
```

Applied loading

In accordance with Eq. (A.4), loads can be applied to discontinuities lying along boundaries using the following code fragment:

```python
m, l = len(bd), Cn[:,2]
loadedCn = np.where(bd == BD.Load)[0]
fL = np.zeros((m, 2))
fL[loadedCn, 1] = l[loadedCn]
```

Note that this applies a 'flexible' unit load (since no kinematic constraints have been created to link together the displacements of adjacent loaded segments).

A.2.2. Illustrative examples

The formulation described is now applied to simple literature problems. For all problems a laptop PC equipped with an Intel I7-7700HQ CPU and running 64-bit Windows 10 was used. These problems are characterized by a pure cohesive model (i.e., can be described by the Tresca failure envelope, in which only shear plastic strains occur).

Metal extrusion

The first example is a classical metal extrusion problem considered by Hill (1950), in which metal is pushed through a rectangular die by a ram, leading to 'steady motion' metal extrusion (i.e., a uniform displacement (rate) field at the bottom boundary).

Figure A.2 presents results for three different domain heights. It is evident that a slip-line field similar to that obtained by Hill is only obtained when the loaded boundary is a sufficient distance from the opening. This is because the loading presented in Sec. A.2.1 is 'flexible', and does not ensure a uniform displacement field is present at the loaded boundary; this can be addressed by instead using a rigid load, as described in Sec. A.4.

| (a) | (b) | (c) |
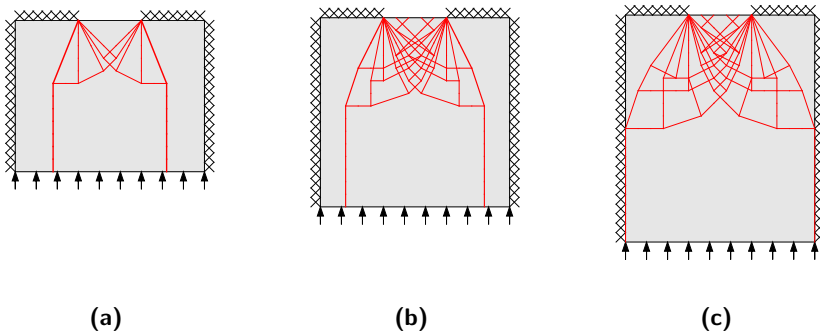
Figure A.2: Metal extrusion (1/3 opening on the top edge): (a) 15x12 nodal divisions, $\lambda = 4.237$; (b) 15x15 nodal divisions; $\lambda = 4.841$; (c) 15x18 nodal divisions, $\lambda = 5.320$. ($c = 1$)

Prandtl punch

Figure A.3(a) shows a variant of the well-known Prandtl punch problem (Hill, 1950). Taking symmetry conditions into account, a rectangular domain with 10×5 nodal divisions is used here; see Fig. A.3(b). The load factor obtained is 5.222, which is just 1.56% above the analytical solution of $2+\pi$. A major benefit of the DLO method compared with comparable finite element analysis methods is that the singularity in the displacement field that occurs at the edge of the punch is identified automatically, without the need for e.g., tailored

meshes or adaptive mesh refinement.

(a)

(b)
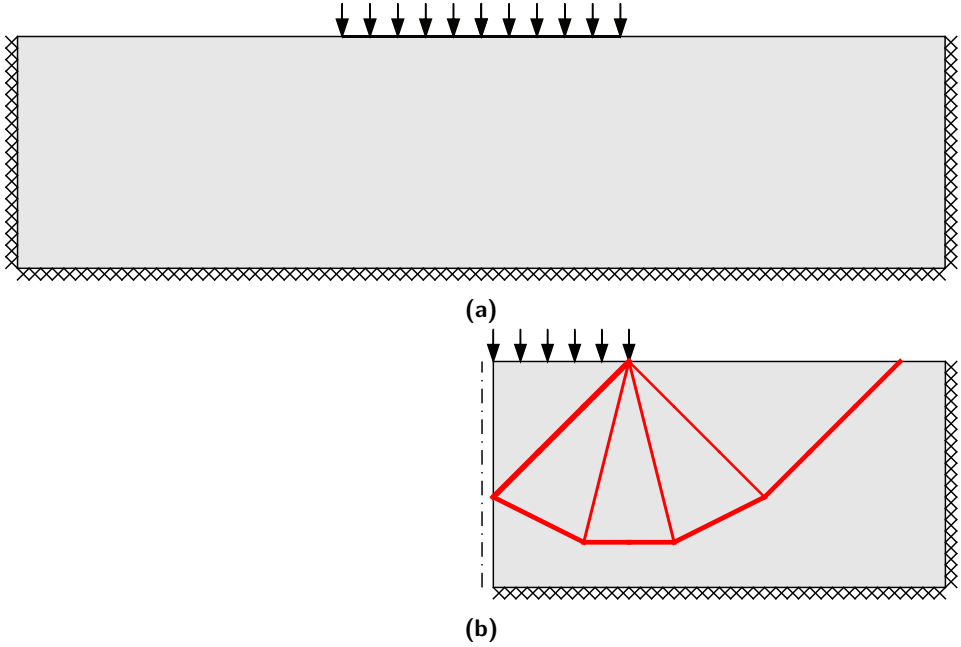
Figure A.3: Prandtl punch: (a) problem specification; (b) half domain discretized using 10×5 nodal divisions; unit load applied along 3 nodal divisions of the top edge. Load factor $\lambda = 5.222$ (taking cohesion $c = 1$).

A.3. Extensions
A.3.1. Cohesive frictional materials

By changing the flow rule matrix it is possible to treat different convex yield surfaces. For example, it is straightforward to implement the Mohr-Coulomb model for treating cohesive frictional materials.

To achieve this no changes to the compatibility conditions imposed in Eq. (2.105b) are required, since normal displacements were already included in the basic DLO formulation (e.g., to permit the presence of normal displacements at boundaries).

However, to implement the Mohr-Coulomb model the flow rule constraints need to be modified as follows:

$$\mathbf{N}_i \mathbf{p}_i - \mathbf{d}_i = \begin{bmatrix} 1 & -1 \\ \tan\phi & \tan\phi \end{bmatrix} \begin{bmatrix} p_i^1 \\ p_i^2 \end{bmatrix} - \begin{bmatrix} s_i \\ n_i \end{bmatrix} = \mathbf{0}, \qquad \text{(A.5)}$$

where $\mathbf{N}_i$ is the local plastic flow matrix, $\mathbf{p}_i$ is a vector containing non-negative plastic multipliers, and ϕ is the angle of friction of the material.

A.3.2. Rigid loads

In contrast to the 'flexible' loads defined using Eqn. (A.4), it is possible to specify rigid loads, where the shape of a given loaded boundary line remains fixed. For rigid loads, all displacement of discontinuities belonging to the rigid load boundary share the same value (see Table 2.1). It can be implemented by introducing additional equality constraints to link the displacement variables involved:

```
linkN, linkS = processCnLinks(bd)
if len(linkN):
    nL = d[linkN * 2 + 1]
    cons.append(nL[1:] == nL[:-1])
if len(linkS):
    sL = d[linkS * 2]
    cons.append(sL[1:] == sL[:-1])
```

where `linkN` and `linkS` are arrays containing the indices of discontinuities to be linked, considering normal and shear displacements respectively; `sL` and `nL` are arrays of the corresponding displacement variables.

A.3.3. Treatment of body forces
Theory

In previous work (e.g Smith and Gilbert 2007) the work done by body forces was implemented by considering the work done moving a column of material that lies e.g. vertically above a given slip-line discontinuity. For simple examples involving domains with a flat uppermost boundary (e.g., see Fig. A.4(a)), it is relatively easy to calculate the gravity load imposed by materials lying above any discontinuity. However, for general cases, the calculations can become complex. For example, in Fig. A.4(b), since the uppermost edge is non-smooth, any algorithm developed to calculate the gravity load would need to first identify intersection points on this edge in order to obtain polygonal areas above each underlying discontinuity line. Due to the requirement to calculate intersection points, this process can also become computationally expensive when a large number of discontinuities are present in a given DLO problem. For this reason, handling distributed body forces was identified as an area of weakness for DLO by He and Gilbert (2016).

However, following recent work by Smith and Gilbert (2022), a simpler and more elegant approach becomes possible. Here this will be described from a conceptual standpoint, with details of the derivation available for interested readers in Smith and Gilbert (2022).

Consider first a body containing only a non-dilational material within which a translational mechanism is formed. Due to conservation of volume, all normal displacements at the domain boundary must sum to zero. To an external observer, material that is displaced at one boundary discontinuity by a normal displacement must 'reappear' at one or more other boundary discontinuities. For
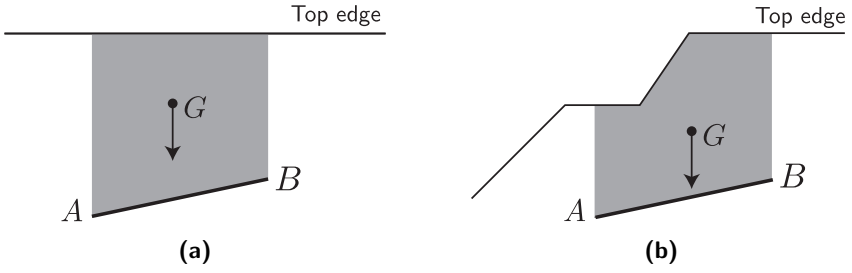
Figure A.4: Challenges to calculate body force G of the shaded area for a discontinuity AB using the approach described in Smith and Gilbert (2007): (a) flat top edge, simple algorithm is available to calculate the area 'above' the discontinuity, e.g., in Gilbert et al. (2010); (b) non-smooth top edge, more complex algorithm is required, where the shape of the top edge must be considered.

example in Figure A.3 the volume of material pushed downwards by the punch indenter must equal the volume pushed upwards either side of the indenter.

To compute the work done by body forces, it is therefore not necessary to track the movement of material throughout a body (since this is done implicitly by enforcing compatibility elsewhere in the DLO formulation), but to simply note the potential of material that vanishes (positive normal displacement), or appears (negative normal displacement) at a boundary and sum these to form the body force work term. Shear displacements do not affect volume and so have no effect.

General equations

As already outlines in 2.4.2 the loss of body force potential P_i due to a normal displacement n_i is given by Eqn. (2.109).

For a material that undergoes volume change on deformation, e.g., dilation, the argument can be extended to include volume generation (or loss) internal to the body and Eqn. (2.109) is unchanged.

When combined with discrete loads applied to any discontinuity, this gives the general equation for loading (live or dead) on a discontinuity i as follows:

$$\mathbf{f}_i^{\mathrm{T}} \mathbf{d}_i = \left[\begin{array}{cc} S_i, & \gamma l_i(-k_v \cdot y_m - k_h \cdot x_m) + N_i \end{array} \right] \left[\begin{array}{c} s_i \\ n_i \end{array} \right] \tag{A.6}$$

where S_i and N_i are respectively a shear and normal load applied to the discontinuity. Body forces may be applied as either live or dead loads. In this work, gravity loads are always considered to be dead loads, and therefore Eq. (A.6) can be simplified to:

$$\mathbf{f}_{\mathrm{D},i}^{\mathrm{T}} \mathbf{d}_i = \left[\begin{array}{cc} 0, & \gamma \cdot l_i \cdot y_{m,i} \end{array} \right] \left[\begin{array}{c} s_i \\ n_i \end{array} \right], \tag{A.7}$$

which involves significantly simpler computations than those associated with the strip model shown in Fig. A.4.

To accommodate such body forces it is necessary to extend equation A.1a to now include dead loads (D) as follows:

$$\min_{\mathbf{d},\mathbf{p}} \lambda \mathbf{f}_L^T \mathbf{d} = \mathbf{g}^T \mathbf{p} - \mathbf{f}_D^T \mathbf{d} \tag{A.8}$$

A.3.4. Alternative LP solvers

By default, the LP problem (A.1) is solved using the open-source solver ECOS (Domahidi et al. 2013) that is distributed with `cvxpy`. However, `cvxpy` also supports many other, potentially more efficient, solvers - albeit these need be installed separately by users. For example, to use the MOSEK solver (MOSEK ApS 2019), the `solve` command in function `solveLP` is replaced with the following:

```
factor, d, p = prob.solve(solver = cvx.MOSEK,\
    mosek_params={"MSK_IPAR_INTPNT_BASIS":0})
```

The MOSEK parameter `"MSK_IPAR_INTPNT_BASIS"` disables the unnecessary basis identification step to improve speed.

A.3.5. Adaptive solution procedure

Similar to the 'member adding' procedure applied to numerical truss layout optimisation problems (Gilbert and Tyas 2003; He et al. 2019), an adaptive solution scheme can be employed when solving DLO problems, significantly improving computational efficiency. Figure A.5 shows how a solution is obtained for a Prandtl punch problem when using the adaptive solution process. For sake of simplicity, in this work all potential discontinuities are created, Fig. A.5(c), and only small subsets are selected to solve problem (A.1), e.g., Fig. A.5(d)-(i). Note that it is possible to improve the memory efficiency further by skipping the step in Fig. A.5(c) and only storing the required subsets.

In the adaptive solution procedure, the dual problem of (A.1) is examined. Using duality theory (e.g., see He et al. 2019), the dual problem of (A.1), extended in (A.8), is shown in Eqn. (2.110)

When the primal problem (A.1) is solved via the primal-dual interior point method, the nodal forces $\mathbf{t}$ at every node is obtained from the compatibility constraints. Therefore, the discontinuity force vector $\mathbf{q}$ for all potential discontinuities (i.e., discontinuities that are not included in the primal problem) can be obtained from the equality constraint (2.110b):

```
q = B.transpose().dot(t) + factor * fL + fD
```

Since the potential discontinuities are not included in the primal problem, yield condition (2.110c) may not be satisfied for all those discontinuities. Their violations can be calculated:
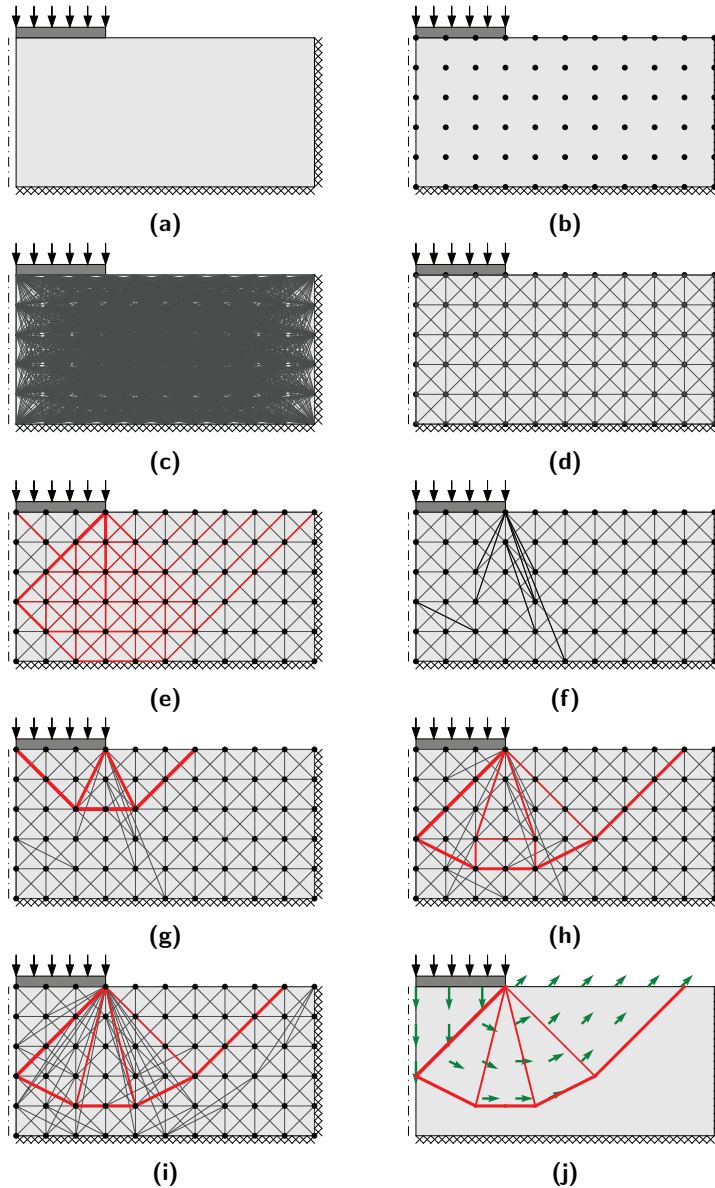
Figure A.5: Solve a DLO problem via the adaptive solution scheme: (a) Problem specification; (b) node discretisation (10×5 divisions); (c) create all potential discontinuities by interconnecting every possible pair of nodes (1361 potential discontinuities); (d) only activate a small subset of discontinuities (215 discontinuities activated); (e) iteration 1, solve problem (A.1), $\lambda = 6.000$; (f) check dual violation using (2.112), and activate the most violated discontinuities via (A.9); (g) iteration 2, $\lambda = 5.333$, with dual violation; (h) iteration 4, $\lambda = 5.259$, with dual violation; (i) final iteration, $\lambda = 5.222$, no dual violation, 248 activated discontinuities in total; (j) highlight discontinuities with non-zero energy dissipation, and show displacement vectors using algorithms in Section A.3.6

```
y = N.transpose().dot(q) / g
```

Note that for each discontinuity, two violation numbers, corresponding to the two inequality constraints in (2.112), are obtained. They are extracted using

```
vio1 = y[np.arange(0, m * 2, 2)]
vio2 = y[np.arange(1, m * 2, 2)]
```

And all discontinuities are sorted by their violation numbers in descending order:

```
vio = np.vstack((vio1, vio2))
vio = np.amax(vio, axis=0)
```

   To prevent dual violations, the violated discontinuities should be added to the primal problem in the next iteration. To improve computational efficiency, only the most violated discontinuities are added. Denote m_v the number of violated discontinuities, m_p the number of potential (i.e., inactivated) discontinuities. The following selection criteria is used to obtain the number of the most violated discontinuities:

$$\Delta m = \begin{cases} \kappa_1 m_{\mathrm{v}}, & m_{\mathrm{v}} \geq \kappa_2 m_{\mathrm{p}} & \text{(A.9a)} \\ m_{\mathrm{v}}, & m_{\mathrm{v}} \leq \kappa_1 \kappa_2 m_{\mathrm{p}} & \text{(A.9b)} \\ \kappa_1 \kappa_2 m_{\mathrm{p}}, & \kappa_1 \kappa_2 m_{\mathrm{p}} < m_{\mathrm{v}} < \kappa_2 m_{\mathrm{p}}, & \text{(A.9c)} \end{cases}$$

where Δm is the number of discontinuities to be added; κ_1 and κ_2 are coefficients determining the percentage of new discontinuities to be added. In this work, both coefficients are taken as 0.05. In (A.9), if the number of violated discontinuities is relatively large ($m_{\mathrm{v}} \geq \kappa_2 m_{\mathrm{p}}$), only a small proportion of the violated discontinuities are added, (A.9a). This prevents the problem from growing very rapidly during early iterations of the adaptive solution process, where a large number of dual violations are expected. On the other hand, if the number of violated discontinuities is relatively small ($m_{\mathrm{v}} \leq \kappa_1 \kappa_2 m_{\mathrm{p}}$), all the violated discontinuities will be added, (A.9b), as they will only slightly increase the size of the problem. Otherwise, if the number of violated discontinuities is neither large nor small, a fixed proportion of the inactivated discontinuities are added, (A.9c). If no violation is detected among all potential discontinuities, there is no new discontinuities to be added (i.e., $\Delta m = m_{\mathrm{v}} = 0$), and the adaptive procedure completes.

   Note that selection criteria (A.9) is based on heuristics; it is therefore possible to design different strategies. Nevertheless, it is important to state that, the adaptive procedure is guaranteed to obtain the same load factor as that obtained by solving the full problem, regardless of the specific heuristics used.

A.3.6. Graphical display of mechanism and kinematics

   To give a visual indication of movements, a grid of displacement vectors can be overlain on any mechanism. This can be achieved by running horizontal scan

lines across the domain at regular y-intervals. The absolute displacement is set to zero where the scan line lies outside the domain. As the scan line crosses the domain from left to right, it will cross discontinuities. At each crossing the absolute displacement is updated by adding the relative displacement that is incurred when crossing the discontinuity. The absolute displacement can then be noted at regular x-intervals along the scan line.
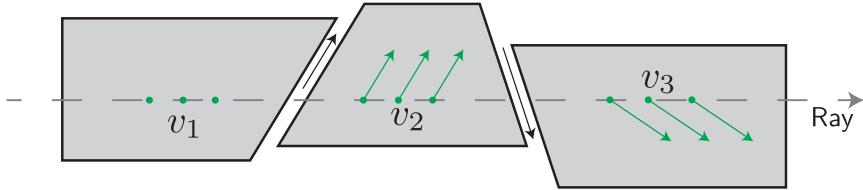

Figure A.6: Generating velocity field by collecting velocity jumps at intersections between discontinuities and a ray

A.4. Numerical examples

In this section several examples involving the features presented in Sec. A.3 are shown. In all the following examples a rigid load is present unless stated otherwise.

A.4.1. Metal extrusion example revisited

Taking advantage of features introduced in Section A.3, here the metal extrusion example in Section A.2.2 is considered. Since the ram can now be modelled using rigid load to ensure a 'steady motion', there is no need to set the loaded boundary sufficiently away from the opening; and a square domain is used. Also, to obtain more accurate solutions than Fig. A.2(c), nodal divisions are increased. Fig. A.7 shows the results obtained using 30×30 and 60×60 nodal divisions; and Table A.2 provides a summary of the solutions with varying nodal divisions. Since the number of total discontinuities increases extremely rapidly with the nodal divisions, it is difficult to solve the full problem without the adaptive solution procedure. The ECOS solver failed to obtain solutions after the nodal division is increased from 15×15 to 30×30; so the more efficient MOSEK solver is utilized. On the other hand, using the adaptive solution procedure, the problems become significantly less difficult to solve, so the computational efficiency is increased. For example, the ECOS solver can solve the problem with 60×60 nodal divisions; and large speed up factors are found in relatively large problems using MOSEK solver. It is important to note that, although for each problem the CPU costs vary largely with different approaches (i.e., full problem or adaptive solution) and solvers (ECOS or MOSEK), the reported load factors remain the same.

(a)　　　　　　　　　　　　　**(b)**
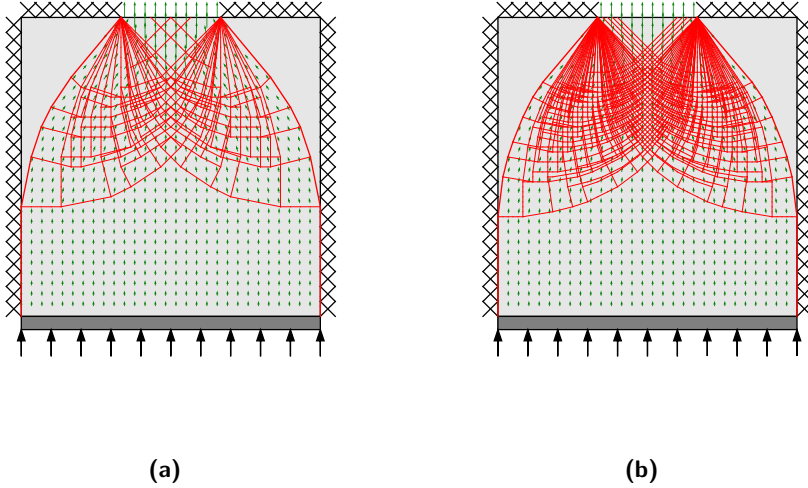
Figure A.7: Metal extrusion example revisited: (a) 30×30 nodal divisions, $\lambda = 4.880$; (b) 60×60 nodal divisions, $\lambda = 4.861$. $(c = 1)$

Table A.2: Metal extrusion example revisited: results for various nodal divisions

Nodal division	Num. of total	Load factor	CPU time (ECOS)		CPU time (MOSEK)		
$(x \times y)$	discontinuities	λ	Full (s) [†]	Adaptive (s) [‡]	Full (s) [†]	Adaptive (s) [‡]	Speed up factor
15×15	20,074	4.920	3	1	1	1	1
30×30	280,916	4.880	-	9	21	9	2.3
45×45	1,362,082	4.868	-	52	114	24	4.8
60×60	4,209,056	4.861	-	457	514	98	5.2
75×75	10,145,578	4.858	-	-	2281	183	12.5

†: cumulative CPU time spent in function `solveLP`

‡: cumulative CPU time spent in functions `SolveLP` and `stopViolation`

- : maximum number of iterations reached in ECOS

Metal block compressed between rough platens

The second example is a rectangular metal block that is compressed vertically between two rough platens. The analytical solution has been provided by (Chakrabarty (1991),Chakrabarty (2006)). In fact, the problem is in analogy with the optimal layout of trusses for the cantilever truss problem (Lewiński et al. (1994) / Johnson (1961)), if only half the width of the metal block is observed; and the layout of discontinuities at failure exactly matches the layout of (near-)optimum trusses with minimum volume design. Here three different aspect ratios are considered, and the results are shown in Table A.3. For sake of clarity, Fig. A.8 shows the corresponding slip-line patterns obtained with relatively small nodal divisions.
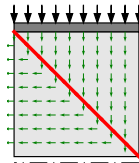
(a)
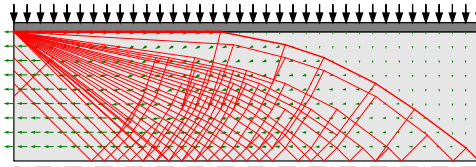
(b)
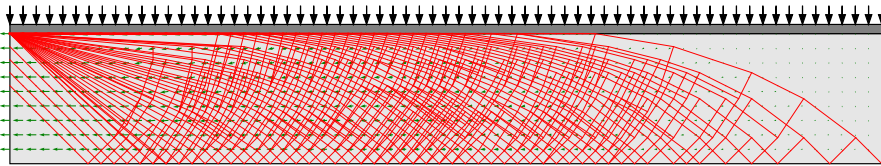
(c)

Figure A.8: Metal block compressed between rough platens: (a) $10{\times}10$ nodal divisions, aspect ratio $= 1$, $\lambda = 2.000$; (b) $36{\times}10$ nodal divisions, aspect ratio $= 3.6$, $\lambda = 3.325$; (c) $67{\times}10$ nodal divisions, aspect ratio $= 6.7$, $\lambda = 4.978$ $(c = 1)$

Table A.3: Metal block compressed between rough platens: results for various block width : height aspect ratios

Block width : height aspect ratio	Analytical: λ	Numerical:			
		Nodal division ($x \times y$)	λ	Error%	CPU (s) [†]
1	2.000	25×25	2.000	0.00	2
3.644	3.334	91×25	3.335‡	0.03	80
6.718	4.894	168×25	4.900‡	0.11	116

†Adaptive solution procedure via the MOSEK solver
‡Aspect ratios of 3.64 and 6.72 were used in the numerical studies.

A.4.2. Geotechnical examples

With the Mohr Coulomb failure criteria (Section A.3.1) and body forces (Section A.3.3), the DLO formulation (A.1) can be used to solve a range of geotechnical problems.

Bearing capacity problem with cohesive frictional soil

Here the inclusion of friction is illustrated by modification of the Prandtl punch problem considered in Section A.2.2 to a bearing capacity problem involving a Mohr Coulomb failure criteria (cohesive-frictional soil). The soil is considered weightless, in which case the analytical solution can be obtained via $\lambda = c \cdot (N_q - 1) \cot \phi$, where c is the cohesion, ϕ is the angle of friction and $N_q = \exp(\pi \tan \phi) \tan^2(45 + \phi/2)$. To model the problem, here the half domain is discretized with 48×16 nodal divisions, taking into account symmetry conditions, and a unit rigid load of 5 nodal divisions is applied. The value obtained for λ in this analysis is 21.0124 (Fig. A.9) where $N_q = 10.66$, which differs from the analytical value of 20.721 by 1.4%.
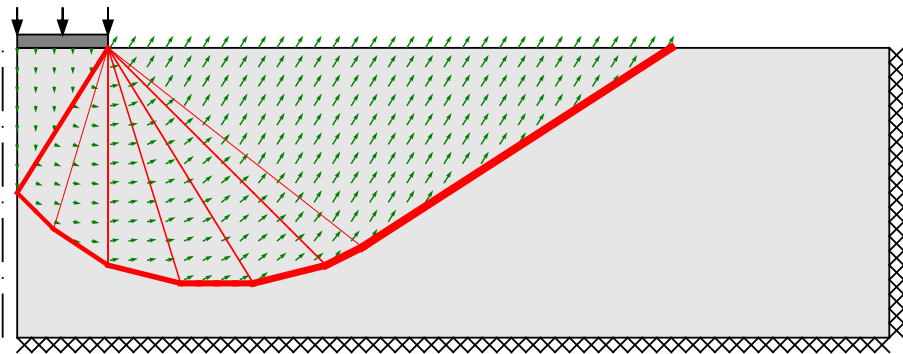

Figure A.9: Bearing capacity problem with cohesive frictional soil: with rigid load applied over a length of 5 nodal divisions and with domain discretized with 48×16 nodal divisions. Load factor $\lambda = 21.024$. ($c = 1, \phi = 25°, \gamma = 0$)

Retaining wall

Here the inclusion of self weight is illustrated through the analysis of a geotechnical retaining wall problem. The "passive state" is considered, which identifies the lateral resistance of a soil body when the wall is pushed towards it, see Fig. A.10. The soil cohesion and unit weight are taken as unity and $\phi = 20°$. The domain is discretized using 40×20 nodal divisions, and a unit rigid load is applied on the left boundary. The load factor obtained is 23.254 which is 0.007% higher than the theoretical value of 23.252 ($\lambda = 0.5K_p\gamma H + 2c\sqrt{K_p}$, where $K_p = \tan^2(45 + \phi/2)$, and $H = 20$ is the wall height).
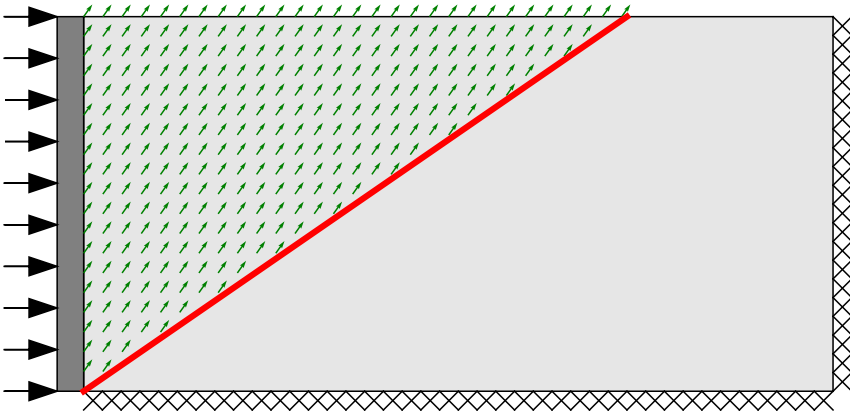
Figure A.10: Retaining wall: using unit rigid load and 40×20 nodal divisions. Load factor $\lambda = 23.254$. ($c = 1, \phi = 20°, \gamma = 1$)

Terraced slope with crest surcharge

Figure A.11 shows a slope stability problem with a rigid load at the crest. The Mohr-Coulomb failure criterion is used in the soil ($c = 1$, $\phi = 25°$), and the unit weight is set to $\gamma = 1$. Since the slope has a non-smooth top-surface, it becomes challenging to calculate the load effects of the self-weight of soils using approaches from previous work (e.g., Smith and Gilbert (2007); Gilbert et al. (2010), see also Fig. A.4). Using the new body force formulation (2.109), the load effects can be calculated very efficiently. The non-convex domain is discretized with (20×12) nodal division, and nodes outside the domain are removed in function `createNodes`; similarly, discontinuities intersecting the concave edges on the top-surface are removed in function `createDiscontinuities`.

The failure mechanism in Fig. A.11 shows a partly curved slip-line, which converts the vertical displacement of the rigid plate to horizontal movements of the soils, as observed from the displacement vectors.

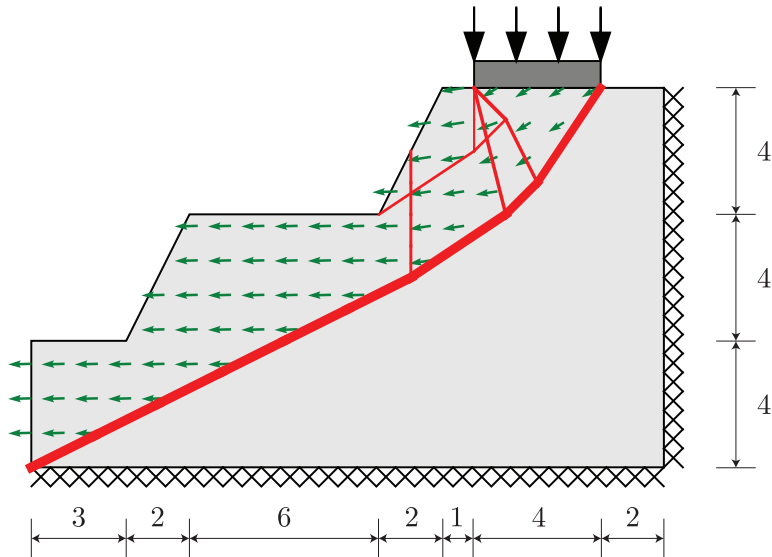**Figure A.11:** Terraced slope with crest surcharge: using 20×12 nodal divisions, load factor $\lambda = 9.170$. $(c = 1, \phi = 20°, \gamma = 1)$

A.5.Running the example problems

Two main scripts have been prepared and made available as supplementary material; the first, `DLO_basic.py`, covers the basic DLO formulation described in Sect. A.2; the second, `DLO.py`, incorporates the extensions described in Sect. A.3. For readers unfamiliar with DLO it is strongly recommended that `DLO_basic.py` is referred to first as this is shorter and has been designed to be as accessible as possible. (Note that `DLO.py` also includes code optimizations to improve speed, e.g., loops have been replaced with vectorized calculations.)

Both the scripts depend on a number of packages that can be installed via the `conda` cross-platform command line package management tool distributed with Anaconda (which is freely available from `https://www.anaconda.com/download` and also includes a Python development environment):

```
conda install numpy
conda install scipy
conda install shapely
conda install -c conda-forge cvxpy
conda install matplotlib
```

To allow readers to run the example problems, an additional script, `example.py`, has been prepared. This includes functions to run each of the examples

considered in this work (Table A.4) and to solve all examples considered in this work in sequence, readers can run the following command in a terminal:

```
python example.py
```

In addition, to obviate the need to install Python and associated packages, the scripts have also been made available via Google Colab (Bisong 2019), at: https://colab.research.google.com/drive/1qgXhlD2JSC_pKU_PF0p3kECFiM9gXTYd. Entering this url in a web browser automatically runs all examples - scroll to the bottom of the page to view the text and graphical output generated for all problems, which will take a few seconds to appear. This link will work for as long as Google Colab services remain publicly available.

Table A.4: Python function calls for all example problems

Description	Figure	Python function
Extrusion (flexible load)	Fig. A.2(a)	Extrusion12()
	Fig. A.2(b)	Extrusion15()
	Fig. A.2(c)	Extrusion18()
Prandtl punch	Fig. A.3	Prandtl()
Extrusion (rigid load)	Fig. A.7(a)	Extrusion30()
	Fig. A.7(b)	Extrusion60()
Metal compressed	Fig. A.8(a)	Metal10()
	Fig. A.8(b)	Metal36()
	Fig. A.8(c)	Metal67()
Bearing capacity	Fig. A.9	Bearing()
Retaining wall (passive failure),	Fig. A.10	Retaining()
Slope	Fig. A.11	Slope()

Bibliography

Angelillo, M., Lourenço, P., and Milani, G. (2014). Masonry behaviour and modelling. volume 51. Springer,Vienna, m.angelillo edition.

Anthoine, A. (1995). Derivation of the in-plane elastic characteristics of masonry through homogenization theory. *International Journal of Solids and Structures*, 32(2):137–163.

Anzani, A., Binda, L., Carpinteri, A., Lacidogna, G., and Manuello, A. (2008). Evaluation of the repair on multiple leaf stone masonry by acoustic emission. *Materials and Structures*, 41:1169–1189.

Argyris, J. H. and Kelsey, S. (1960). *Energy theorems and structural analysis*, volume 60. Springer.

Bathe, K.-J. (2006). *Finite element procedures*. Klaus-Jurgen Bathe.

Bisong, E. (2019). *Google Colaboratory*, pages 59–64. Apress, Berkeley, CA.

Borri, A., Corradi, M., and De Maria, A. (2020). The failure of masonry walls by disaggregation and the masonry quality index. *Heritage*, 3(4):1162–1198.

Borri, A., Corradi, M., Giulio, C., and De Maria, A. (2015). A method for the analysis and classification of historic masonry. *Bulletin of Earthquake Engineering*, 13(4):2647–2665.

Cavalagli, N., Cluni, F., and Gusella, V. (2011). Strength domain of non-periodic masonry by homogenization in generalized plane state. *European Journal of Mechanics - A/Solids*, 30(2):113–126.

Bibliography

Cavalagli, N., Cluni, F., and Gusella, V. (2013). Evaluation of a Statistically Equivalent Periodic Unit Cell for a quasi-periodic masonry. *International Journal of Solids and Structures*, 50(25-26):4226–4240.

Cavalagli, N., Cluni, F., and Gusella, V. (2018). Failure surface of quasi-periodic masonry by means of statistically equivalent periodic unit cell approach. *Meccanica*, 53(7):1719–1736.

Chaboche, J. (2008). A review of some plasticity and viscoplasticity constitutive theories. *International Journal of Plasticity*, 24(10):1642–1693. Special Issue in Honor of Jean-Louis Chaboche.

Chakrabarty, J. (1991). The analytical solution of some boundary value problems in plane plastic strain. *International Journal of Mechanical Sciences*, 33(2):89–99.

Chakrabarty, J. (2006). *Theory of plasticity*, page 685–690. Oxford UK: Butterworth-Heinemann, 3 edition.

Clough, R. W. (1960). The finite element method in plane stress analysis. In *Proceedings of 2nd ASCE Conference on Electronic Computation, Pittsburgh Pa., Sept. 8 and 9, 1960*.

Cluni, F., Costarelli, D., Gusella, V., and Vinti, G. (2020). Reliability increase of masonry characteristics estimation by a sampling algorithm applied to thermographic digital images. *Probabilistic Engineering Mechanics*, 60:103022.

Cluni, F. and Gusella, V. (2004). Homogenization of non-periodic masonry structures. *International Journal of Solids and Structures*, 41(7):1911–1923.

Cluni, F., Gusella, V., and Vinti, G. (2019). Masonry elastic characteristics assessment by thermographic images. *Meccanica*, 54(9):1339–1349.

Corradi, M., Tedeschi, C., Binda, L., and Borri, A. (2008). Experimental evaluation of shear and compression strength of masonry wall before and after reinforcement: Deep repointing. *Construction and Building Materials*, 22(4):463–472.

Courant, R. et al. (1943). Variational methods for the solution of problems of equilibrium and vibrations. *Lecture notes in pure and applied mathematics*, pages 1–1.

Courant, R. and Hilbert, D. (1953). *Methods of mathematical physics: partial differential equations*. John Wiley & Sons.

Dantzig, G. B. (2002). Linear programming. *Operations research*, 50(1):42–47.

de Buhan, P. and de Felice, G. (1997). A homogenization approach to the ultimate strength of brick masonry. *Journal of the Mechanics and Physics of Solids*, 45(7):1085–1104.

de Felice, G. and Giannini, R. (2001). Out-of-plane seismic resistance of masonry walls. *Journal of Earthquake Engineering*, 5(2):253–271.

Diamond, S. and Boyd, S. (2016). CVXPY: A Python-embedded modeling language for convex optimization. *J Mach Learn Res*, 17(83):1–5.

Domahidi, A., Chu, E., and Boyd, S. (2013). ECOS: An SOCP solver for embedded systems. In *2013 European Control Conference (ECC)*, pages 3071–3076. IEEE.

Dorn, W. (1964). Automatic design of optimal structures. *J. de Mecanique*, 3:25–52.

Falsone, G. and Lombardo, M. (2007). Stochastic representation of the mechanical properties of irregular masonry structures. *International Journal of Solids and Structures*, 44(25):8600–8612.

Ferris, M. and Tin-Loi, F. (2001). Limit analysis of frictional block assemblies as a mathematical program with complementarity constraints. *International Journal of Mechanical Sciences*, 43(1):209–224.

Gilbert, M., Casapulla, C., and Ahmed, H. (2006). Limit analysis of masonry block structures with non-associative frictional joints using linear programming. *Computers and Structures*, 84(13-14):873–887.

Gilbert, M., Smith, C., and Pritchard, T. (2010). Masonry arch analysis using discontinuity layout optimisation. *Proceedings of the Institution of Civil Engineers - Engineering and Computational Mechanics*, 163(3):155–166.

Gilbert, M. and Tyas, A. (2003). Layout optimization of large-scale pin-jointed frames. *Engineering Computations*, 20(8):1044–1064.

Hawksbee, S. J. (2012). *3D ultimate limit state analysis using discontinuity layout optimization*. PhD thesis, University of Sheffield.

He, L. and Gilbert, M. (2016). Automatic rationalization of yield-line patterns identified using discontinuity layout optimization. *International Journal of Solids and Structures*, 84:27–39.

He, L., Gilbert, M., and Song, X. (2019). A Python script for adaptive layout optimization of trusses. *Structural and Multidisciplinary Optimization*, 60(2):835–847.

Bibliography

Hegemier, G. and Prager, W. (1969). On michell trusses. *International Journal of Mechanical Sciences*, 11(2):209–215.

Hill, R. (1950). *The mathematical theory of plasticity*, volume 11. Oxford university press.

Huber, M. (1904). Czasopismo techniczne. *Lemberg, Austria*, 22:181.

Johnson, W. (1961). An analogy between upper-bound solutions for plane-strain metal working and minimum-weight two-dimensional frames. *International Journal of Mechanical Sciences*, 3(4):239–246.

Karmarkar, N. (1984). A new polynomial-time algorithm for linear programming. In *Proceedings of the sixteenth annual ACM symposium on Theory of computing*, pages 302–311.

Lewiński, T., Zhou, M., and Rozvany, G. (1994). Extended exact solutions for least-weight truss layouts—part I: cantilever with a horizontal axis of symmetry. *International Journal of Mechanical Sciences*, 36(5):375–398.

Livesley, R. K. (1978). Limit analysis of structures formed from rigid blocks. *International Journal for Numerical Methods in Engineering*, 12(12):1853–1871.

Llorens, J., Chamorro, M. A., Fontàs, J., Alcalà, M., Delgado-Aguilar, M., Julián, F., and Llorens, M. (2021). Experimental behavior of thin-tile masonry under uniaxial compression. multi-leaf case study. *Materials*, 14(11).

Maier, G. and Munro, J. (1982). Mathematical programming applications to engineering plastic analysis. *Applied Mechanics Reviews*, 35:1631–1643.

Matousek, J. and Gärtner, B. (2006). *Understanding and using linear programming*. Springer Science & Business Media.

Mikhlin, S. G. and Chambers, L. (1964). *Variational methods in mathematical physics*, volume 50. Pergamon Press Oxford.

MOSEK ApS (2019). *MOSEK Optimizer API for C 9.1.13*.

Murty, K. (1983). Linear programming.

Nering, E. D. and Tucker, A. W. (1992). *Linear Programs & Related Problems: A Volume in the Computer Science and Scientific Computing Series*. Elsevier.

Pande, G., Liang, J., and Middleton, J. (1989). Equivalent elastic moduli for brick masonry. *Computers and Geotechnics*, 8(3):243–265.

Przemieniecki, J. S. (1985). *Theory of matrix structural analysis*. Courier Corporation.

Bibliography

Rios, A. J., Pingaro, M., Reccia, E., and Trovalusci, P. (2022). Statistical assessment of in-plane masonry panels using limit analysis with sliding mechanism. *Journal of Engineering Mechanics*, 148(2):04021158.

Smith, C. and Gilbert, M. (2007). Application of discontinuity layout optimization to plane plasticity problems. *Proc. R. Soc. A*, 463:2461–2484. doi:10.1098/rspa.2006.1788.

Smith, C. and Gilbert, M. (2013). Identification of rotational failure mechanisms in cohesive media using discontinuity layout optimisation. *Geotechnique*, 63(14):1194–1208.

Smith, C. C. and Gilbert, M. (2022). The stress function basis of the upper bound theorem of plasticity. *International Journal of Solids and Structures*, 244:111565.

Smith, M. (2009). Abaqus/standard user's manual, version 6.9.

Strang, G. (1987). Karmarkar's algorithm and its place in applied mathematics. *The Mathematical Intelligencer*, 9(2):4–10.

Synge, J. L. and Rheinboldt, W. (1957). The hypercircle in mathematical physics. *Physics Today*, 10(10):45.

Tiberti, S. and Milani, G. (2019). 2D pixel homogenized limit analysis of non-periodic masonry walls. *Computers and Structures*, 219:16–57.

Tiberti, S. and Milani, G. (2020). 3d homogenized limit analysis of non-periodic multi-leaf masonry walls. *Computers and Structures*, 234:106253.

Timoshenko, S. P. and Goodier, J. N. (1934). *Theory fo Elasticity*. McGraw-Hill.

Turner, M. J., Clough, R. W., Martin, H. C., and Topp, L. (1956). Stiffness and deflection analysis of complex structures. *journal of the Aeronautical Sciences*, 23(9):805–823.

Valentino, J., Gilbert, M., Gueguin, M., and Smith, C. C. (2023). Limit analysis of masonry walls using discontinuity layout optimization and homogenization. *International Journal for Numerical Methods in Engineering*, 124(2):358–381.

Vanderbei, R. J. (2001). Linear programming: Foundations and extensions. 2001. *Google Scholar Google Scholar Cross Ref Cross Ref*.

Šejnoha, J., Šejnoha, M., Zeman, J., Sykora, J., and Vorel, J. (2008). Mesoscopic study on historic masonry. *Structural Engineering and Mechanics*, 30(1):99–117.